

1 2



9 0

UNIVERSIDADE D
COIMBRA

Ana Rita Rolo Ferreira

**Synthesis and Characterization of a
Biocompatible Fluorinated Mn(III)-
Porphyrin as a Redox Responsive ^{19}F -
NMR/ T_1 Bimodal MRI Contrast Agent**

Dissertation submitted to the Department of Life Sciences of the Faculty of Sciences and Technology of the University of Coimbra for the Master's Degree in Biochemistry, supervised by Prof. Dr. Carlos Geraldes, Prof. Dr. Maria Paula Marques, and Dr. Sara Pinto

October 2021

Ana Rita Rolo Ferreira

**Synthesis and Characterization of a
Biocompatible Fluorinated Mn(III)-Porphyrin as
a Redox Responsive ^{19}F -NMR/ T_1 Bimodal MRI
Contrast Agent**

Trabalho realizado no âmbito da disciplina Dissertação em Bioquímica, do Mestrado em Bioquímica, sob a orientação científica do Professor Doutor Carlos Geraldes e da Professora Doutora Maria Paula Marques, do Departamento de Ciências da Vida da Faculdade de Ciências e Tecnologia da Universidade de Coimbra, e da Doutora Sara Pinto, do Departamento de Química da Faculdade de Ciências e Tecnologia da Universidade de Coimbra.

Outubro de 2021

“Just because something does not do what you planned it to do does
not mean it is useless”

Thomas A. Edison

Agradecimentos

A elaboração de uma dissertação de mestrado é uma longa viagem, pautada por inúmeros desafios, adversidades, incertezas, alegrias e tristezas. No fim de mais um ciclo, que me permitiu não só adquirir novos conhecimentos, contribuindo para o meu enriquecimento académico, mas também crescer a nível pessoal, gostaria de expressar o meu mais sincero agradecimento a todas as pessoas que, de alguma forma, me ajudaram a chegar aqui hoje e fizeram parte deste percurso.

Em primeiro lugar, ao meu orientador, Professor Doutor Carlos Geraldês, agradeço o voto de confiança, toda a paciência, empenho, conhecimento científico e sentido prático com que sempre me orientou durante a realização desta dissertação.

À minha coorientadora, Doutora Sara Pinto, agradeço a orientação exemplar, pautada por um elevado e rigoroso conhecimento científico, e a sua visão crítica e oportuna, as quais foram fundamentais em todas as etapas deste trabalho, especialmente nas adversidades. Um obrigada por ter sempre acreditado em mim, por toda a motivação, palavras de conforto e ânimo. Quero agradecer, de igual modo, ao Laboratório de Catálise e Química Fina por me terem aceitado e acolhido de braços abertos.

À minha coorientadora, Professora Doutora Maria Paula Marques, agradeço a possibilidade de desenvolver parte do meu trabalho no seu grupo de investigação, pelo conhecimento científico e por toda a amabilidade. À Doutora Ana Lúcia Carvalho, agradeço todo o conhecimento partilhado e toda a paciência que teve comigo no laboratório, que foi crucial. Quero agradecer também à Unidade de Química-Física Molecular por me fazerem sentir parte do grupo e sempre tão bem-vinda.

Queria também expressar o meu mais sincero agradecimento ao Laboratório de Ressonância Magnética Nuclear, em especial ao Pedro Cruz, por toda a paciência que teve comigo e por todo o conhecimento científico.

Por fim, quero agradecer aos meus pais por terem sempre acreditado em mim e pelo apoio incondicional ao longo desta jornada. À minha irmã Inês, por toda a paciência e por me fazer todas as vontades. Aos meus colegas de laboratório, em especial à Ana, quero agradecer por toda a ajuda prestada e pelas palavras de conforto nos momentos mais difíceis. À Margarida, por estar sempre lá para mim, pelas palavras reconfortantes, pelas longas conversas e por toda a ajuda. À Ângela, pela divisão de tarefas, pelos lanches partilhados e pelas conversas ao sol. À Mariana, que mesmo à distância, sempre me deu força e coragem para continuar e nunca desistir. Por último, mas não menos importante, aos meus colegas de casa, em especial ao Armando e ao Diogo, pelas conversas, pelos jantares, pelas brincadeiras e pela boa disposição ao longo destes meses.

Index

Abbreviations and Symbols.....	v
Index of Figures	ix
Index of Tables	xiii
Abstract	xv
Resumo	xvii
Introduction.....	1
1.1. Molecular Imaging.....	3
1.1.1. Importance of Molecular Imaging.....	3
1.2. Magnetic Resonance Imaging.....	4
1.2.1. Origin	4
1.2.2. Principle	5
1.2.3. Advantages	6
1.2.4. Nuclear Relaxation Times.....	6
1.2.5. The ¹⁹ F MRI Technique	8
1.2.6. Signal to Noise Ratio.....	9
1.2.7. MRI and Cancer	10
1.3. Contrast Agents	10
1.3.1. Paramagnetic and Superparamagnetic Agents.....	12
1.3.2. Fluorinated Agents	13
1.3.3. Porphyrins as Contrast Agents	14
1.3.4. Redox Responsive Probes	17
1.4. Cyclodextrins	18
1.5. <i>In Vitro</i> Studies.....	20

1.5.1. The Epithelial Cell Model.....	21
1.5.2. The Caco-2 Cell Line.....	23
1.5.2.1. Origin	23
1.5.2.2. Features and Mechanisms	23
1.5.2.3. Stability, Consistency and Reproducibility	24
1.5.2.4. Relevance to Human <i>In Vivo</i> Conditions	25
1.5.2.5. Applications.....	25
1.5.2.6. Advantages and Disadvantages	26
1.6. Aim of the Work	26
Materials and Methods.....	27
2.1. Materials	29
2.2. Biological Material.....	31
2.3. Equipment.....	31
2.4. Composition of the Solutions Used	33
2.5. Synthesis of the Mn(III)TPP- <i>p</i> -CF ₃ Probe.....	34
2.5.1. Synthesis of Free-base 5,10,15,20-tetrakis(4-trifluoromethylphenyl) porphyrin (TPP- <i>p</i> -CF ₃).....	34
2.5.2. Complexation of TPP- <i>p</i> -CF ₃ with manganese.....	35
2.6. Characterization of the Mn(III)TPP- <i>p</i> -CF ₃ Probe	36
2.6.1. Determination of Molar Absorption Coefficients	36
2.6.2. Reduction of Mn(III)TPP- <i>p</i> -CF ₃	36
2.6.3. ^1H and ^{19}F NMR Study.....	36
2.6.4. Reduction Kinetics of Mn(III)TPP- <i>p</i> -CF ₃	37
2.6.5. ^{19}F NMR Relaxometry	37

2.7.	Inclusion of Mn(III)TPP- <i>p</i> -CF ₃ into γ -cyclodextrin	37
2.7.1.	Inclusion Study	37
2.7.2.	Reduction of γ -CD*Mn(III)TPP- <i>p</i> -CF ₃	38
2.7.3.	¹ H and ¹⁹ F NMR Study.....	38
2.7.4.	Stoichiometric Determination.....	39
2.8.	Cell Initiation	40
2.9.	Cell Culture Procedure.....	41
2.10.	Trypan Blue Exclusion Method.....	42
2.11.	Morphological Studies.....	43
2.12.	<i>In Vitro</i> Antitumour Assays	44
2.12.1.	SRB Assay	45
2.12.2.	MTT Assay	47
2.13.	Data Processing and Analysis.....	48
	Results and Discussion.....	51
3.1.	Synthesis of the Mn(III)TPP- <i>p</i> -CF ₃ Probe.....	53
3.2.	Characterization of the Mn(III)TPP- <i>p</i> -CF ₃ Probe	57
3.2.1.	Determination of Molar Absorption Coefficients	57
3.2.2.	Reduction of Mn(III)TPP- <i>p</i> -CF ₃	60
3.2.2.1.	Study Performed with Ascorbic Acid.....	60
3.2.2.2.	Study Performed with Glutathione	64
3.2.3.	¹ H and ¹⁹ F Study.....	65
3.2.4.	Reduction kinetics of Mn(III)TPP- <i>p</i> -CF ₃	67
3.2.5.	¹⁹ F NMR Relaxometry	68
3.3.	Inclusion of Mn(III)TPP- <i>p</i> -CF ₃ into γ -cyclodextrin	70

3.3.1. Inclusion Study.....	70
3.3.2. Reduction of γ -CD*Mn(III)TPP- <i>p</i> -CF ₃	71
3.3.3. ¹ H and ¹⁹ F NMR Study.....	72
3.3.4. Stoichiometric Determination.....	75
3.4. <i>In Vitro</i> Antitumour Assays	76
Conclusion and Future Perspectives.....	81
References	87

Abbreviations and Symbols

ATCC	American Type Culture Collection
B	Magnetic Field
BBB	Blood-Brain-Barrier
CA	Contrast Agents
Ca ²⁺	Calcium Ion
Caco-2	Cancer Coli-2
CDs	Cyclodextrins
CEST	Chemical Exchange Saturation Transfer
CPMG	Carr-Purcell-Meiboom-Gill
CSF	Cerebrospinal Fluid
CT	Computed Tomography
DHA	Dehydroascorbic Acid
DIACEST	Diamagnetic CEST
DMSO	Dimethyl Sulfoxide
DSC	Differential Scanning Calorimetry
Dy ³⁺	Dysprosium Ion
ECACC	European Collection of Authenticated Cell Cultures
EDTA	Ethylenediaminetetraacetic Acid
FAD	Flavin Adenine Dinucleotide
FADH	Dihydroflavine Adenine Dinucleotide
FBS	Fetal Bovine Serum
FDA	Food and Drug Administration
FID	Free Induction Decay
FT	Fourier Transform
GBCAs	Gadolinium-based Contrast Agents
Gd ³⁺	Gadolinium (III) Ion
Gd-DTPA.(H ₂ O)	Gadolinium(III)-Diethylenetriamine Pentaacetic Acid Monohydrate
GSH	Glutathione Reduced
GSSG	Glutathione Disulphide
HDO	Semiheavy Water
HEPES	4-(2-Hydroxyethyl)piperazine-1-ethanesulfonic Acid
HSA	Human Serum Albumin
IDH	Isocitrate Dehydrogenase

IECs	Intestinal Epithelial Cells
K _{eq}	Equilibrium Constant
I	Nuclear Spin
LD50	Median Lethal Dose
Ln ³⁺	Lanthanide Ion
MEM	Minimum Essential Medium
MEMRI	Manganese-Enhanced MRI
Mn ^{2+/3+}	Manganese Ion
MnCl ₂	Manganese Chloride
Mn-DPDP	Mangafodipir Trisodium
MnO	Manganese Oxide
Mn(II)TPP- <i>p</i> -CF ₃	5,10,15,20-tetrakis(4-trifluoromethylphenyl) Manganese(II) Porphyrin
Mn(III)-TPP-mPEG ₅₅₀	Mn(III)TPP-methoxy Poly(ethylene glycol) Porphyrin
Mn(III)TPP- <i>p</i> -CF ₃	5,10,15,20-tetrakis(4-trifluoromethylphenyl) Manganese(III) Porphyrin
[Mn(III)(TPPS ₄)] ³⁻	Mn-meso-tetra-(4-sulfonatophenyl) Porphyrin
MR	Magnetic Resonance
MRI	Magnetic Resonance Imaging
mRNAs	Messenger Ribonucleic Acid
MTT	3-(4,5-dimethylthiazol-2-yl)-2,5-diphenyltetrazolium Bromide
NADH	Nicotinamide Adenine Dinucleotide
NADPH	Nicotinamide Adenine Dinucleotide Phosphate
NCI	National Cancer Institute
NEAA	Non-Essential Amino Acids
NMR	Nuclear Magnetic Resonance
NSF	Nephrogenic Systemic Fibrosis
PARACEST	Paramagnetic CEST
PBS	Phosphate Buffered Saline
PEG	Polyethylene Glycol
Pen/Step	Penicillin/Streptomycin
PET	Positron Emission Tomography
PFCs	Perfluorocarbons
P450	Cytochrome P450
R	Relaxation Rate
Redox	Oxidation-Reduction Reactions

RF	Radiofrequency
RMN	Ressonância Magnética Nuclear
RNS	Reactive Nitrogen Species
ROS	Reactive Oxygen Species
rpm	Rotations per Minute
S	Electronic Spin
SD	Standard Deviation
SDH	Succinate Dehydrogenase
SNR	Signal to Noise Ratio
SPECT	Single-Photon Emission Computed Tomography
SPIO	Superparamagnetic Iron Oxide
SRB	Sulforhodamine B
T	Tesla
TB	Trypan Blue
TE	Echo Time
TEER	Transepithelial Electric Resistance
TGA	Thermal Gravimetric Analysis
THF	Tetrahydrofuran
TJ	Tight Junction
TMS	Tetramethylsilane
TPP	5,10,15,20-tetrakis(phenyl) Porphyrin
TPP- <i>p</i> -CF ₃	5,10,15,20-tetrakis(4-trifluoromethylphenyl) Porphyrin
TPPS ₄	Meso-tetra-(4-sulfonatophenyl) Porphyrin
TR	Repetition Time
Tris	Tris(hydroxymethyl)aminomethane
T ₁	Spin-Lattice Relaxation Time
T _{1w}	T ₁ -weighted Image
T ₂	Spin-spin Relaxation Time
T ₂ *	Effective spin-spin Relaxation Time
US	Ultrasound
UV-Vis	Ultraviolet-Visible
UV-Vis-NIR	Ultraviolet-Visible-Near Infrared
Yb ³⁺	Ytterbium (III) Ion
¹ H	Hydrogen
¹³ C	Carbon Isotope
¹⁵ N	Nitrogen

¹⁸ F-MISO	¹⁸ F-fluoro-misonidazole
¹⁹ F	Fluorine
²³ Na	Sodium
⁶⁴ CuII-ATSM	⁶⁴ CuII-diacetyl-bis(N4-methylthiosemicarbazone)
2D	Two-dimensional
3D	Three-dimensional
α-CD	Alpha Cyclodextrin
β-CD	Beta Cyclodextrin
γ-CD	Gamma Cyclodextrin
γ-CD*Mn(III)TPP- <i>p</i> -CF ₃	Inclusion Complex of Mn(III)TPP- <i>p</i> -CF ₃ into γ-CD
μ	Nuclear Magnetic Moment

Index of Figures

Figure 1.1. The free induction decay and Fourier Transformation can generate MR images or MR spectra.....	6
Figure 1.2. Choice of multi-parameter soft tissue contrasts available with MRI. The soft tissue contrast can vary depending on the appropriate choice of imaging sequences and corresponding sequence parameters, as illustrated from the axial cross-section healthy brain. A: A T ₁ -weighted image; B: T ₂ -weighted image; C: fast gray matter acquisition T ₁ inversion-recovery image.....	8
Figure 1.3. Schematic representation of the molecular structure of the currently commercially available Gd ³⁺ -containing MRI CAs. Charges in structures are omitted for clarity. The brand names are given between brackets. Relaxivities are in s ⁻¹ mM ⁻¹ measured in aqueous solution at 1.5 T and 37 °C.....	11
Figure 1.4. T ₁ -weighted MR images tumour-bearing mice before and after intravenous administration of (I) an Mn-porphyrin complex conjugated with dextran, and Gd-DTPA (II): (a) before the injection; (b) post-injection (30 minutes). The arrows illustrate the enhanced boundary of the tumours.....	16
Figure 1.5. Molecular structures (top) and dimensions (bottom) of α-CDs, β-CDs and γ-CDs (from left to right).....	19
Figure 1.6. Schematic representation of polarized epithelial cells with different types of intercellular contacts. These are essential for the maintenance of barrier function and communication between neighbouring cells.....	21
Figure 1.7. Different mechanisms of absorption and transport through the intestinal epithelium: (1) paracellular transport; (2) passive diffusion of molecules from the apical to the basolateral side; (3) vesicle-mediated transcytosis; (4) carrier-mediated uptake and diffusion through the epithelial cell layer.....	22
Figure 1.8. Caco-2 cells observed under an inverted optical microscope. On the left, the cells are seeded at low density. On the right, the cells exhibit high density. The emergence of the monolayer is notorious [images supplied by ATCC® (American Type Culture Collection)].....	24
Figure 2.1. Chemical structure of TPP- <i>p</i> -CF ₃	35
Figure 2.2. Chemical structure of Mn(III)TPP- <i>p</i> -CF ₃	35
Figure 2.3. Schematic representation of the main steps required for cell initiation.....	41
Figure 2.4. Growth curve of Caco-2 cells. The cell viability was determined by the SRB method. The number of cells gradually increases with time before reaching the stationary growth phase.....	41

Figure 2.5. Schematic representation of the fundamental steps required for cell subculturing.....	42
Figure 2.6. Schematic representation of a hemocytometer (A) and its counting areas (B). Before cell counting, a coverslip was placed over the hemocytometer and the cellular suspension with TB was added to both counting areas. Only the cells represented in the numbered squares were counted, according to the rule depicted in square number 4: the green and empty circles indicate the counted cells (inside the grid and overlapping with the top and left edges), while the red circles indicate the cells excluded from the counting.....	43
Figure 2.7. Caco-2 cell line at passage #57 observed under an inverted optical microscope. The left panel shows cells seeded at low density. The right panel shows cells exhibiting a high density, where the formation of the monolayer is prominent.....	44
Figure 2.8. Chemical structure of Sulforhodamine B.....	45
Figure 2.9. Protocol used for analysis of cell protein content based on the SRB assay.....	46
Figure 2.10. Reduction of MTT bromide to its formazan crystals by cellular reductases, in viable cells.....	47
Figure 2.11. Protocol used for the analysis of cell viability based on the MTT metabolization.....	48
Figure 3.1. Synthesis of TPP- <i>p</i> -CF ₃ . Reagents and reaction conditions: Acetic acid/Nitrobenzene, 2 hours, 120°C.....	53
Figure 3.2. Synthesis of Mn(III)TPP- <i>p</i> -CF ₃ . Reagents and reaction conditions: Acetic acid/Sodium acetate, 2 hours, 80°C.....	54
Figure 3.3. ¹ H NMR spectrum of 0.6 mM TPP- <i>p</i> -CF ₃ recorded in DMSO-d ₆ , at room temperature (25°C).....	54
Figure 3.4. ¹ H NMR spectrum of 0.6 mM Mn(III)TPP- <i>p</i> -CF ₃ in DMSO-d ₆ , at room temperature (25°C).....	55
Figure 3.5. ¹⁹ F NMR spectrum of 0.6 mM Mn(III)TPP- <i>p</i> -CF ₃ . The spectrum was recorded in deuterated DMSO, at room temperature (25°C).....	56
Figure 3.6. Optical absorption spectra of free-base porphyrin and metalloporphyrin in solution, at room temperature. In the metalloporphyrin, Q ₀ is the result of a pure electronic transition (no molecular vibrations) between the electronic ground state and the first electronic excited state; Q ₁ is due to the same electronic transition but also molecular vibrations are involved. This band is called a vibronic band. The 0 and 1 of free-base porphyrin indicate a similar interpretation. The x and y refer to the orientation (polarization) of the electric vector of the absorbed light concerning the axes shown on the chemical structure diagram for free-base porphyrin.....	57

Figure 3.7. Linear fit of molar absorbance coefficient vs. concentration for the Soret band of Mn(III)TPP- <i>p</i> -CF ₃ , in THF.....	59
Figure 3.8. Linear regression model of molar absorbance coefficient for the Q bands of Mn(III)TPP- <i>p</i> -CF ₃ , in THF. The Q ₂ band (with a wavelength of 618 nm) and the Q ₁ band (with a wavelength of 582 nm on the right) are represented on the left, and on the right, respectively.....	59
Figure 3.9. UV-Vis reduction titration of 0.0125 mM Mn(III)TPP- <i>p</i> -CF ₃ with ascorbic acid, recorded in THF (25°C). Number of equivalents of ascorbic acid added: 0 (black line); 0.87 (red line); 2.18 (blue line); 3.93 (green line); 12.65 (purple line).....	60
Figure 3.10. UV-Vis spectrum of the reoxidation of Mn(II)TPP- <i>p</i> -CF ₃ (green line) in THF, obtained upon air exposure after 1 hour. Complete conversion to Mn ^{III} was attained (blue line). The initial Mn(III)TPP- <i>p</i> -CF ₃ spectrum is represented by the black line.....	61
Figure 3.11. UV-Vis reduction spectra of 0.0125 mM Mn(III)TPP- <i>p</i> -CF ₃ with 0.87 equivalents of ascorbic acid, recorded in THF (25°C). The spectra were acquired in different time points: 0 min (black line); 1 min (red line); 5 min (blue line); 10 min (green line); 20 (purple line); 30 min (orange line).....	62
Figure 3.12. UV-Vis reduction titration of 0.0125 mM Mn(III)TPP- <i>p</i> -CF ₃ with ascorbic acid, recorded in DMSO (25°C) (left), and reoxidation of Mn(II)TPP- <i>p</i> -CF ₃ obtained upon air exposure after 1 hour (right). Left: number of equivalents of ascorbic acid added: 0 (black line); 2.50 (red line); 8.35 (blue line); 12.52 (green line); 16.70 (purple line). Right: initial Mn(III)TPP- <i>p</i> -CF ₃ (black line); Mn(II)TPP- <i>p</i> -CF ₃ (red line); complete reoxidation to Mn ^{III} (blue line).....	63
Figure 3.13. UV-Vis spectra of Mn(III)TPP- <i>p</i> -CF ₃ solutions upon addition of glutathione, recorded in THF (left) and DMSO (right) (25°C). The number of equivalents of glutathione added: 0 (black line); 2.50 (red line); 8.35 (blue line); 12.52 (green line); 16.70 (purple line).....	64
Figure 3.14. ¹ H NMR spectra of 0.6 mM Mn(III)TPP- <i>p</i> -CF ₃ before (left) and after (right) addition 16.70 equivalents of aqueous ascorbic acid, recorded in deuterated DMSO (25°C). (Number of scans = 143; acquisition time = 0.82 s).....	65
Figure 3.15. ¹⁹ F NMR spectral titration of 0.6 mM Mn(III)TPP- <i>p</i> -CF ₃ with ascorbic acid, recorded in deuterated DMSO (25°C). Number of equivalents of ascorbic acid added: 0 (red line); 8.32 (green line); 12.52 (blue line); 16.70 (purple line). (Number of scans = 123; acquisition time = 0.5 s).....	66
Figure 3.16. Reduction kinetics of 0.6 mM Mn(III)TPP- <i>p</i> -CF ₃ in DMSO- <i>d</i> ₆ upon addition of 2.5 equivalents of ascorbic acid in D ₂ O (25°C).....	67

- Figure 3.17.** UV-Vis spectra obtained for the solutions containing 0.0052 mM Mn(III)TPP-*p*-CF₃ and CDs (methyl-β-CD, on the left, and γ-CD, on the right). Concentrations of cyclodextrin in the prepared solutions: 0.1 mM (black line); 0.2 mM (red line); 0.4 mM (blue line); 0.5 mM (green line).....70
- Figure 3.18.** UV-Vis reduction titration spectra of the solutions containing 0.0052 mM Mn(III)TPP-*p*-CF₃ and different concentrations of γ-CD. Number of equivalents of ascorbic acid added: 0 (black line); 2.35 (red line); 7.57 (green line); 23.49 (blue line).....72
- Figure 3.19.** ¹H NMR spectra titration of 0.5 mM Mn(III)TPP-*p*-CF₃ in DMSO-d₆ (25°C) upon addition of aqueous γ-CD. Number of equivalents of γ-CD added: 0 (red line); 0.50 (light green line); 1 (dark green line); 2 (blue line); 3 (purple line). The spectrum of aqueous γ-CD is also shown. (Number of scans = 143; acquisition time = 0.82 s).....73
- Figure 3.20.** ¹⁹F NMR spectra titration of γ-CD with 0.5 mM Mn(III)TPP-*p*-CF₃, recorded in DMSO-d₆ (25°C). Number of equivalents of γ-CD added: 0 (red line); 0.50 (light green line); 1 (dark green line); 2 (blue line); 3 (purple line). (Number of scans = 128; acquisition time = 0.5 s).....74
- Figure 3.21.** Plot of absorbance (at 465 nm) of 0.052 mM Mn(III)TPP-*p*-CF₃ (in THF) vs. molar fractions of γ-CD used to prepare the solutions.....75
- Figure 3.22.** Effect of Mn(III)TPP-*p*-CF₃ and γ-CD*Mn(III)TPP-*p*-CF₃ on Caco-2 cells, assessed by the MTT (a) and b)) and SRB (c) and d)) colorimetric tests. After 72 hours of the addition of the tested agents, the medium was discarded and new culture medium was added. Control corresponds to 144 hours. Results are represented as mean ± SD of three independent experiments (n = 3), performed in triplicate for each experimental condition. SD of three independent experiments (n = 3), performed in triplicate for each experimental condition. The MTT data were expressed in % of each control at the different time points. The SRB data were expressed in % of C₀, according to equation 2.4. Data were analysed with the software GraphPad Prism 8.0.2, using the one-way ANOVA method followed by the Tukey's multiple comparison test: p* < 0.05; p** < 0.01; p*** < 0.001; p# < 0.0001 were considered statistically significant. If p > 0.05 no statistically significant differences were considered..... 77

Synthesis and Characterization of a Biocompatible Fluorinated Mn(III)-Porphyrin as a Redox Responsive ^{19}F -NMR/ T_1 Bimodal MRI Contrast Agent

Index of Tables

Table 1.1. Overview of several exogenous contrast agents for MRI and their properties...	12
Table 1.2. Chemical structures of reduced and oxidized forms of glutathione and ascorbic acid.....	18
Table 2.1. List of materials used in the experimental work.....	29
Table 2.2. List of equipment used in the experimental work.....	32
Table 2.3. List of solutions used for the <i>in vitro</i> assays.....	33
Table 2.4. Schematic representation of Job's Method experiment.....	40
Table 3.1. Values of the molar absorption coefficients obtained for the different bands of Mn(III)TPP- <i>p</i> -CF ₃	58
Table 3.2. Values of ¹⁹ F T ₁ and T ₂ relaxation times (ms), and respective R ₁ and R ₂ relaxation rates (s ⁻¹), for TPP- <i>p</i> -CF ₃ and Mn(III)TPP- <i>p</i> -CF ₃ solutions (0.6 mM) in DMSO-d ₆ (25°C).....	68

Synthesis and Characterization of a Biocompatible Fluorinated Mn(III)-Porphyrin as a Redox Responsive ¹⁹F-NMR/T₁ Bimodal MRI Contrast Agent

Abstract

Among the different imaging techniques, magnetic resonance imaging of chemical and physiological processes is becoming widespread. MRI is a powerful tool given its ability to image deep inside tissue with high temporal resolution and sensitivity. The strength of ^{19}F MRI comes from the negligible background signal in *in vivo* ^{19}F MRI and the broad chemical shift window of ^{19}F , making it possible to image more than one marker. Much of the growth of ^{19}F MRI can be assigned to novel designs of ^{19}F probes, which have improved imaging parameters due to the incorporation of paramagnetic ions. According to Bloch-Wangsness-Redfield theory, several parameters may affect the sensitivity of the fluorine-based probes, such as internuclear distance, rotational correlation times, geometry, as well as oxidation state and spin state of the metal ion.

In this dissertation, a novel porphyrin – Mn(III)TPP-*p*-CF₃ has been designed and synthesized to work as a “turn-off” redox probe for application in ^{19}F MRI. The incorporation with manganese, which is a paramagnetic metal ion, has the purpose to reduce T_1 relaxation time, allowing the acquisition of sufficient signal intensity in a reasonable period of time. The former probe was characterized by both UV-Vis absorption and $^1\text{H}/^{19}\text{F}$ NMR studies. For the development of redox responsive MRI probes based on the Mn^{III}/Mn^{II} couple, it is mandatory a stable complexation of both reduced and oxidized forms of the metal and appropriate tuning of the redox potential in a biologically relevant range. The non-water-soluble fluorinated Mn-porphyrin derivative satisfies both requirements. In aqueous solution, it can reversibly switch between Mn^{III}/Mn^{II} oxidation states. In the presence of ascorbic acid (one of the most important antioxidants), the Mn^{III} undergoes a slow reduction, reversed in the presence of air oxygen. However, the complex is not reduced by glutathione. This event is prevented by the coordination of the glutathione carboxylate groups to the Mn^{III} in the axial position. The inclusion of Mn(III)TPP-*p*-CF₃ into γ -CD aims to increase the probe hydrosolubility, considering their ability to form noncovalent inclusion complexes with hydrophobic guest molecules. ^{19}F NMR confirmed the inclusion of the meso aryl groups (CF₃) of the porphyrin into the γ -CD hydrophobic cavity. Although the γ -CD*Mn(III)TPP-*p*-CF₃ complex is also reduced by ascorbic acid, the inclusion with CD stabilizes both Mn^{III} and Mn^{II} oxidation states even in the absence of ascorbic acid, which may compromise its application as a redox responsive probe. The stoichiometry between the two compounds was not possible to determine experimentally, but it is expected to have a 2:1 stoichiometry (γ -CD:Mn(III)TPP-*p*-CF₃). Overall, no *in vitro* cytotoxicity in the human Caco-2 cell line was detectable for both complexes, even though the concentrations used were not in the typical MRI imaging concentration range.

Keywords: Magnetic resonance imaging; ¹⁹F MRI; redox responsive probes; porphyrin; manganese; cyclodextrins; Caco-2 cell line.

Resumo

De entre as diferentes técnicas de imagem, a ressonância magnética nuclear de processos químicos e fisiológicos tem vindo a ganhar maior destaque. A MRI é uma técnica bastante vantajosa, dada a sua capacidade de gerar imagens de tecidos profundos com alta resolução temporal e sensibilidade. A vantagem de ^{19}F MRI advém da ausência de sinal de flúor *in vivo* e da extensa janela química de ^{19}F , o que permite detetar simultaneamente mais do que uma sonda. O desenvolvimento da técnica de ^{19}F MRI deve-se ao design de novas sondas perfluoradas, com parâmetros de imagem melhorados devido à incorporação de iões paramagnéticos. De acordo com a teoria de Bloch-Wangsness-Redfield, vários fatores podem afetar a sensibilidade das sondas perfluoradas, como a distância internuclear, tempos de correlação rotacional, geometria, bem como o estado de oxidação e estado de spin do ião metálico.

Nesta dissertação foi sintetizada uma nova porfirina – Mn(III)TPP-*p*-CF₃ para aplicação em ^{19}F MRI como sonda “turn-off” redox. A incorporação com manganês, que é um ião paramagnético, tem como objetivo reduzir o tempo de relaxação T_1 , permitindo a aquisição de sinal com intensidade suficiente num período de tempo razoável. A sonda foi caracterizada por estudos de absorção UV-Vis e $^1\text{H}/^{19}\text{F}$ RMN. Para o desenvolvimento de sondas MRI sensíveis ao ambiente redox baseadas em Mn^{III}/Mn^{II}, a complexação estável das formas reduzida e oxidada do metal, bem como o ajuste apropriado do potencial redox numa faixa biologicamente relevante são fatores essenciais. A porfirina sintetizada, que é insolúvel em água, satisfaz ambos os requisitos. Em solução aquosa, consegue alternar reversivelmente entre os estados de oxidação Mn^{III}/Mn^{II}. Na presença de ácido ascórbico (um dos principais antioxidantes), o Mn^{III} sofre uma redução lenta, que é revertida com a exposição ao oxigénio do ar. No entanto, o complexo não é reduzido pela glutatona. Este facto deve-se à coordenação dos grupos carboxilo da glutatona ao Mn^{III}, em posição axial. A inclusão com γ -CD visa aumentar a hidrossolubilidade do complexo, considerando a sua capacidade de formar complexos de inclusão não covalentes com moléculas hóspedes hidrofóbicas. Através de ^{19}F RMN foi confirmada a inclusão dos grupos CF₃ da porfirina na cavidade hidrofóbica da γ -CD. Embora o complexo γ -CD*Mn(III)TPP-*p*-CF₃ também seja reduzido na presença de ácido ascórbico, a inclusão com γ -CD estabiliza ambos os estados de oxidação Mn^{III}/Mn^{II}, mesmo na ausência de ácido ascórbico, o que pode comprometer a sua aplicabilidade como sonda redox. Apesar de a estequiometria entre os dois compostos não ter sido determinada experimentalmente, é esperada uma estequiometria de 2:1 (γ -CD:Mn(III)TPP-*p*-CF₃). De uma forma geral, não foi detetada citotoxicidade *in vitro* na linha celular humana Caco-2 para ambos os complexos, embora as concentrações utilizadas não cobrissem a faixa de concentrações típica para aplicação em MRI.

Palavras-chave: Imagiologia por ressonância magnética; ¹⁹F MRI; sondas redox; porfirina; manganês; ciclodextrinas; linha celular Caco-2.

Introduction

Synthesis and Characterization of a Biocompatible Fluorinated Mn(III)-Porphyrin as a Redox Responsive ¹⁹F-NMR/T₁ Bimodal MRI Contrast Agent

1.1. Molecular Imaging

Through the years, a lot of research has been developed in multiple fields, leading to discoveries and progress. As biology and medicine come together, it is important that imaging also merges with biology to create the technology referred to as biological or molecular imaging. This merging is occurring at all levels, from imaging of molecules themselves to imaging of bacteria, viruses, cells, and organ systems. The organisms range from simple systems to humans, but in each case, imaging is becoming an essential technology of integrative biology [1].

The purpose of integrative biology is to ascertain the mechanisms of organized system function. The system can vary from proteins, with many effector sites through which its functions can be modified by interactions with other molecules, to an organ, such as the liver or the brain, in which a collection of cells functions as an integrated system based on the molecular mechanisms of signal transduction [2]. Thus, the role of molecular imaging is to provide technologies that can help in revealing whole systems and use molecular probes or interactions to examine the molecular mechanisms of integrated systems. Many imaging technologies have been and are being developed to achieve these goals, each one being unique for its applications, advantages, and limitations [3].

Molecular imaging has emerged at the end of the last century combining *in vivo* imaging and molecular biology with the aim of identifying and describing the living biological process at a cellular and molecular level using non-invasive procedures [4]. Therefore, it has a relevant role in determining diseases changes and promoting drug research and development, creating new medical modalities to monitor human health [5].

Distinct imaging technologies have been extensively used to monitor structural, functional, and molecular changes in cancer tissues, for instance, optical imaging, X-ray, computed tomography (CT), magnetic resonance imaging (MRI), positron emission tomography (PET), single-photon emission computed tomography (SPECT) and ultrasound (US) [6].

1.1.1. Importance of Molecular Imaging

Molecular imaging is catching the eyes of clinicians and scientists alike as the perks of the revolution in molecular medicine are applied to *in vivo* imaging of molecular function. Recently, it was possible to approach the capability to measure in the living animal and by non-invasive techniques, the spatial distribution of enzymes and other proteins, of target mRNAs and expressed genes, that until recently were detectable using only *ex vivo* techniques.

Multimodal molecular imaging combines two or more types of detection technologies to produce a new way of imaging, which is useful for acquiring some further information in diagnosis, treatment and monitoring [5]. In the last years, we were able to notice the quick development of molecular imaging, which greatly depends on the advances of biomedical probes, imaging systems and corresponding algorithms [4]. Optical molecular imaging is one of the most important parts of molecular imaging.

Along with the evolution of technology, imaging systems are expected to make good advances on spatial resolution, temporal resolution, tissue penetration, sensitivity, throughput and cost. The idea of employing multiple imaging modalities in a single imaging session comes from the fact that techniques with high sensitivity have relatively poor resolution, whilst those with high resolution have relatively poor sensitivity. Thus, the combination of complementary techniques can compensate for their disadvantages and potentiate their advantages.

Overall, it has been broadly used to optimize medical research and clinical practice nowadays [6]. In practice, multimodal molecular imaging can help to detect cardiovascular diseases [7], neuropsychiatric diseases [8], and other pathologies, such as degenerative diseases and cancer [9,10]. Additionally, it can considerably enhance the positioning of the tumour border and effectively guide the surgical resection of tumours. In effect, multimodal molecular imaging has a promising future. The development of this field will bring a breakthrough in medical imaging and research, and molecular biology. Even though molecular imaging remains at its initial stage, there is a broader space for further developments and improvements.

1.2. Magnetic Resonance Imaging

1.2.1. Origin

The nuclear magnetic resonance (NMR) phenomenon was first described experimentally in 1946, by Bloch and Purcell [11,12], who later shared the 1952 Nobel Prize in Physics. Several years later, the key discovery that nuclei in chemically distinct sites in the same molecule resonate at slightly different frequencies was reported [13,14], which contributed to the application of NMR in analytical spectroscopy. In 1971, Damadian recognized the diagnostic potential of NMR to distinguish between different tissues [15] and in 1973, Lauterbur published the first magnetic resonance (MR) image [16], receiving the 2003 Nobel Prize in Medicine or Physiology, together with Peter Mansfield. They observed that the resonance frequency is proportional to the strength of the applied magnetic field. So, by applying a magnetic field gradient, that would give rise to a range of

resonance frequencies, which shows the spatial distribution of protons, such as those found in water. In January 1974, a cross-sectional image of a living mouse was published by Lauterbur [17], and later, an aqueous solution of a paramagnetic manganese (Mn²⁺) salt was used as the first *in vivo* MR contrast agent, using a dog [18]. After the development of imaging-reconstruction techniques [19] and the emergence of fast and powerful computers, human magnetic resonance imaging was created in 1977-1978.

Since then, the technique has rapidly emerged, with the construction of the first high field [1.5 Tesla (T)] whole-body MRI scanner [20]. This improvement allowed its clinical application. The first clinical magnetic resonance images were obtained in Nottingham and Aberdeen in 1980, making MRI a powerful clinical tool, with over 25,000 of these systems in use today [21,22].

1.2.2. Principle

The MRI principle is based on the manipulation of the magnetic properties of the atomic nuclei present in the body with a non-zero nuclear spin (S), especially those found in the atoms of hydrogen. The motion of these nuclei produces a small magnetic moment. When a body is placed in the magnetic field of the MRI scanner, a small excess of the magnetic moments of these nuclei aligns with the direction of the magnetic field, creating a macroscopic magnetization along its z-axis. Then, a radiofrequency (RF) pulse is applied in a transmitter coil to the body in the scanner, exciting the nuclei such that there are transitions between lower and higher energy spin states, leading to a rotation of the magnetization away from the z-axis, with a rotating component along the x-y plane. This rotating magnetization creates an induced electric current in those coils (the free induction decay signal or FID) now connected to a receiver, which decays exponentially with time and with an oscillating component with a frequency equal to the frequency difference between the transmitter and receiver frequency. This signal can be digitalized and transformed into an NMR spectrum by a Fourier Transform (FT) in a computer. The intensity of the NMR signals of the water protons in the body can be transformed into a 2D MRI image, using three varying magnetic field gradients along the xyz axis, which localize spatially those signals (Figure 1.1) [23]. By using MRI probes, the contrast of these images is improved as well as the visibility of tissues and body structures. Scientific investigation in this field made it possible to use contrast agents (CA) to label specific cell types, and then monitor cells at the molecular level [24].

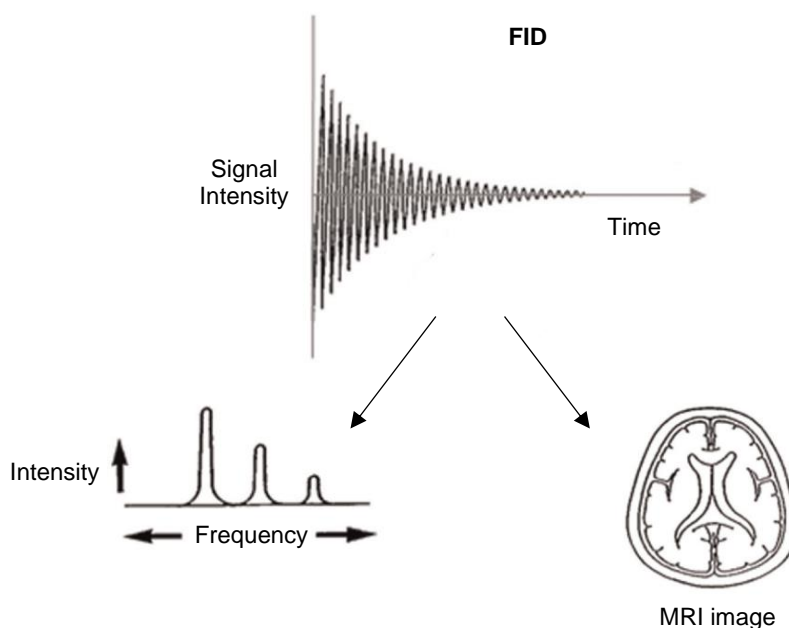


Figure 1.1. The free induction decay and Fourier Transformation can generate MR images or MR spectra. (Adapted from [25]).

1.2.3. Advantages

From initially being a technique recognised for its great potential, MRI has now become one of the most apprized primary diagnostic imaging modalities and has maintained this role up to this point [23,26]. This fulfilment is owed to the multiple characteristics and advantages of anatomical MRI, which enable great soft tissue contrast that hinges on multiple contrast parameters, the capacity to produce two-dimensional (2D) and three-dimensional (3D) data, besides the absence of ionizing radiation [27]. It also allows visualisation of deep tissues, provides anatomical and physiological information with precise spatial resolution, offers an excellent soft-tissue contrast, which can be optimized with the administration of contrast agents and is not dependent on an operator [24]. MRI is thus a non-invasive imaging technique that enables the visualisation of the internal structures of the body in health and disease. In fact, it has been used as a diagnostic tool, with a wide range of medical applications for over 30 years.

1.2.4. Nuclear Relaxation Times

Relaxation is the term applied to describe the process by which protons release the energy that they absorbed from the RF pulse. Relaxation is a central process in MR, as provides the prime mechanism of image contrast. In resonance absorption, RF energy is absorbed by the protons only when it is broadcast at the correct frequency. The extra energy distorts the equilibrium arrangements of the spins parallel and antiparallel to the

magnetic field (B). Following excitation, relaxation occurs when the protons release this added energy and return to their original configuration through naturally occurring processes. Although an individual proton absorbs the energy, relaxation times are measured for a complete sample and are statistical or average measurements. Relaxation times are measured for gray matter or cerebrospinal fluid as bulk samples, rather than for the individual water or fat molecules within the organs. Two types of relaxation can be measured - longitudinal and transverse relaxations, which are represented by the time constants T_1 and T_2 , respectively. Both times measure the spontaneous energy transfer by an excited proton, but they differ in the final disposition of the energy [23].

T_1 is also known as “spin-lattice relaxation”, by which the “lattice” is the surrounding nucleus environment. As longitudinal relaxation occurs, energy is dissipated into the lattice. So, T_1 refers to the time required for the z component of magnetization to return 63% toward the equilibrium following an RF pulse as an exponential function of time. The spin-lattice relaxation can be manipulated by varying the times between RF pulses and the repetition time (TR). While water and cerebrospinal fluid (CSF) have long T_1 values (3000-5000 ms), and thus they appear dark on T_1 -weighted images (T_{1w}), fat has a short T_1 value (260 ms) and appears bright on T_1 -weighted images. In tissues, the nature of the protein molecular structures and any metal ions that may be present have a pronounced effect on the frequency. Metal ions, such as iron or manganese, can have significant magnetic moments that may influence the local environment [26].

The relaxation time T_2 and T_2^* (T_2 with an added effect from the non-homogeneous magnetic field B_0) is the time required for the transverse component of magnetization to decay to 37% of its initial value via irreversible processes. It is also known as spin-spin relaxation time or transverse relaxation time. Relaxation processes may also redistribute energy among the nuclei within a spin system, without the whole spin system losing energy. As a result, when an RF pulse is applied, nuclei align predominantly along the axis of the applied energy. On relaxation, there is dephasing of nuclei orientations as energy is transferred between the nuclei, and there is a reduction in the resultant field direction, with a more random arrangement of alignments. In this manner, T_2 measures how fast the spins exchange energy in the “xy” plane. Tissues with longer T_2 appear hyperintense on T_2 -weighted images [26].

The two most important MR parameters, which influence all MR sequences, are TR and TE (echo time). TR refers to the time between subsequent RF pulses, while TE indicates the time between RF excitations and signal acquisition. By combining both TE and TR, the relative contrast weighting of various tissues can be determined. Short TR and short TE will generate T_1 -weighted images, whereas long TR and long TE will generate T_2 -

weighted images. Moreover, acquisitions with long TR and short TE generate proton-density-weighted images, while the signal of the image is ascertained by the voxel hydrogen content. MRI images can thus be weighted in T_1 or T_2 , depending on the structures that are intended to visualize. T_{1w} images are produced primarily to observe soft tissue and fat, while T_2 -weighted images are intended to visualise body fluids as well as multiple pathologies (Figure 1.2) [27].

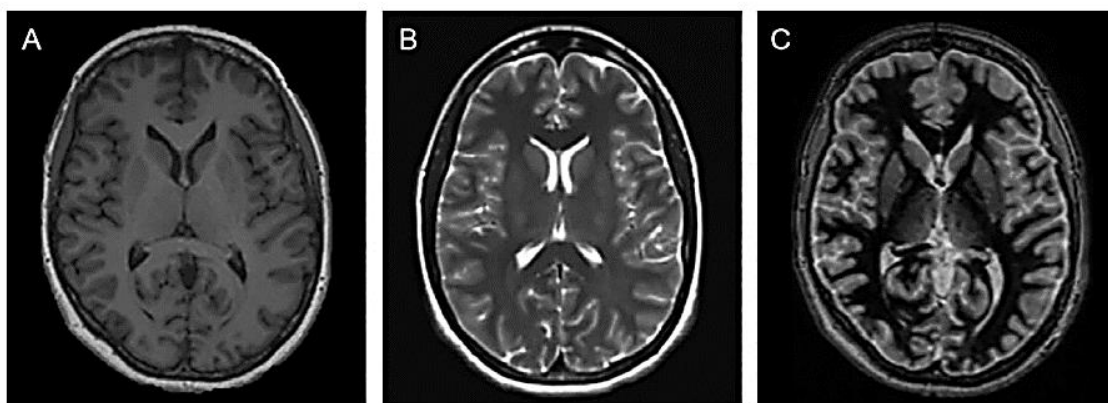


Figure 1.2. Choice of multi-parameter soft tissue contrasts available with MRI. The soft tissue contrast can vary depending on the appropriate choice of imaging sequences and corresponding sequence parameters, as illustrated from the axial cross-section healthy brain. A: A T_1 -weighted image; B: T_2 -weighted image; C: fast gray matter acquisition T_1 inversion-recovery image. (From [27]).

1.2.5. The ^{19}F MRI Technique

Considering the multiple advantages of MRI, which essentially focus on the magnetic properties of the water protons present in the tissues, the possibility of using other nuclei for application in MRI was studied and analysed. Besides protons, other body abundant nuclei with a nuclear spin (I) $I > 0$, such as ^{23}Na ($I = 3/2$), or slow relaxing non-abundant nuclei with $I = 1/2$ present in labelled biomolecules (such as ^{13}C and ^{15}N) can generate a strong *in vivo* magnetic resonance signal using hyperpolarization techniques. One of the useful nuclei is fluorine (^{19}F), which like hydrogen (^1H), also has nuclear spin $I = 1/2$. After the feasibility of fluorine imaging has been proven, several ^{19}F -containing materials were investigated as tracers [28].

^{19}F MRI has emerged as a novel technology for, not only tracking transplanted immune cells but also endogenous macrophage-type cells that are present in some inflammatory disorders (such as autoimmune myocarditis and inflammatory bowel disease). Indeed, ^{19}F MRI can provide more accurate and unambiguous detection of labelled cells, considering that there is a lack of background signal from the body [29]. In addition, the relationship between the concentration of the ^{19}F and signal intensity is directly

proportional and linear over a wide range of concentrations, which allows direct quantification of the signal from the acquired images. The absence of a detectable background in the ¹⁹F signal in biological tissues contributes to higher visibility of the target cells, similar to “hot spots” emerging from an empty background. The main limitation is that ¹⁹F MRI requires the use of separate coils for image acquisition, or the use of a multinuclear detector coil, neither of which is typically available in many MRI places. Conversely, the resonance frequency of ¹⁹F is near to that of ¹H, existing ¹H coils adapted for use as dual-tuned coils, ensuring the acquisition of both ¹H and ¹⁹F nuclei [30].

1.2.6. Signal to Noise Ratio

Signal to noise ratio (SNR) can be defined by the signal/noise ratio, which is measured frequently by calculating the difference in signal intensity between the area of interest and the background. The SNR is proportional to the volume of the voxel and to the square root of the number of averages and phase steps, assuming that the voxels size are constant [31]. Considering averaging and increasing the phase steps take time, SNR is approximately the same as the acquisition time. In MRI, the SNR can be improved by adjusting several parameters, for instance, volume acquisition as compared to 2D imaging, spin-echo sequences as compared to gradient echo, and increasing the signal by decreasing the TE and increasing the TR [32].

When using fluorinated probes, SNR is the first challenge to overcome, since fluorine signal is often just above the detection limit due to its low concentration in tissues. Also, the scanning times are limited. Particularly for quantification, a sufficient range above the detection limit is essential to measure the fully dynamic range of signal intensities [33]. The signal obtained from a fluorinated molecule depends on its resonance (with specific excitation frequency) and receiving bandwidth. Variations in the local chemical environments of individual fluorine atoms can lead to multiple resonances frequencies within one molecule. When imaging, these multiple resonances can give signal location artifacts, which are known as chemical shift artifacts (*i.e.*, misregistration in MRI signals) [34]. The ¹⁹F MRI SNR can be increased by taking the sum of multiple acquisitions, which is called signal averaging. Signal averaging improves SNR by decreasing the noise and making the signal stand out from the existing background noise. However, to increase the SNR, the scanning times must be increased, as several acquisitions are required. In addition, the incorporation of paramagnetic T₁ reducing agents, *e.g.*, paramagnetic metal atoms, can often help to reduce the total measurement time [33].

1.2.7. MRI and Cancer

MRI can be used as a method for discriminating between malignant tumours and normal tissue through the measurement of spin-lattice (T_1) and spin-spin (T_2) magnetic relaxation times. According to previous studies, the relaxation times for the malignant tumours are clearly outside the range of values for the normal tissues, which indicates that malignant tissues can be characterized by an increase in the motional freedom of tissue water molecules [15,23]. The possibility of using magnetic relaxation methods for fast discrimination between benign and malignant surgical specimens has also been studied.

The principle of the NMR technique combines many of the desirable features of an external probe for the detection of internal cancer. In fact, magnetic resonance measurements cause no obvious deleterious effect on biological tissue, the incident radiation consisting of common radio frequencies at right angles to a static magnetic field. The detector is external to the sample, and the method allows one to resolve information emitted by the sample to atomic dimensions. Therefore, the spectroscopist has available for study a wide range of nuclei to obtain evidence of deviant chemical behaviour [23].

1.3. Contrast Agents

Contrast agents are exogenous compounds administered orally or intravenously to patients before the MRI exam, in order to improve the visibility of body structures for clinical diagnostic purposes. Therefore, they can increase the contrast between healthy and damaged tissues, allowing better visualization of the tissues [24,35,36]. These agents act by modifying the relaxation rate of protons in water, creating a change in the MRI signal intensity [37]. However, contrast agents can also be used to pre-label cells *ex vivo* before their transplantation, which is one of the most common approaches in MRI-based cell tracking. Several compounds containing paramagnetic metal ions in complexes and/or nanoparticles have been widely used in the field of medical imaging as contrast agents [38].

The primary criterium for an MRI contrast agent is to affect the relaxation times (T_1 , T_2 and T_2^*) of water protons in tissues. Specific coordinated metal ions can interact freely with water molecules in biological tissue and can influence their nuclear spin relaxation process [38]. Highly stable metal complexes (mostly of gadolinium (Gd^{3+}), but also of Mn^{2+}) have been produced as MRI contrast agents and administered to patients for enhancing the contrast between the diseased and healthy tissues depending on their body biodistribution and kinetics [39].

The ' T_1 agents' affect mainly the T_1 relaxation time of water protons in tissues by decreasing its value, creating hyperintense contrast. This way, the contrast agent ensures the brightening of the tissue of interest. They are generally referred to as paramagnetic agents, which can have one or more unpaired electrons and act as a spinning dipole in a static magnetic field, creating small local field changes. Therefore, this will directly affect the magnetization of the surrounding protons, leading to shorter T_1 relaxation times. Several paramagnetic contrast agents show great efficacy and are clinically used, currently being Gd^{3+} (with seven unpaired electrons) complexes of linear or macrocyclic polyaminocarboxylate ligands, having one water molecule directly bound to Gd^{3+} in its inner-coordination sphere (Figure 1.3). Fast exchange of this water molecule with the bulk water molecules disseminates the proton relaxation of this water to the whole neighbouring tissue [40]. On the other hand, the ' T_2 agents' affect predominantly the T_2 relaxation time of the water protons, making much stronger alterations in the local magnetic field, causing the protons to go out of phase. As a result, the tissue of interest produces a weaker NMR signal, becoming hypointense compared to the surrounding non-targeted tissue. The superparamagnetic iron oxide nanoparticles (SPIO) and dysprosium (Dy^{3+}) complexes are examples of these kinds of agents [35,36].

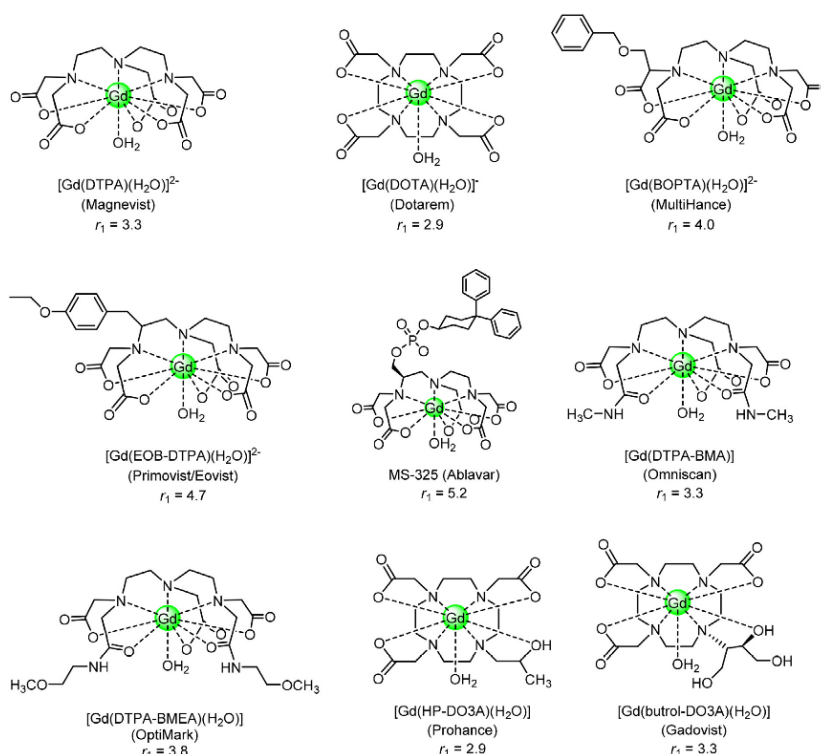


Figure 1.3. Schematic representation of the molecular structure of the currently commercially available Gd^{3+} -containing MRI CAs. Charges in structures are omitted for clarity. The brand names are given between brackets. Relaxivities are in $\text{s}^{-1} \text{mM}^{-1}$ measured in aqueous solution at 1.5 T and 37 °C. (From [40]).

Another class of MRI contrast agents are the chemical exchange saturation transfer (CEST) agents, which generate a decrease in the bulk water proton signal when frequency-selective saturation of their exchangeable protons (N-H, O-H, S-H), in slow exchange with the bulk water, is applied. They are essentially based on amino acids, proteins and sugars, and because they do not contain metal ions, they are often named DIACEST (diamagnetic CEST) agents. The paramagnetic CEST (PARACEST) agents also create contrast based on the CEST principle. However, they do contain paramagnetic metal ions (*e.g.*, Dy³⁺, lanthanide (Ln³⁺), ytterbium (Yb³⁺)) with a high magnetic moment that does not affect much the T₁ and T₂ relaxation times of water, but instead cause large chemical shifts from the free water proton resonance frequency [41,42]. Lastly, there are the ¹⁹F agents that are not considered 'contrast' agents, as there is no background signal to contrast with. Therefore, they are commonly called MRI 'tracers', similar to those used in nuclear medicine. The perfluorocarbons (PFCs), which will be discussed later, are one of the most extensively used tracers [43]. Table 1.1. summarizes the main properties of several MRI CAs.

Table 1.1. Overview of several exogenous contrast agents for MRI and their properties.

Contrast agent	Contrast	Sensitivity	Potential toxicity	Clinical use
Gd ³⁺	Positive	Low	Yes	Yes
Mn ²⁺	Positive	Low	Yes	No
MnO	Positive	Moderate	Yes	No
Dy ³⁺	Negative	Low	Yes	No
(U)SPIO	Negative	High	No	Yes
PARACEST	Negative	Low	Yes	Yes
DIACEST	Negative	Low	No	Yes
PFCs	Positive	Low	No	Yes

1.3.1. Paramagnetic and Superparamagnetic Agents

Paramagnetic contrast agents are commonly used in clinical MRI applications, basically, Gd³⁺ complexes, as one Mn²⁺ complex (Mn-DPDP – Mangafodipir trisodium), or Teslascan, is no longer used clinically.

Gadolinium (III) chelates are the most efficient paramagnetic contrast agents, owing to their seven unpaired electrons. These unpaired electrons of Gd³⁺ generate a magnetic moment capable of increasing the T₁ relaxation time of the surrounding water proton spins,

creating a 'positive' contrast on a T₁-weighted image. These Gd-based contrast agents (GBCAs) are routinely used in more than 40% of the MRI scans clinically used, mainly in brain pathologies affecting the blood-brain-barrier (BBB) [26]. Gd³⁺ has also been used to label and track different types of cells *e.g.*, stem cells, monocytic cells, endothelial progenitor cells and mesenchymal stem cells, in cell transplantation studies. The cellular uptake of these types of chelates occurs by pinocytosis, in which small particles present in the extracellular fluid are internalised into cells, or *via* electroporation. Over the last few years, a variety of paramagnetic agents with improved uptake effectiveness have been designed and applied for cellular imaging, including Gd hexanedione, gadofluorine and liposomal-based Gd³⁺ nanoparticles [38]. The bigger limitation to the use of Gd³⁺ contrast agents is the long-term retention of Gd³⁺ in cells, which might lead to a cytotoxic effect, either to the tissue of interest or to the surrounding tissues. This effect has been reported in patients with impaired kidney function (Nephrogenic Systemic Fibrosis - NSF), where Gd³⁺ complexes are not rapidly cleared, inducing severe fibrosis and even death [36]. Gd³⁺ deposits have also been found in the brain of patients subjected to multiple administrations of GBCAs [44]. The Gd³⁺ toxicity mechanism is not known, but it is assumed that free Gd³⁺ can be taken up in the bone marrow, where it might interfere with the metal ion hemostasis of bone marrow stem cells.

Besides Gd³⁺, Mn²⁺ is another metal ion useful to design a positive contrast agent for T₁-weighted images. The kinetics and behaviour of Mn²⁺ ions in the cells are very identical to the calcium (Ca²⁺) ions, allowing Mn²⁺ ions to enter the cells through ligand- or voltage-gated Ca²⁺ ions channels. Several studies have been published where the use of Mn²⁺-based contrast agents is helpful to study and visualise tissues of interest and for cell tracking. Moreover, manganese oxide (MnO) nanoparticles have been used as an MR contrast agent to detect cells *in vivo* [45]. It is also possible to combine them with superparamagnetic iron oxide particles to detect two cell populations with differential cell contrast (positive vs. negative) at the same time [46].

1.3.2. Fluorinated Agents

Fluorine is the naturally abundant isotope of fluorine, which has a nuclear magnetic resonance sensitivity of 83% compared with hydrogen. Also, it is not radioactive, in contrast to the ¹⁸F isotope that is widely used in PET imaging. When comparing ¹⁹F imaging agents to ¹H contrast agents, additional favourable properties emerge – ¹H contrast agents are detected through their changing of the intrinsic ¹H signal, while ¹⁹F signal is measured directly and therefore, does not depend on the access to mobile water; ¹⁹F has a distinctive resonance frequency from ¹H, appearing as a “second colour” on top of the ¹H anatomical

images with unambiguous detection of the label; also, a linear relationship between signal and amount of ¹⁹F allows an absolute quantification, with corrections needed at very low signal-to-noise regimes; and finally, it has a more positive cytotoxic effect compared to gadolinium and SPIO [33].

The perfluorocarbons (PFCs) compounds are typically used as ¹⁹F imaging agents, which include fluorinated polysaccharides, peptides, and other fluorinated molecules. PFCs consist of a carbon backbone where all hydrogen atoms are replaced by a fluorine atom [47]. These compounds, which are recognised for having many fluorine atoms with identical chemical shifts, are commonly applied in ¹⁹F MRI cell tracking, and they include perfluoro-15-crown-5-ether, linear perfluoropolyethers and perfluorooctyl bromide. PFCs are generally lipophilic and hydrophobic, being synthesized in the form of stable nanoemulsions by high-energy sonication for cell labelling. Usually, the cells are labelled with PFCs nanoemulsions *ex vivo* and then injected into the body. Of note is that PFCs with different chemical shifts allow the visualization of two distinct populations of cells simultaneously *in vivo*. Overall, the choice of the most suitable fluorinated agent is crucial and should be based on the labelling method, use as a responsive probe, specific binding or other activity, stability and toxicity [48].

Studies developed previously have proved that PFC labelling has a minor effect on cell viability and cellular functions, including in differentiation and proliferation, both *in vitro* and *in vivo*. Furthermore, PFCs can be used to probe cell function by sensing intracellular oxygen (O₂) tension. One study combined cell-labelling technology with the oxygen-sensing ability of PFCs, aiming to measure the intracellular oxygen tension in brain tumour models, based on the principle that O₂ molecules can affect the ¹⁹F T₁ relaxation time because they are paramagnetic. This study confirmed that changes in oxygenation following tumour treatment with chemotherapy and immunotherapy provided a reliable imaging biomarker for assessing the efficacy of these kinds of treatments [49].

However, there are some restrictions to the amount of PFCs that can be incorporated into cells. Their size enables the take up of a significant amount of cytoplasmic volume. Therefore, the population number of cells should be higher than a certain threshold for detection, and that might depend on the cell type. The minimal number of cells that can be detected using ¹⁹F tracers varies from 10³ to 10⁵ cells [33].

1.3.3. Porphyrins as Contrast Agents

Porphyrins represent a unique class of heterocyclic tetrapyrrolic organic molecules, which are the most ubiquitous compounds found in nature, among which metal-porphyrin derivatives are found as cofactors of many enzymatic processes. In the last few decades,

researchers have expanded the use of porphyrin-based compounds for medical, drug delivery, biosensing, and bio-imaging purposes. Porphyrins-based molecules have been pioneering theragnostic agents, not only for MRI and photodynamic cancer therapy but also for drug delivery and single-cell imaging [50]. Porphyrins are getting more attention in biomedical applications due to their multiple advantageous features, such as low cytotoxicity in the absence of light, tunable photophysical properties, particularly the absorption and emission wavelength, superficial derivatization, and superior tumour uptake [51,52]. Lately, porphyrins have become accepted not only as photosensitisers and catalysts [53], but also as anticancer drugs.

A successful, rapid and precise diagnostic imaging of soft tissues has relied heavily on MRI [54]. However, almost 50% of MRI examinations need to use MRI contrast agents, which can improve the contrast of MRI images and reduce the high cost and long acquisition times [55,56]. Paramagnetic Gd³⁺ complexes are widely used as MRI contrast agents in clinical applications. However, the Food and Drug Administration (FDA) has restricted the use of these GBCAs since they can cause NSF in patients with renal insufficiency [44,46].

Mn is an essential metal element of cells and plays a fundamental role as a cofactor for enzymes and receptors. The Mn²⁺ ion (electronic configuration 3d⁵) has a relatively high electronic spin ($S = 5/2$), long electron spin relaxation times ($T_{1,2e} \sim 0.1-1$ ns) and a labile coordinated water molecule(s), which can make it act as an advantageous MRI contrast agent [45,46,57]. Free ionic manganese chloride (MnCl₂) is commonly used for manganese-enhanced MRI (MEMRI)-based techniques, in which Mn²⁺ is used as a surrogate marker of cellular calcium influx and a tracer of neuronal connections [46]. MnCl₂ represents one of the earliest examples of a manganese contrast agent, which was the first to be used as CA in dogs [18]. An MnCl₂-based oral contrast agent (Lumenhance®, Bracco Diagnostics) has been evaluated and approved for medical use. However, its neurotoxicity, with an LD₅₀ in mice of 0.3 mmol kg⁻¹ injected intravenously and 1.0 mmol kg⁻¹ injected intraperitoneally, is a major drawback, which prevented its clinical use [46]. However, Mn²⁺ chelates solve the toxicity problem associated with free manganese ions and have been widely used as a blood pool contrast agent. The only clinically approved, injectable Mn(II) contrast agent is the chelate manganese(II) dipyridoxal diphosphate [Mn(DPDP)]⁴⁻ (Mangafodipir trisodium, Teslascan), as a liver CA. The safety factor (LD₅₀/effective dose) of [Mn(DPDP)]⁴⁻ is 540, much higher in comparison to Gd³⁺-diethylenetriamine pentaacetic acid (Gd-DTPA.H₂O, Magnevist®) with a safety factor of 60-100 [46].

Among the Mn²⁺ complexes available, Mn-containing porphyrins are good candidates as effective imaging agents because they not only have higher transmembrane

permeability [58] than that of common Mn²⁺ chelates but also have lower toxicity than that of MnO nanoparticles at a higher dose [59,60]. Nevertheless, Mn³⁺ (high spin 3d⁴, with a reduced electronic spin (S = 2) and shorter electron spin relaxation times (T_{1,2e} ~ 50 ps), which reduces their efficiency as MRI CAs) inserted into the porphyrin ring can in principle be reduced (e.g., by cellular redox buffers like glutathione or ascorbate) to Mn²⁺, with an increased positive contrast effect [61]. However, the reoxidation of Mn²⁺ by oxygen (which is sometimes a reversible process) makes them potentially useful as redox responsive MRI contrast agents (Figure 1.4) [62–65].

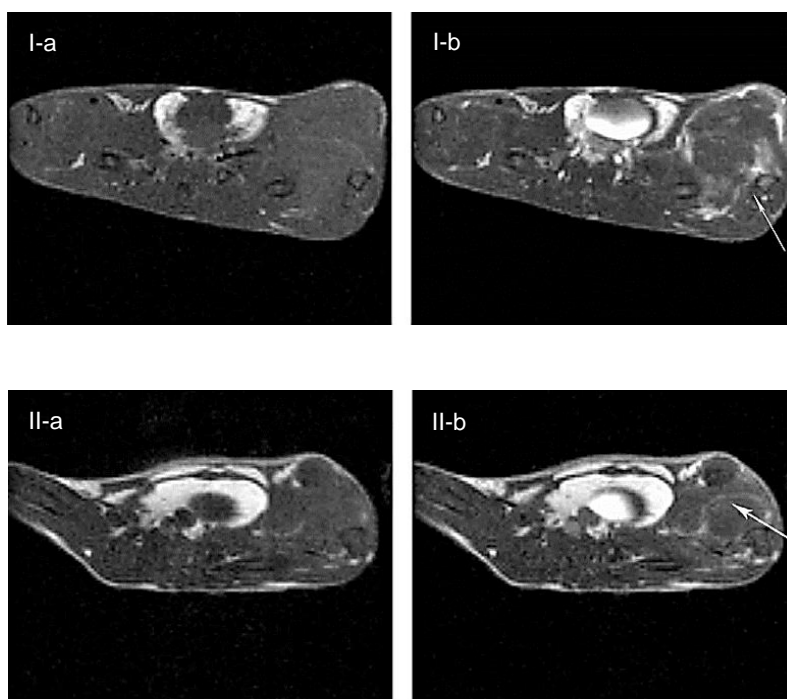


Figure 1.4. T₁-weighted MR images tumour-bearing mice before and after intravenous administration of (I) an Mn-porphyrin complex conjugated with dextran, and Gd-DTPA (II): (a) before the injection; (b) post-injection (30 minutes). The arrows illustrate the enhanced boundary of the tumours. (From [66]).

It has already been shown that MRI contrast agents based on the covalent or non-covalent interaction of a Gd- or Mn-based chelate with a polymer or a macromolecule allows significant amplification of their relaxation efficiency (relaxivity), by increasing the number of paramagnetic ions in the molecule [67] as well as slowing their molecular rotation [68,69], and probably have a substantial effect on their tissue biodistribution and clearance. Therefore, this is an interesting strategy to develop redox responsive molecular imaging probes, which may be useful for the diagnosis of pathophysiological conditions involving oxidative stress or dysregulation of intracellular redox homeostasis, such as chronic inflammation, tumour and ischemia [62].

1.3.4. Redox Responsive Probes

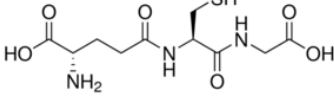
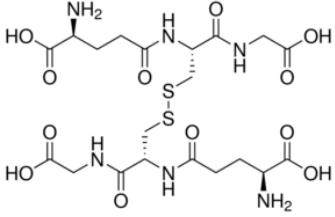
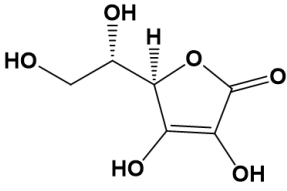
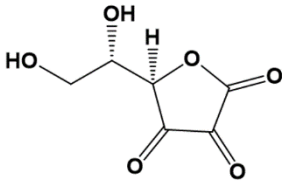
In all living organisms, both intracellular and extracellular redox environments are tightly regulated, which ensures the proper functioning of biological systems. Many pathological processes affect the redox state of local tissues by changing the levels of biological redox species, leading to redox imbalance. For instance, more reactive oxygen species (ROS), *e.g.*, H₂O₂, are produced in regions of inflammation [70]. Also, hypoxia has been found in many solid tumours [71,72]. As a result, both distributions and concentrations of biological redox species can provide information about these pathological processes. The detection and deep-tissue imaging of these oxidative and/or reductive species in living organisms through the oxidation/reduction of the metals ions in the CAs, not only helps to identify and understand these pathological processes but also enables sensitive and accurate diagnosis of redox imbalance-associated diseases. Among the most important antioxidants present in the body, glutathione and ascorbic acid (vitamin C) are two of them.

Glutathione is a tripeptide that plays a crucial role in cellular signalling and antioxidant defences [73]. There are two forms of glutathione – the oxidised form (glutathione disulphide or GSSG) and the reduced form (GSH) (Table 1.2) [74]. Its antioxidant function is mediated by reacting with ROS, reactive nitrogen species (RNS), hydroxyl radicals, hypochlorous acid, and other reactive species, or by acting as an indispensable cofactor for many enzymes, including the glutathione peroxidases and glutathione S-transferases [75]. It can be found in almost every cell of the human body, being distributed at varying levels [76]. Its antioxidant function is mediated by the redox-active thiol group that becomes oxidised when GSH reduces targets molecules. The importance of GSH as a cellular redox buffer is based on the fact that GSH displays a low redox potential ($E'_0 = -240$ mV) and is found in high concentrations in the cells (~ 10-15 mM) [77]. GSH occurs predominantly in its reduced form, except in the endoplasmic reticulum, where it exists mainly as an oxidized form, providing oxidising equivalents to create the adequate environment necessary for the proper folding of proteins [78]. The ratio of GSH/GSSG acts as a reliable marker of cellular redox homeostasis [79]. The GSH/GSSG redox couple along with the NADP/NADPH and FAD/FADH redox couples are responsible for maintaining the appropriate redox balance in the cell, undergoing reversible oxidation or reduction reactions [80].

The ascorbic acid is one of the most important antioxidants, capable of reducing other compounds (*e.g.*, reactive oxygen species), and is converted to its oxidized form, dehydroascorbic acid (DHA), during the process (Table 1.2) [81]. Humans are unable to synthesise this molecule, even though other species can do so [82]. Thus, there is a

recycling mechanism where, after ascorbic acid is used to reduce some oxidised substance and ascorbic acid is, itself, oxidised to DHA, can be reduced back to ascorbic acid by an NADH system or by the action of glutathione [83]. This mechanism is particularly important in red blood cells [81].

Table 1.2. Chemical structures of reduced and oxidized forms of glutathione and ascorbic acid.

Reductants	Reduced Form	Oxidized Form
Glutathione		
Ascorbic Acid		

Accordingly, the development of imaging techniques capable of following *in vivo* tissue redox environment is of utmost interest in clinical research and medical practice, namely in diagnosis, prognosis or monitoring therapeutic response [84]. The aim of developing molecular probes capable of imaging redox activity has had some clinical success. PET probes, such as the radiotracers ^{64}Cu II - diacetyl-bis(N4-methylthiosemicarbazone) (^{64}Cu II-ATSM) and ^{18}F -fluoro-misonidazole (^{18}F -MISO), might have the capacity to predict treatment outcomes in patients undergoing radiotherapy. Also, the same hypoxia targeting mechanism has been extended to MRI contrast agents and fluorescent probes for optical imaging. Furthermore, reversible redox-responsive ^{19}F MRI probes that can identify chronic redox dysregulation have rarely been reported [72].

1.4. Cyclodextrins

Cyclodextrins (CDs) are a family of macrocyclic oligosaccharides linked by α -1,4 glycosidic bonds that have been extensively studied in several fields, after their discovery by Villiers in 1891 [71]. Among them, the most common members are α -, β - and γ -CDs, which are composed of 6, 7 and 8 glucose units, respectively (Figure 1.5). The hydrophobic

cavity of CDs provides them with inclusion capacity with a variety of compounds ranging from small molecules, ions, proteins, and oligonucleotides [85,86].

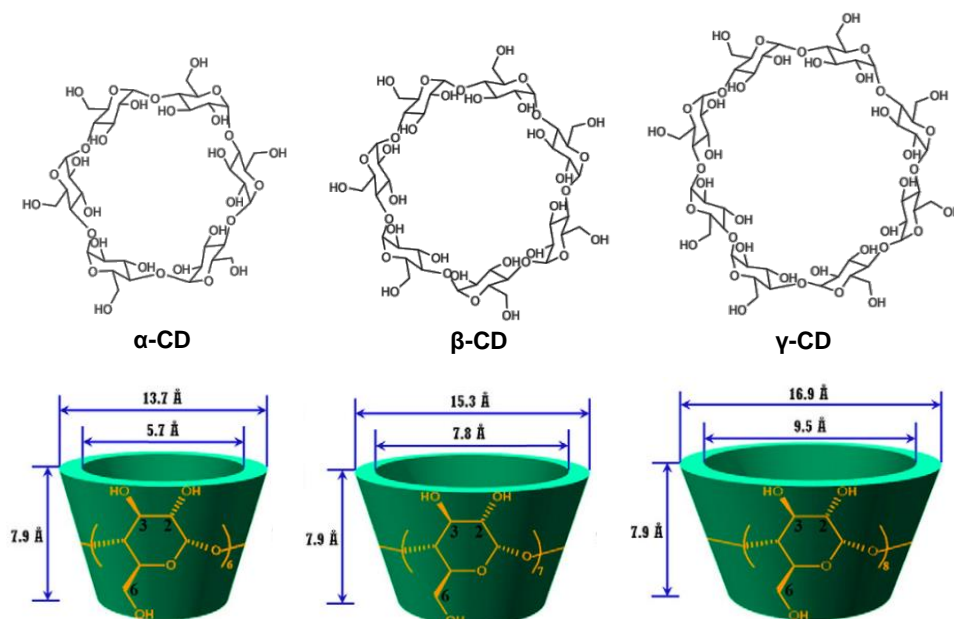


Figure 1.5. Molecular structures (top) and dimensions (bottom) of α -CDs, β -CDs and γ -CDs (from left to right). (Adapted from [86]).

Cyclodextrins are well known for being nontoxic supramolecular hosts, which have been increasingly gaining importance in polymer chemistry, considering their ability to form noncovalent inclusion complexes with hydrophobic guest molecules in aqueous solution, opening the opportunity to generate new supramolecular macromolecular architectures. Thus, the biomedical applications of CDs are extremely attractive due to their low toxicity and low immunogenicity. One of the most used applications is the incorporation of drugs through host-guest interactions in pharmaceutical science and technologies to form inclusion complexes [87]. The related applications include increasing drug solubility and stability, enhancing drug release profiles, alleviating local and system toxicity, and improving drug permeability across biological barriers [88]. The inclusion processes in solution depend on the size, shape and hydrophobicity of the guest molecule. This inclusion process is regulated by van der Waals forces, hydrophobic interactions. Furthermore, hydrogen bonding between the guest and the hydroxyl groups of CDs, the relief of high energy water from the CD cavity, release the strain energy in the molecule rings and dipole-dipole interactions are important. These weak interactions have been used to study the nature of the formation of supramolecules [89].

Porphyrins have become accepted not only as catalysts or photosensitisers, but also as anticancer drugs and CA. Porphyrin derivatives are requisite substances in most living systems. CDs, which are shaped like a truncated cone with a relatively hydrophobic

cavity, incorporate a wide variety of organic compounds to form inclusion complexes [90]. CDs have been used as carriers to improve the aqueous solubility [91], stability against chemical and photochemical degradation [92] and controlled drug release [93]. The formation of inclusion complexes of porphyrin derivatives with CDs changes the photochemical and photophysical properties of porphyrins derivatives [94]. As a result, it is extremely important to examine the formation of supramolecular systems of porphyrin derivatives with CDs.

The aryl groups at the periphery of the porphyrin ring can act as guests of CDs. The formation of inclusion complexes between porphyrins or porphyrin derivatives and β-CDs has been examined by many researchers [90,93,94] to form 2:1 inclusion complexes with porphyrins in an aqueous solution. The use of the β-CD cavity is an excellent way to construct complexes by their noncovalent interaction with 5,10,15,20-tetrakis(phenyl)-porphyrin (TPP), some of them exhibiting remarkable photophysical, photochemical and electronic properties [95]. Also, β-CDs were found to stabilize the low-covalent Mn(II)-TPP in water. The complex of β-CD with Mn(II)-TPP was much more stable than that of β-CD and Mn(III)-TPP [96]. Given the strong interaction of TPP with permethyl-β-CD [97], a supramolecular polymer based on Mn(III)-TPP-mPEG₅₅₀ and bridged bis(permethyl-β-CD) was prepared, and its characterization showed it to be reduced to Mn(II)-TPP-mPEG₅₅₀ by sodium ascorbate, as opposed to free Mn(III)-TPP-mPEG₅₅₀, behaving as an effective positive MRI CA both *in vitro* and *in vivo* [98]. The dependence of the relaxivity of the supramolecular complex of [Mn(III)(TPPS₄)]³⁻ (TPPS₄ = meso-tetra-(4-sulfonatophenyl) porphyrin) with poly-β-CD on its reduction to the Mn^{II} form was also studied *in vitro* [65]. Mn(III)TPP-*p*-CF₃ (5,10,15,20-tetrakis(4-trifluoromethylphenyl) manganese (III) porphyrin), which is a non-water-soluble porphyrin complex that can also form adducts with CDs in solution, has interesting redox, optical and NMR properties, which will be studied in this dissertation.

1.5. *In Vitro* Studies

The development and use of drugs and probes are increasingly growing, having given rise to many concerns and debates among the public, the scientific community, and the regulatory authorities regarding their fate in biological systems [99]. As a result, it is recommended to conduct a complete study of the activity of the probes *in vitro*, capable of ensuring their non-cytotoxicity and high efficiency [100]. Indeed, cell lines are widely used as low maintenance *in vitro* models in drug development, since they are cost-effective and avoid ethical concerns associated with the use of animals.

1.5.1. The Epithelial Cell Model

One of the most important features of the intestinal epithelium is to function as a physical barrier and to allow the uptake of essential nutrients [101]. In fact, intestinal epithelial cells (IECs) are widely used to carry out *in vitro* studies.

Intestinal epithelium cells form a cellular layer that covers the inner surface of the intestine, playing an essential physiological role, namely in food digestion, absorption of nutrients and protection of the human body from microbial infections. In humans, they are regularly replaced, every 4-5 days, through a process of renewal and migration. New IECs are produced by stem cells located in crypts at the base of the intestinal glands [102]. Several cell types can be found in the intestinal epithelium, including enterocytes, Paneth cells, goblet cells and neuroendocrine cells [103]. The enterocytes are the major cell type in the intestinal epithelium and play important roles in nutrient absorption (e.g., of ions, water, sugar, lipids and peptides) and in secreting immunoglobins [104].

The intestinal epithelial cell layer is selectively permeable to a variety of metabolites and digested nutrients, providing a controlled transport of soluble molecules through the paracellular space between the epithelial cells, which is controlled by intercellular tight junctions (TJ) [105]. The protein networks connecting epithelial cells comprise several types of complexes: desmosomes and adherence, gap and tight junctions (Figure 1.6) [106]. These complexes contain transmembrane proteins capable of interacting extracellularly with adjacent cells and intracellularly with proteins that link to the cytoskeleton [104].

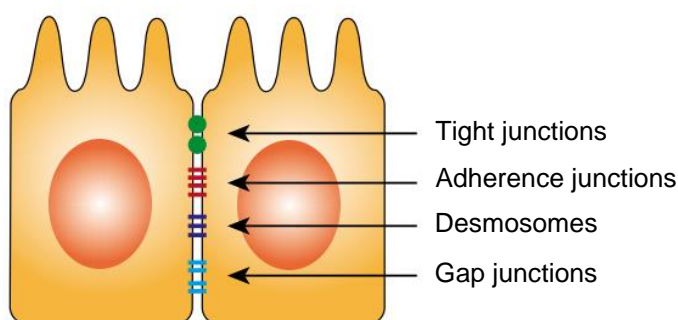


Figure 1.6. Schematic representation of polarized epithelial cells with different types of intercellular contacts. These are essential for the maintenance of barrier function and communication between neighbouring cells. (From [107]).

At least four different transport mechanisms are allowing the selective uptake and transport of macromolecules across the epithelial cell layer (Figure 1.7). Paracellular transport is regulated by complex intracellular processes which tune the permeability of the tight junction complex and allow the transport of molecules through the epithelium. Passive

diffusion through the cell membrane can release some nutrients or microbial metabolites into the basolateral side. The other transport mechanisms are the vesicle-mediated transcytosis and the carrier-mediated uptake and diffusion through the epithelial cell layer [108]. Moreover, each of these mechanisms relies on the physicochemical properties of the compound to be transported, its molecular weight and size, stability, ability to interact with the plasma membrane and charge distribution [109].

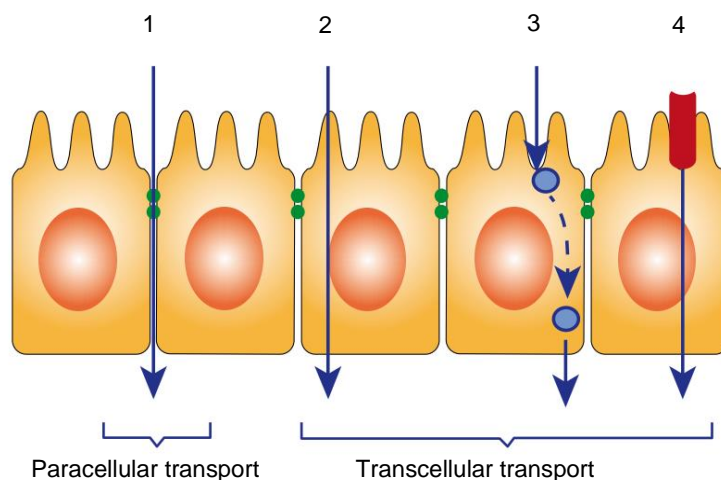


Figure 1.7. Different mechanisms of absorption and transport through the intestinal epithelium: (1) paracellular transport; (2) passive diffusion of molecules from the apical to the basolateral side; (3) vesicle-mediated transcytosis; (4) carrier-mediated uptake and diffusion through the epithelial cell layer. (From [107]).

When applied *in vivo*, other parameters not directly associated with the molecule in question can influence the uptake and the transepithelial transport, *i.e.*, intestinal motility, interactions with other molecules from the diet or the digestive process (*e.g.*, bile salts and enzymes), as well as the solubility in the mucus layer [110]. Thus, the use of intestinal epithelial cells for absorption studies may have some limitations. Nevertheless, they are considered very useful model systems for such purposes.

Overall, the single layer of epithelial cells in the intestine acts as a rate-limiting barrier for the transport and uptake of compounds between the lumen and the body interior. Therefore, it is possible to assess absorption and active and passive transport processes through the intestinal epithelium when differentiated human epithelial cell monolayers are cultured *in vitro* [111]. Among the available epithelial cell lines, Caco-2 has been found particularly suitable for these types of studies, as was chosen for the present work (as explained below).

1.5.2. The Caco-2 Cell Line

1.5.2.1. Origin

In the 1970s, several epithelial cells lines were established from gastrointestinal tumours, with the aim of identifying and studying mechanisms of cancer development and effects of chemotherapy. Partly due to the heterogeneity of primary intestinal epithelial cells, both in morphology and function (e.g., small bowel enterocytes, enteroendocrine cells, goblet cells), there was a need for differentiating the tumour cells into more specialized cell types [112]. Some of the cell lines were differentiated by adding synthetic or biological factors to the culture medium. In particular, one of them exhibited a singular property, being able to discriminate spontaneously when reaching confluence – the Caco-2 (Cancer coli-2) cell line, established by Jorgen Fogh at the Sloan-Kettering Cancer Research Institute in 1977 [113]. Caco-2 cells were isolated from a primary colonic tumour in a 72-year-old Caucasian male using the explant culture technique. This cell line forms moderately well-differentiated adenocarcinomas, in nude mice, consistent with colonic primary grade II [114].

1.5.2.2. Features and Mechanisms

The Caco-2 cells monolayers (Figure 1.8) have been widely accepted as an effective *in vitro* model to predict intestinal drug permeability in humans, considering that the permeability of the gastrointestinal membrane is one of the key factors that define the absorption and bioavailability of some types of drugs [111]. Indeed, one of the most advantageous properties of Caco-2 cells is their ability to spontaneously differentiate into a monolayer with many properties similar to those characteristics of absorptive human enterocytes (e.g., with brush border layer as found in the small intestine) [47]. The Caco-2 cell line is heterogeneous, *i.e.*, comprises cells with slightly distinctive characteristics in terms of morphology and function.

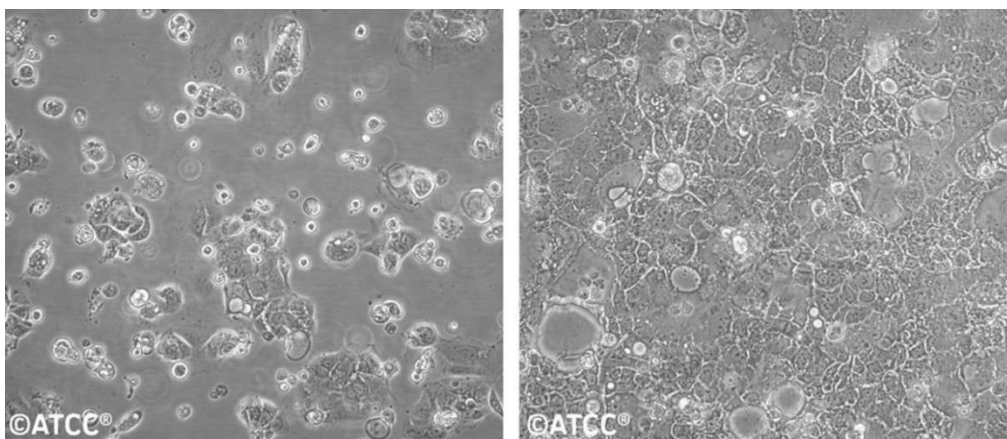


Figure 1.8. Caco-2 cells observed under an inverted optical microscope. On the left, the cells are seeded at low density. On the right, the cells exhibit high density. The emergence of the monolayer is notorious. (Images supplied by ATCC® (American Type Culture Collection) [115]).

After reaching confluence, Caco-2 cells start to polarise, acquiring a typical apical brush border displaying microvilli [116]. Also, tight junctions are formed between adjacent cells. It should be highlighted that Caco-2 cells express many of the enzyme markers and transport systems typical of enterocytes - namely lactase, aminopeptidase N, sucrase-isomaltase and dipeptidyl-peptidase IV. In addition, markers of colonocytes are also present in Caco-2 cells [117].

1.5.2.3. Stability, Consistency and Reproducibility

Over 40 years have passed since the establishment of the Caco-2 cell line, which has been propagated in many laboratories worldwide. Considering the distinct culture conditions and the different number of passages that these cells can be exposed to, they have often acquired distinct properties. Subsequently, the expression of differentiation markers typical of enterocytes changes with an increasing number of passages [118]. In addition, other parameters such as the transepithelial electric resistance (TEER) and the proliferation rate have been reported to increase with the passage number [119]. It has also been found that late passage cells may start growing in multilayers, which can complicate comparison with previous results based on early passage cultures (monolayers). Accordingly, data obtained under identical experimental conditions in different laboratories may not be directly comparable. To overcome this difficulty, a range of cloned Caco-2 cell lines has been established and characterized in the literature [112,120].

1.5.2.4. Relevance to Human *In Vivo* Conditions

The rapid increase in the number of compounds that are being synthesized and tested as potential drugs has resulted in increasing pressure for developing assays suitable for an accurate screening, regarding both pharmacokinetic properties (e.g., absorption, transport, metabolism) and pharmacological activity, to keep pace with the drug design pipeline [121].

As previously discussed, Caco-2 monolayers are well known to allow a reliable correlation in studies on the absorption of drugs and other compounds after oral intake, in humans. Several experiments have been carried out to compare Caco-2 permeability coefficients with absorption data, a high correlation having been found especially when the compounds are transported by passive paracellular transport mechanisms [122].

Previous studies suggest that there are variations between gene expression profiles of transformed epithelial cell lines such as the Caco-2 cells, even though they have been found to express a great number of enzymes and transporter proteins present in the human intestinal epithelium [123,124]. Due to this fact, data from experiments using the Caco-2 cell model cannot be directly compared to the *in vivo* situation [108]. Nevertheless, intestinal epithelial cell models such as Caco-2 have many advantages, due to their simplicity and reproducibility, allowing an inter-laboratory comparison of the results.

1.5.2.5. Applications

Cell culture assays have allowed the exploration of interesting new possibilities in many scientific disciplines. If handled correctly, the Caco-2 cell line is considered a key cell line in the drug discovery workflow, providing not only essential information on the biological and biochemical basis of barrier properties of the intestinal mucosa but also relevant data regarding the absorption and permeability of drugs and dietary components, which is paramount for both the pharmaceutical and the food industry [124]. Therefore, the Caco-2 cell line has been used in a wide number of applications, among them studies of: the mechanisms and the effects of microbiota, microbiota metabolites and bioactive food components on the barrier function of the intestinal epithelium [125]; the pathways involved in drug or food components transportation across the intestinal epithelium [126]; the potential cytotoxic effects of drug candidates or food metabolites [127]; the optimal physicochemical properties of bioactive molecules for passive diffusion *via* the paracellular or transcellular pathways across the intestinal epithelium [128]; the interactions between bioactive molecules during transport across the intestinal epithelium [129].

1.5.2.6. Advantages and Disadvantages

The Caco-2 cells can spontaneously differentiate to express morphological and functional characteristics of mature small intestinal enterocytes. Among the intestinal epithelial cells used for *in vitro* assays, this cell line is one of the most accurately compared to the *in vivo* situation [120,130]. They express the majority of receptors, transporters and drug-metabolizing enzymes, such as aminopeptidase, esterase and sulfatase, found in the normal epithelium, although no P450 metabolizing enzyme activity has been reported in these cells [129].

However, the Caco-2 cell model has several limitations in comparison with normal human intestinal epithelium. Firstly, the normal epithelium contains more than one type of cell type and not only enterocytes. Secondly, the Caco-2 cells were originally derived from a tumour, which has numerous biological differences compared to a normal enterocyte [120]. Moreover, these cells are colonic in origin and not from the small intestine [112]. Also, several non-cellular parameters can affect the absorption of a compound in cells, influencing its *in vivo* uptake [108]. Although in general, the Caco-2 cell line provides a powerful tool for establishing and determining several properties of the human intestinal epithelium, one has to be careful in extrapolating data from *in vitro* models to the *in vivo* case.

1.6. Aim of the Work

The aim of this study was the development of a biocompatible water-soluble supramolecular complex as a redox responsive bimodal ^1H - ^{19}F MRI probe, based on the inclusion of the water-insoluble Mn(III)TPP-*p*-CF₃ fluorinated porphyrin into γ -CD.

The first step of the work was the synthesis and characterization (*via* UV-Vis and NMR) of the biocompatible redox probe, in terms of: a) molar absorption coefficients, ability to be reversibly converted between the Mn(III) and Mn(II) oxidation states through the addition of reductants and reoxidation in the presence of oxygen; b) effectiveness to be applied as a potential probe for MRI by studying the ^1H and ^{19}F NMR spectra and relaxation times in the two oxidation states; and c) capability to form stable inclusion complexes with cyclodextrins in order to increase its hydrosolubility, thus favouring drug administration and absorption.

The second goal of the study was to assess the potential antiproliferative and cytotoxic activities of MnTPP-*p*-CF₃ and its CD-inclusion complex, by MTT and SRB *in vitro* assays using the Caco-2 cell line.

Materials and Methods

Synthesis and Characterization of a Biocompatible Fluorinated Mn(III)-Porphyrin as a Redox Responsive ¹⁹F-NMR/T₁ Bimodal MRI Contrast Agent

2.1. Materials

Commercially available reagents were purchased with the highest quality available and were used as received. All the materials used in the experimental work described in this dissertation are listed in Table 2.1.

Table 2.1. List of materials used in the experimental work.

Material	Manufacture	Reference	Supplier
Materials used in probe characterization			
Acetic acid (CH ₃ CO ₂ H, ≥ 99.5%)	Sigma-Aldrich®	W200603	Sigma-Aldrich® Química S.A., Sintra, Portugal
Ascorbic acid (C ₆ H ₈ O ₆ , ≥ 99.0%)	Fisher Scientific	AAA1561336	Fisher Scientific, Portugal
Chloroform-d (CDCl ₃ , 99.8 atom % D)	Sigma-Aldrich®	151823	Sigma-Aldrich® Química S.A., Sintra, Portugal
Deuterium oxide (D ₂ O, 99.9 atom % D)	Sigma-Aldrich®	151882	Sigma-Aldrich® Química S.A., Sintra, Portugal
Dichloromethane (CH ₂ Cl ₂ , ≥ 99.8%)	Sigma-Aldrich®	270997	Sigma-Aldrich® Química S.A., Sintra, Portugal
Dimethyl sulfoxide (DMSO, C ₂ H ₆ OS, 99+%)	Alfa Aesar	A13280	Fisher Scientific, Portugal
Dimethyl sulfoxide-d ₆ [DMSO-d ₆ , (CD ₃) ₂ SO, 99.9 atom %D]	Sigma-Aldrich®	151874	Sigma-Aldrich® Química S.A., Sintra, Portugal
Glacial acetic acid (H ₃ CCOOH, ≥ 98%)	VWR Chemicals	84528.290	VWR International, Alfragide, Portugal
L-Glutathione (C ₁₀ H ₁₇ N ₃ O ₆ S, 98%)	Fluorochem	213215	Fluorochem, Cymit Quimica S.L.
Manganese (II) acetate [(CH ₃ CO ₂) ₂ Mn, 98%]	Sigma-Aldrich®	330825	Sigma-Aldrich® Química S.A., Sintra, Portugal
Methanol (CH ₃ OH, 99.8%)	Sigma-Aldrich®	322415	Sigma-Aldrich® Química S.A., Sintra, Portugal
Methyl-β-Cyclodextrin (C ₅₄ H ₉₄ O ₃₅ , ≥ 98%)	Sigma-Aldrich®	C4555	Sigma-Aldrich® Química S.A., Sintra, Portugal
Nitrobenzene (C ₆ H ₅ NO ₂ , 99%)	Alfa Aesar	A10585	Fisher Scientific, Portugal
Sodium acetate (CH ₃ COONa, ≥ 99%)	Sigma-Aldrich®	S2889	Sigma-Aldrich® Química S.A., Sintra, Portugal
Sodium sulphate anhydrous (Na ₂ SO ₄ , ≥ 99.0%)	Sigma-Aldrich®	238597	Sigma-Aldrich® Química S.A., Sintra, Portugal

Table 2.1. (cont.) | List of materials used in the experimental work.

Tetrahydrofuran RPE (THF, C ₄ H ₈ O)	Carlo Erba Reagents	487303	Carlo Erba - LaborSpirit, Loures, Portugal
¹ H-Pyrrole (C ₄ H ₅ N, 99%)	Fluorochem	034290	Fluorochem, Cymit Quimica S.L.
4-(Trifluoromethyl)benzaldehyde (C ₈ H ₅ F ₃ O, 98%)	Fluorochem	002181	Fluorochem, Cymit Quimica S.L.
4-(2-Hydroxyethyl)piperazine-1-ethanesulfonic acid (HEPES, C ₈ H ₁₈ N ₂ O ₄ S, ≥ 99.5%)	Sigma-Aldrich®	H4034	Sigma-Aldrich® Química S.A., Sintra, Portugal
γ-Cyclodextrin (C ₄₈ H ₈₀ O ₄₀ , ≥ 98%)	Sigma-Aldrich®	C4892	Sigma-Aldrich® Química S.A., Sintra, Portugal
Materials used in the <i>in vitro</i> assays			
Acetic acid (CH ₃ CO ₂ H, ≥ 99.8%)	Sigma-Aldrich®	71251	Sigma-Aldrich® Química S.A., Sintra, Portugal
Dimethyl sulfoxide (DMSO, C ₂ H ₆ OS, ≥ 99.9%)	Sigma-Aldrich®	472301	Sigma-Aldrich® Química S.A., Sintra, Portugal
Disposable plastic material routinely used in cell culture (culture flasks, Eppendorfs, centrifuge tubes, serological pipettes, and syringes)	Orange Scientific	*	Frilabo, Maia, Portugal
Ethanol (CH ₃ CH ₂ OH, ≥ 99.8%)	Sigma-Aldrich®	51976	Sigma-Aldrich® Química S.A., Sintra, Portugal
Ethylenediaminetetraacetic acid (EDTA, ≥ 98.5%)	Sigma-Aldrich®	ED	Sigma-Aldrich® Química S.A., Sintra, Portugal
Fetal bovine serum (FBS)	Life Technologies®	10270-106	Alfagene®, Carcavelos, Portugal
Hydrochloric acid (HCl, 37%)	Sigma-Aldrich®	320331	Sigma-Aldrich® Química S.A., Sintra, Portugal
Methanol (CH ₃ OH, ≥ 99.8%)	Sigma-Aldrich®	179337	Sigma-Aldrich® Química S.A., Sintra, Portugal
Minimum Essential Medium (MEM)	Sigma-Aldrich®	56416C	Sigma-Aldrich® Química S.A., Sintra, Portugal
Minimum Essential Medium non-essential amino acid solution (100x solution)	Sigma-Aldrich®	M7145	Sigma-Aldrich® Química S.A., Sintra, Portugal
Penicillin – Streptomycin solution (Pen/Strep, 10.000 units penicillin and 10 mg streptomycin/mL)	Sigma-Aldrich®	P4333	Sigma-Aldrich® Química S.A., Sintra, Portugal
Potassium chloride (KCl, ≥ 99.9%)	Sigma-Aldrich®	P5405	Sigma-Aldrich® Química S.A., Sintra, Portugal
Potassium phosphate monobasic (KH ₂ PO ₄ , ≥ 99.0%)	Sigma-Aldrich®	P5379	Sigma-Aldrich® Química S.A., Sintra, Portugal

Table 2.1. (cont.) | List of materials used in the experimental work.

Sodium bicarbonate (NaHCO ₃ , ≥ 99.7%)	Sigma-Aldrich®	S5761	Sigma-Aldrich® Química S.A., Sintra, Portugal
Sodium chloride (NaCl, ≥99.0%)	Sigma-Aldrich®	S9888	Sigma-Aldrich® Química S.A., Sintra, Portugal
Sodium phosphate dibasic (Na ₂ HPO ₄ , ≥ 99%)	Sigma-Aldrich®	S0876	Sigma-Aldrich® Química S.A., Sintra, Portugal
Sulforhodamine B (SRB, 75%)	Sigma-Aldrich®	230162	Sigma-Aldrich® Química S.A., Sintra, Portugal
Thiazolyl blue tetrazolium bromide (MTT, C ₁₈ H ₁₆ BrN ₅ S, 98%)	Sigma-Aldrich®	M2128	Sigma-Aldrich® Química S.A., Sintra, Portugal
Tris(hydroxymethyl)aminomethane (Tris, ≥ 99.8%)	Sigma-Aldrich®	252859	Sigma-Aldrich® Química S.A., Sintra, Portugal
Trypan Blue 0.4% (w/v) (TB, C ₃₄ H ₂₈ N ₆ O ₁₄ S ₄)	Sigma-Aldrich®	T8154	Sigma-Aldrich® Química S.A., Sintra, Portugal
Trypsin (10x solution, 25g porcine trypsin <i>per</i> liter in 0.9% sodium chloride)	Sigma-Aldrich®	T4549	Sigma-Aldrich® Química S.A., Sintra, Portugal
24-well cell culture plates	Corning Incorporated	3524	Sigma-Aldrich® Química S.A., Sintra, Portugal
48-well cell culture plates	Corning Incorporated	3548	Sigma-Aldrich® Química S.A., Sintra, Portugal

*References for each material can be found on the manufacture's website (<https://www.frilabo.pt/categoria-produto/consumiveis/consumiveis-cultura-celulas/>).

2.2. Biological Material

The Caco-2 epithelial human colorectal adenocarcinoma cell line was purchased from the European Collection of Cell Cultures (ECACC; Salisbury, UK; ECACC no. 86010202), as a cryopreserved cellular suspension. In our laboratory, passage #52 was assigned to the culture initiated from the frozen aliquot supplied by ECACC and was used between passage numbers #52 to #58.

2.3. Equipment

All the equipment used in the experimental work described in this dissertation is listed in Table 2.2.

Table 2.2. List of equipment used in the experimental work.

Equipment	Manufacturer	Model	Distributor
Equipment used in probe characterization			
Balance (analytical)	Mettler Toledo	AB204-S	Soquímica, Lisboa, Portugal
Kinetic system with laser	Not know	Not know	Not know
Magnetic stir plate	Heidolph	Hei-Standard	Soquímica, Lisboa, Portugal
Nuclear magnetic resonance spectrometer	Bruker	AvanceCore 400 MHz	Bruker, Lisboa, Portugal
Rotary evaporator	Heidolph	Hei-VAP Core	Soquímica, Lisboa, Portugal
Ultraviolet-Visible absorption spectrophotometer	Hitachi	U-2010	Hitachi Vantara, Portugal
Vacuum pump	VWR™	10160-722	VWR International, Alfragide, Portugal
Valve-regulated vacuum pump	Heidolph	Rotovac Valve Tec	Soquímica, Lisboa, Portugal
Equipment used in the <i>in vitro</i> assays			
Balance (analytical)	Radwag®	AS 220.R2	Not know
Bench autoclave	Prestige Medical	220140 Omega Media	Ezequiel Panão Jorge, Electromédica, Coimbra, Portugal
Camera	Olympus	DP20	Not know
Camera monitor	SyncMaster 151s	00124110	Samsung, Lisboa, Portugal
Centrifuge with cooling	MPW Medical Instruments®	MPW-350R	MPW, Frilabo, Portugal
CO ₂ incubator	Sanyo	COM-19AIC(UV)	Sanyo, Frilabo, Portugal
Drying oven	Thermo Fisher Scientific	Heraeus	Thermo Fisher Scientific, Portugal
Biobank	Cryo Diffusion S.A.S.	B2048	Not know
Magnetic stir plate	Heidolph	Hei-Standard	Soquímica, Lisboa, Portugal
Microplate reader	BioTek	µQuant	BioTek, Portugal
Optical microscope	Olympus	CKX41	Olympus®, Portugal

Table 2.2. (cont.) | List of equipment used in the experimental work.

pH meter	Crison Instruments	Basic 20+	Crison, Rotoquímica, Portugal
Unstirred thermostatic bath	Clifton®	NE1-25	Frilabo, Portugal
Vertical laminar flux cabinet	Kojair®	020236 BW-100	BioWizard, Frilabo, Portugal
Vortex mixer	IKA®	MS2 Minishaker	IKA® Works, Frilabo, Portugal
Thermostatic water bath	Clifton®	NEI-14 79004	Frilabo, Portugal
Water purification system	Millipore S.A.	Simplicity® SIMS50000	Interface, Equipamento e Técnica Lda., Amadora, Portugal

2.4. Composition of the Solutions Used

Ultrapure (Millipore) water was used in the preparation of all solutions for the *in vitro* assays. The solution of Mn(III)TPP-*p*-CF₃ in DMSO was sterilised by filtration using a 0.22 µm pore size syringe filter. The solution of γ-CD*Mn(III)TPP-*p*-CF₃ in DMSO:H₂O, in turn, could not be filtered because the dimensions of the complex were too high for the porosity of the filter, causing its retention. The MEM culture medium was filtrated using a vacuum-driven filter unit. The filtrations were carried out under sterile conditions, in a laminar flow cabinet. All other solutions were autoclaved at 121°C and 1.39 atm, for around 15-20 min.

All the solutions used for the *in vitro* assays are listed in Table 2.3.

Table 2.3. List of solutions used for the *in vitro* assays.

Solution	Components	pH	Storage
Cell culture routine			
MEM culture medium	- 9.53 g MEM - 2.2 g NaHCO ₃ - 1000 mL (final volume) ultrapure water	7.4	4°C
MEM 10% (v/v) FBS/1% Pen/Strep	- 100 mL FBS - 10 mL MEM non-essential amino acid solution - 10 mL Penicillin/Streptomycin solution	7.4	4°C
Phosphate Buffered Saline (PBS) 10x	- 87.7 g (15 mM) NaCl - 2 g (27 mM) KCl - 6.1 g (43 mM) Na ₂ HPO ₄ - 2 g (15 mM) KH ₂ PO ₄ - 1000 mL of ultrapure water	7.4	Room temperature

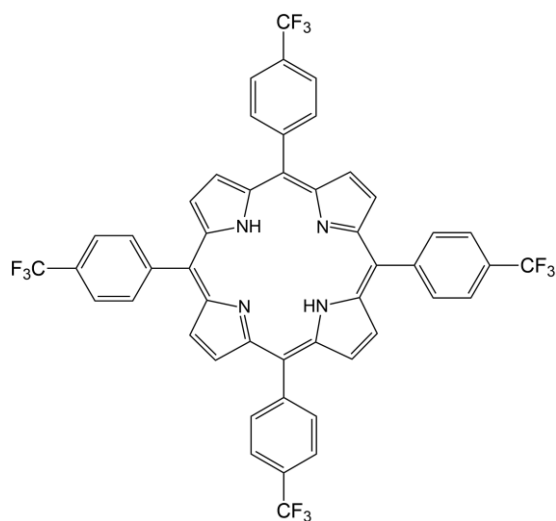
Table 2.3. (cont.) | List of solutions used for the *in vitro* assays.

PBS 1x	- 100 mL PBS 10x - 900 mL ultrapure water	7.4	Room temperature
Trypsin-EDTA 1x	- 90 ml PBS 1x - 10 mL Trypsin 10x - 20 mg EDTA	7.4	4°C
Tested agents			
Mn(III)TPP- <i>p</i> -CF ₃ in DMSO	- 10 mg Mn(III)TPP- <i>p</i> -CF ₃ - 20 mL DMSO		Room temperature
γ-CD*Mn(III)TPP- <i>p</i> -CF ₃ in DMSO:H ₂ O	- 5 mL (5 mM) Mn(III)TPP- <i>p</i> -CF ₃ in DMSO - 20 mL (5 mM) γ-CD in ultrapure water		Room temperature
MTT assay			
Thiazolyl blue tetrazolium bromide solution	- 17 mg MTT - 34 mL PBS		-20°C
SRB assay			
Methanol 1% (v/v) in acetic acid	- 5 mL acetic acid - 495 mL methanol		-20°C
1% (v/v) acetic acid	- 10 mL acetic acid - 990 mL deionised water		Room temperature
SRB 0.5% (v/v)	- 2.5 g Sulforhodamine B - 500 mL acetic acid solution 1% (v/v)		Room temperature
Tris 10 mM	- 1.2 g Tris base - 1000 mL ultrapure water	10	Room temperature

2.5. Synthesis of the Mn(III)TPP-*p*-CF₃ Probe

2.5.1. Synthesis of Free-base 5,10,15,20-tetrakis(4-trifluoromethylphenyl) porphyrin (TPP-*p*-CF₃)

A mixture of glacial acetic acid (140 mL) and nitrobenzene (70 mL) was added into a round bottom flask, and it was heated at 120°C, for ten minutes. Then, 4-(trifluoromethyl)benzaldehyde (5.5 mL, 0.04 mol) and 1H-pyrrole (3 mL, 0.04 mol) were added dropwise. The reaction was left in a reflux system with stirring for two hours. After the reaction was completed, the mixture was cooled with iced, and methanol was added to help precipitation. In the end, vacuum filtration was performed, and the synthesized porphyrin was collected. The chemical structure of TPP-*p*-CF₃ is presented below (Figure 2.1).



Yield: 10%

RMN ^1H (400 MHz, CDCl₃) δ ppm: 8.82 (s, 8 H $_{\beta}$), 8.34 (d, 4 H-3' and H-5'), 8.05 (d, 4 H-2' and H-6'), -2.80 (s, 2 H $_{\text{NH}}$);

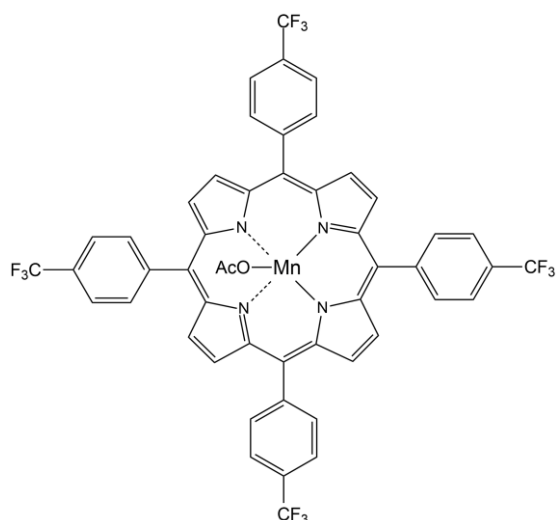
RMN ^{19}F (376.5 MHz, CDCl₃) δ ppm: -62.10 (s, 4 F);

HRMS (ESI-TOF) m/z: calculated for C₄₈H₂₆F₁₂N₄: 886.2036, obtained 887.4532 [M+H]⁺.

Figure 2.1. Chemical structure of TPP-*p*-CF₃.

2.5.2. Complexation of TPP-*p*-CF₃ with manganese

The former free-base porphyrin (100 mg, 0.113 mmol), manganese (II) acetate (156 mg, 0.903 mmol) and sodium acetate (370 mg, 0.451 mmol) were dissolved in acetic acid (3 mL). The mixture was stirred for two hours at 80°C and controlled by UV-Vis spectroscopy. After complete conversion to the manganese complex, the reaction mixture was extracted several times with dichloromethane/water to remove the excess salt that might be still present in the solution. The organic layer was dried over anhydrous sodium sulphate and concentrated under vacuum. The chemical structure of Mn(III)TPP-*p*-CF₃ is provided below (Figure 2.2).



Yield: 85%

RMN ^1H (400 MHz, DMSO-*d*₆) δ ppm: 7.85 (s, 8 H $_{\beta}$);

RMN ^{19}F (376.5 MHz, DMSO-*d*₆) δ ppm: -61.12 (s, 12 F).

Figure 2.2. Chemical structure of Mn(III)TPP-*p*-CF₃.

2.6. Characterization of the Mn(III)TPP-*p*-CF₃ Probe

2.6.1. Determination of Molar Absorption Coefficients

With the purpose of determining the molar absorption coefficients (ϵ) of the synthesized porphyrin, a stock solution of Mn(III)TPP-*p*-CF₃ (0.370 mg, 3.71×10^{-4} mmol) was prepared by adding it with THF (25 mL) to an application suitable concentration of 1.50×10^{-5} M. Thereafter, multiple solutions were prepared by diluting 0.5 mL (7.50×10^{-7} M), 1 mL (1.50×10^{-6} M), 2 mL (3.00×10^{-6} M), 5 mL (7.50×10^{-6} M), 6 mL (9.00×10^{-6} M), 7 mL (1.05×10^{-5} M) and 9 mL (1.35×10^{-5} M) of the former solution in THF, bringing the total volume to 10 mL. The absorbance of the different solutions was monitored by UV-Vis spectroscopy in order to establish the values of the molar absorption coefficients not only for the Soret band but also for the Q bands of the porphyrin.

2.6.2. Reduction of Mn(III)TPP-*p*-CF₃

A solution of HEPES buffer (pH 7.4) was prepared by adding HEPES (2.830 g, 9.99 mmol) and sufficient water to bring the total volume to 100 mL. After that, a solution of ascorbic acid in HEPES buffer was prepared by dissolving ascorbic acid (2.3 mg, 0.013 mmol) in 5 mL of the previously made solution (2.61×10^{-3} M).

The Mn(III)TPP-*p*-CF₃ porphyrin (10 mg, 0.010 mmol) was diluted in THF (20 mL) to a final concentration of 5.0×10^{-4} M. Then, 0.5 mL of that solution was transferred into a volumetric flask and THF was added to bring the total volume to 20 mL, reaching a final concentration of 1.25×10^{-5} M. The same procedure was repeated using DMSO as a solvent. The reduction was monitored by UV-Vis spectroscopy by adding different volumes of ascorbic acid to the stock solution placed in the quartz cell.

The reduction experiment was replicated using glutathione as a reducing agent. Thus, a solution of L-glutathione (40 mg, 0.013 mmol) in buffer HEPES was prepared (2.61×10^{-3} M). Thereafter, different volumes of glutathione were added to the Mn^{III} solution placed in the quartz cell. Once again, the experiment was made using both solvents – THF and DMSO. The conversion of Mn^{III} to Mn^{II} was monitored by UV-Vis spectroscopy.

2.6.3. ¹H and ¹⁹F NMR Study

NMR spectroscopy is a powerful and unique technique due to its versatility, capable of elucidating structure and dynamics in macromolecular and supramolecular systems over wide ranges in space and time [131]. The Mn(III)TPP-*p*-CF₃ complex was characterized by

both ¹H and ¹⁹F NMR spectroscopy to assess the potential of this complex for application in ¹⁹F MRI. Hence, a solution of Mn(III)TPP-*p*-CF₃ (0.659 mg, 6.60 × 10⁻⁴ mmol) was prepared in DMSO-d₆ to a final concentration of 6 × 10⁻⁴ M. The reduction of Mn^{III} to Mn^{II} with ascorbic acid was also followed by NMR spectroscopy. The former solution was prepared by adding ascorbic acid (1.06 mg, 6.0 × 10⁻³ mmol) in deuterium oxide to a final concentration of 6 × 10⁻³ M. All ¹H and ¹⁹F NMR spectra were recorded at 400 MHz and 376.5 MHz, respectively, on a 400 MHz Bruker Avance III NMR spectrometer, at room temperature (25 °C). Proton and ¹⁹F chemical shifts are given in parts per million (ppm) relative to tetramethylsilane (TMS) and trifluorotoluene in chloroform-d, respectively, which were used as internal standards (δ 0.00 ppm for ¹H and -63.72 ppm for ¹⁹F).

2.6.4. Reduction Kinetics of Mn(III)TPP-*p*-CF₃

For this experiment, both solutions of Mn(III)TPP-*p*-CF₃ in DMSO-d₆ and ascorbic acid in D₂O were prepared according to section 2.6.3.

The conversion of Mn^{III} to Mn^{II} was monitored by the decrease of the fluorine singlet in ¹⁹F NMR, which represents the decrease of the concentration of the Mn^{III} complex in solution. The decrease of Mn(III)TPP-*p*-CF₃ in the presence of 2.5 equivalents of ascorbic acid was monitored over time, particularly between 3 and 40 minutes after the addition of the reducing agent. ¹⁹F NMR spectra were recorded at 376.5 MHz, on a 400 MHz Bruker Avance III NMR spectrometer, at room temperature (25 °C). The excess of ascorbic acid used in the experiment assured pseudo-first-order kinetics regarding the Mn^{III} complex.

2.6.5. ¹⁹F NMR Relaxometry

Two solutions of TPP-*p*-CF₃ and Mn(III)TPP-*p*-CF₃ were prepared in CDCl₃ to a final concentration of each of 6 × 10⁻⁴ M. The longitudinal and transverse ¹⁹F relaxation times of TPP-*p*-CF₃ and Mn(III)TPP-*p*-CF₃ complexes in CDCl₃ were measured on a 400 MHz Bruker Avance III NMR spectrometer (ν(¹⁹F) = 376.5 MHz, 25 °C). An inversion recovery pulse sequence was used for T₁ determination and a CPMG spin-echo sequence to determine T₂, which was compared with the T₂* values obtained from the signal linewidths.

2.7. Inclusion of Mn(III)TPP-*p*-CF₃ into γ-cyclodextrin

2.7.1. Inclusion Study

As Mn(III)TPP-*p*-CF₃ is nonpolar, it is only soluble in organic solvents. Considering that its application includes conducting *in vitro* studies in aqueous solutions, it was

necessary to overcome this obstacle. The inclusion of Mn(III)TPP-*p*-CF₃ into cyclodextrins has the purpose of increasing its solubility in water.

Therefore, a solution of Mn(III)TPP-*p*-CF₃ (1.3 mg, 1.3 × 10⁻³ mmol) in THF (25 mL) was prepared, to a final concentration of 5.2 × 10⁻⁵ M. The buffer HEPES (pH 7.4) was used in the same concentration as mentioned above. In this study, two different cyclodextrins were tested: methyl-β-cyclodextrin and γ-cyclodextrin. The solutions were prepared so that each reached a final concentration of 7 × 10⁻⁴ M in water.

After that, five Mn(III)TPP-*p*-CF₃ solutions with different concentrations of cyclodextrin were prepared. Each solution contained 1 mL of Mn(III)TPP-*p*-CF₃ and 1 mL of HEPES. The volumes of aqueous cyclodextrin added to the above mixture were those necessary to obtain the following final concentrations: 1 × 10⁻⁴ M (1.43 mL), 2 × 10⁻⁴ M (2.86 mL), 3 × 10⁻⁴ M (4.30 mL), 4 × 10⁻⁴ M (5.71 mL) and 5 × 10⁻⁴ M (7.14 mL). In the end, sufficient water was added to bring the total volume of the solutions to 10 mL. The final concentration of Mn(III)TPP-*p*-CF₃ in those solutions was 5.2 × 10⁻⁶ M. This procedure was repeated for both cyclodextrins used in this experiment. The absorbance of the solutions was monitored by UV-Vis spectroscopy to analyse if there were any changes in the structure of the porphyrin of interest, supported by the appearance/disappearance of the characteristic bands.

2.7.2. Reduction of γ-CD*Mn(III)TPP-*p*-CF₃

Analogously to what was done in section 2.6.2., it was intended to confirm if the Mn(III)TPP-*p*-CF₃ porphyrin would still be reduced in the presence of ascorbic acid, also considering the presence of γ-cyclodextrin in solution. Thus, five solutions containing the γ-CD*Mn(III)TPP-*p*-CF₃ complex were prepared as described in section 2.7.1. The solution of ascorbic acid was used as mentioned above. The reduction was monitored by UV-Vis spectroscopy by adding several volumes of the reducing agent to the multiple solutions under analysis.

2.7.3. ¹H and ¹⁹F NMR Study

NMR spectroscopy has also been applied for confirming the binding mode, coordinative sites and binding mechanism between porphyrins and cyclodextrins [94,132]. The nature of the interaction between Mn(III)TPP-*p*-CF₃ and γ-CD was probed using both ¹H and ¹⁹F NMR spectroscopy.

Firstly, a solution of γ-CD in D₂O (5 × 10⁻⁴ M) was characterized by ¹H NMR. Then, stock solutions of Mn(III)TPP-*p*-CF₃ in DMSO-*d*₆ (5 × 10⁻⁴ M and 8.5 × 10⁻⁴ M) and γ-CD in

D₂O (5 x 10⁻⁴ M and 8.5 x 10⁻⁴ M) were used to perform titrations aiming to analyse the interaction and further establish the stoichiometry between these compounds. For one set of experiments, increasing volumes of Mn(III)TPP-*p*-CF₃ (8.5 x 10⁻⁴ M) were added to the cyclodextrin solution (5 x 10⁻⁴ M) placed in the NMR tube. For the other set, increasing volumes of γ -CD (8.5 x 10⁻⁴ M) were added to the Mn(III)TPP-*p*-CF₃ solution (5 x 10⁻⁴ M). After each addition, the mixture was stirred in order to homogenise it before the spectrum acquisition. All the NMR spectra were taken at room temperature.

2.7.4. Stoichiometric Determination

Stoichiometric determination of reactants is a crucial step not only to characterize products but also to assess their interaction when searching for new compounds.

Hence, a titration of Mn(III)TPP-*p*-CF₃ with γ -CD was performed. Three stock solutions were required to carry out this study: Mn(III)TPP-*p*-CF₃ in THF (5.2 x 10⁻⁵ M); γ -CD in water (7 x 10⁻⁴ M) and HEPES buffer (0.1 M, pH 7.4). All the solutions were prepared according to section 2.6.2. and section 2.7.1. Thereafter, 9 solutions were prepared, keeping the number of moles of Mn(III)TPP-*p*-CF₃ constant - 1 x 10⁻⁴ mmol. Several molar fractions of γ -CD (0.1; 0.2; 0.3; 0.4; 0.5; 0.6; 0.7; 0.8 and 0.9) were added to each one of the volumetric flasks and the remaining volume was made up with HEPES so that the final volume for each solution was 10 mL.

Another experiment that was carried out to establish the stoichiometry between these two species was the Job's method (also known as the method of continuous variations), which is applied for the identification of compounds formed in solution by reaction of two species [133]. The formation of complexes can be represented by the following equation 2.1:



Here, A represents a metal ion, and B refers to a molecule capable of interacting with A, for example, an anion, forming a complex A_mB_n with a n/m stoichiometry. To determine m and n, stock solutions of A and B of the same molar concentration are combined in varying proportions, so that their total molar concentration is kept constant, and a convenient property of the resulting solutions is measured [134]. The units on the x-axis vary from concentration to mole fraction of A or B (X_A or X_B), taking into consideration equation 2.2:

$$X_A = \frac{[\text{A}]}{\{[\text{A}]+[\text{B}]\}} = 1 - X_B \quad (2.2)$$

The application of mole fraction or its equivalent along the x axis is common in all Job plots [135]. The most used dependent variable for the y axis is UV-Vis absorbance, but any other property able to correlate linearly with the concentration of A_mB_n is suitable, for instance, kinetics, conductivity, NMR signal intensity, permittivity, calorimetry, gravimetric titration, etc. The shape of the curve provides qualitative insight into the equilibrium constant (K_{eq}) of the complex. While a strong binding produces a more angular plot (similar to a triangle-shaped plot in the limit), a more balanced equilibrium leads to a softer curvature [136,137]. Thus, considering the shape of the plot along with the maximum or minimum value obtained, it is possible to establish the stoichiometry of the two species in the complex.

Briefly, two solutions were used – Mn(III)TPP-*p*-CF₃ in HEPES (1 x 10⁻⁵ M) and γ-CD in HEPES (1 x 10⁻⁵ M), which were tested at different molar concentration ratios ranging from 0:1 to 1:0 (Mn(III)TPP-*p*-CF₃:γ-CD) as demonstrated in Table 2.4. Afterwards, absorption spectra were immediately measured.

Table 2.4. Schematic representation of Job's Method experiment.

Molar fraction of Mn(III)TPP-<i>p</i>-CF₃	0	0.1	0.2	0.3	0.4	0.5	0.6	0.7	0.8	0.9	1
Molar fraction of γ-CD	1	0.9	0.8	0.7	0.6	0.5	0.4	0.3	0.2	0.1	0
Final solution	Mixture with a final volume of 10 mL										

2.8. Cell Initiation

A new cell culture was prepared from a 1 mL aliquot of cryopreserved Caco-2 cells, according to the procedure schematically represented in Figure 2.3. The frozen cells were placed in a water bath to defrost (at 37 °C). This solution was then transferred to a centrifuge tube containing 10 mL of MEM culture medium and it was centrifuged at 1100 rpm for 5 minutes in order to remove dead cells and DMSO (a constituent of the freezing medium). The supernatant was discharged, and the pellet was resuspended in 10 mL of culture medium. Finally, the cells were transferred to a 75 cm² culture flask and were incubated at 37 °C in a humidified atmosphere containing 5% CO₂ until the culture was ready for subculturing.

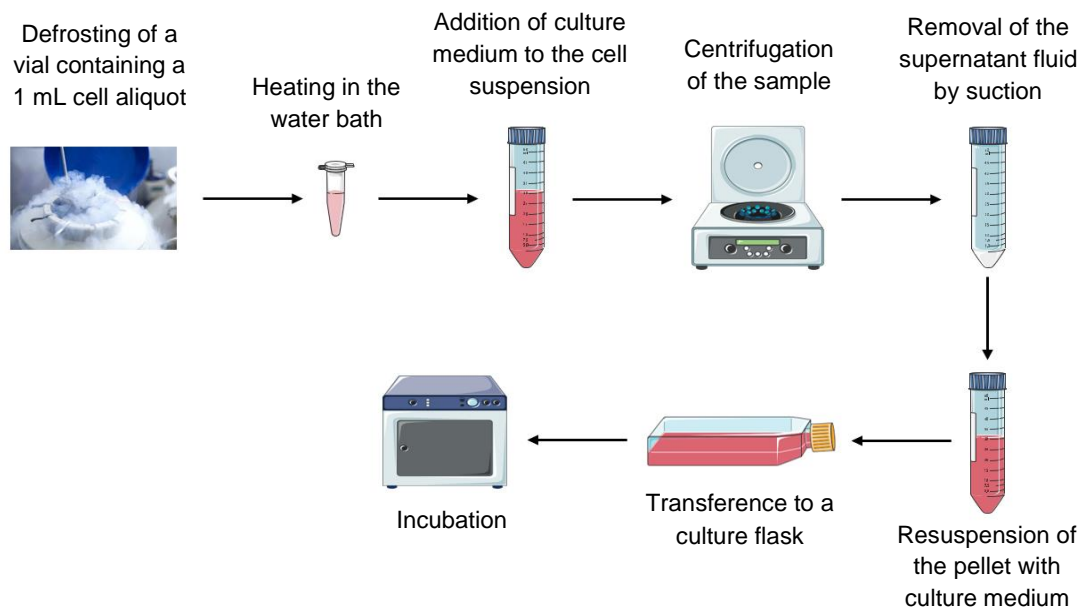


Figure 2.3. Schematic representation of the main steps required for cell initiation.

2.9. Cell Culture Procedure

The Caco-2 cells, which grow as adherent monolayers, were cultured in 75 cm² filter vented flasks (except when otherwise stated), under sterile conditions, at 37°C in a humidified atmosphere containing 5% CO₂. The cultures were maintained in MEM culture medium, supplemented with glucose, thirteen essential amino acids and eight different vitamins (thiamine, riboflavin, nicotinamide, pantothenic acid, pyridoxine, folic acid, choline and myo-inositol).

Cells were seeded with a dilution factor of 1:3, and cultures were subcultured once or twice a week, when reaching 80% confluence (before the stationary growth phase, Figure 2.4).

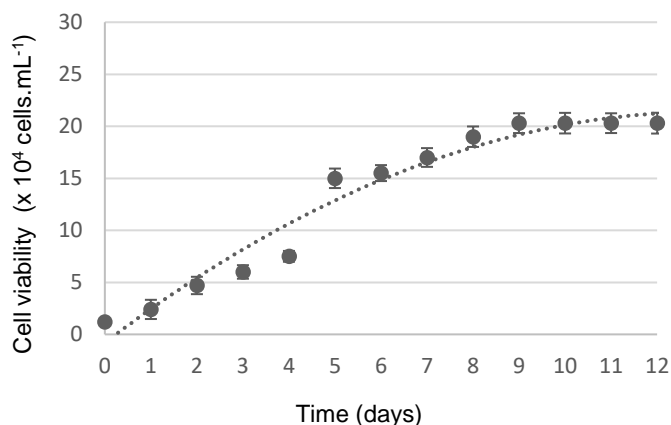


Figure 2.4. Growth curve of Caco-2 cells. The cell viability was determined by the SRB method. The number of cells gradually increases with time before reaching the stationary growth phase [138].

The subculturing process is represented in Figure 2.5. Firstly, the culture medium was discarded and the cell monolayer was washed with 5 mL of PBS 1x. Then, 2 mL of trypsin-EDTA solution were added and spread over the monolayer. The trypsinisation process was monitored over time (approximately 20 minutes) using an inverted optical microscope, especially the moment when cells were detached from the bottom of the flask (cells became smaller, rounded-shaped and brighter). At this stage, MEM medium was added to inhibit the trypsin. Finally, 2 mL of the cell suspension were transferred to a new 75 cm² flask and fresh cell culture medium was added.

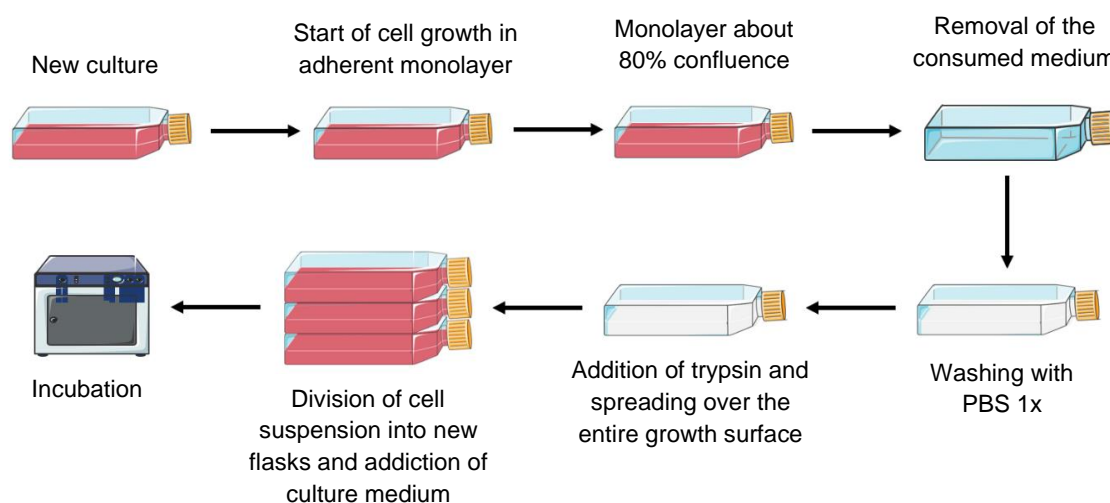


Figure 2.5. Schematic representation of the fundamental steps required for cell subculturing.

2.10. Trypan Blue Exclusion Method

The Trypan Blue (TB) dye exclusion test was used as a method for cell counting. This is a simple and rapid assay to determine the number of morphologically intact cells in a cell suspension. This method takes advantage of the fact that living cells have an intact cell membrane and, consequently, the TB dye is not able to cross the membrane and enter the cell. On the other hand, dead cells have a disrupted membrane allowing this dye to cross into the cell. As a result, dead cells display a dark (blue) cytoplasm, allowing easy identification by observation under the microscope. Nevertheless, this method has the disadvantage of not being able to differentiate between viable and non-viable cells, since a cell may be unviable even if it still displays an intact membrane [139,140].

Sample preparation for cell counting followed the previously described process, until the trypsinization step (section 2.9). At this stage, 8 mL of MEM culture medium were added to the cell suspension which was centrifuged at 1100 rpm for 5 minutes. The supernatant was discarded and the pellet was resuspended in 10 mL of fresh culture

medium. In a separate Eppendorf, 0.5 mL of this suspension was added to 0.5 mL of MEM. Samples for cell counting were prepared by mixing small volumes of this cellular suspension and 0.4% (w/v) solution of TB, in appropriate proportions - usually 20 μL TB/20 μL cell suspension. After homogenisation, this solution was used to fill the two chambers of a hemocytometer. Upon examination under an inverted optical microscope, the cells were counted and averaged (Figure 2.6).

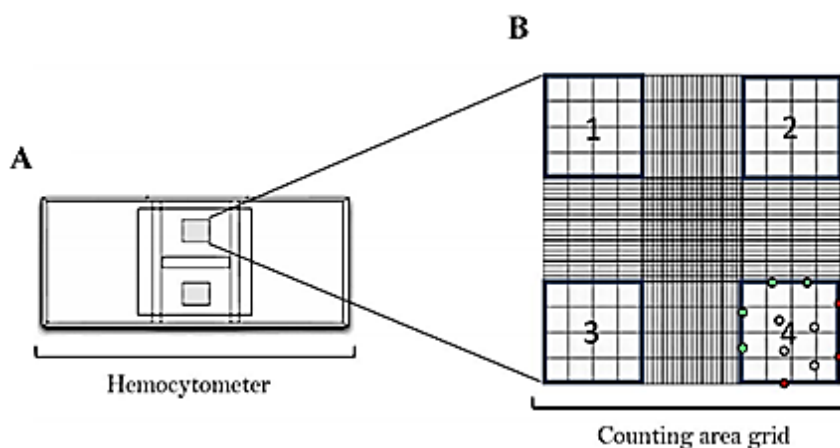


Figure 2.6. Schematic representation of a hemocytometer (A) and its counting areas (B). Before cell counting, a coverslip was placed over the hemocytometer and the cellular suspension with TB was added to both counting areas. Only the cells represented in the numbered squares were counted, according to the rule depicted in square number 4: the green and empty circles indicate the counted cells (inside the grid and overlapping with the top and left edges), while the red circles indicate the cells excluded from the counting.

For each cellular suspension, at least two countings were carried out. Taking into account the volume of each corner square (1×10^{-4} mL) and the dilution factor, the total number of cells *per* mL of cellular suspension was determined using equation 2.3, where x represents the mean number of cells counted in the four hemocytometer squares for each counting (eight in total):

$$\text{cells/mL} = x \times \frac{\text{dilution factor}}{1 \times 10^{-4} \text{ mL}} \quad (2.3)$$

2.11. Morphological Studies

The cell morphology and growth pattern of the Caco-2 cells were monitored by phase-contrast optical microscopy, with an Olympus CKX41 microscope using a 10x objective with phase-contrast.

The Caco-2 population, when in culture, undergoes a process of spontaneous differentiation which leads to the emergence of a cellular monolayer expressing several morphological and functional characteristics of the mature human enterocyte [141]. Moreover, the culture conditions influence the expression of these features, contributing to

a selection of sub-populations of cells that do not express all the characteristics of the parental line and may become dominant in the culture [111]. Consequently, the Caco-2 population is characterized by the presence of sub-populations with different morphologies, as shown in Figure 2.7.

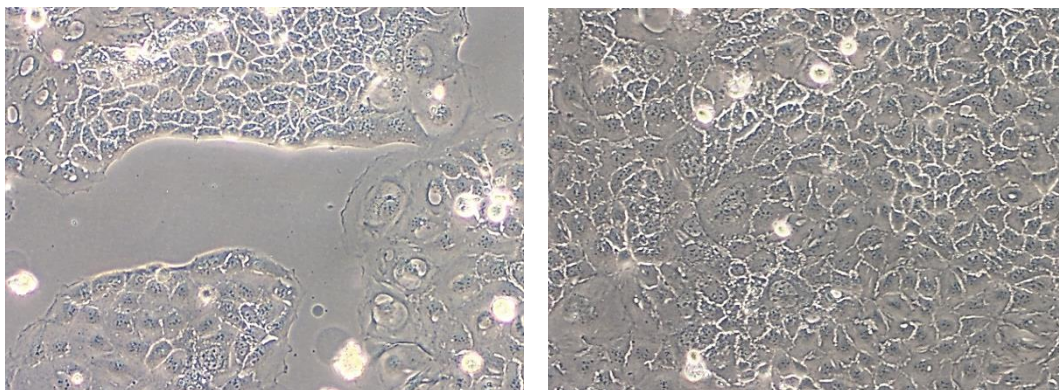


Figure 2.7. Caco-2 cell line at passage #57 observed under an inverted optical microscope. The left panel shows cells seeded at low density. The right panel shows cells exhibiting a high density, where the formation of the monolayer is prominent.

2.12. *In Vitro* Antitumour Assays

Two different *in vitro* assays were carried out to assess the antiproliferative and cytotoxic activities of both Mn(III)TPP-*p*-CF₃ and γ -CD*Mn(III)TPP-*p*-CF₃ agents as biocompatible probes. The Sulforhodamine B colorimetric assay evaluates the number of living cells (cell density, directly related to anti-proliferative ability), whereas the MTT assay determines cell viability (cytotoxic potential) through the reduction of 3-(4,5-dimethylthiazol-2-yl)-2,5-diphenyltetrazolium bromide. The antitumour capacity of both compounds was assessed for the established concentrations and incubation times, against the Caco-2 human colorectal adenocarcinoma cell line.

For both SRB and MTT assays, the cells were seeded at 3×10^4 cells/cm² in 24-well cell culture plates (with a growing area of 1.93 cm²) by adding 1 mL of cell suspension (containing approximately 5.79×10^4 cells/mL) to each well. The cells were treated with different concentrations of the tested agents and monitored over time – after 24, 48 and 72 hours. Furthermore, a reversibility study was carried out after 72 hours of exposure to the tested agents, by removing the medium containing the tested agents and substituting it by new culture medium, after which the cells were left to incubate for 72 h and then counted (after a total of 144 h).

These assays were performed in triplicate, in three independent experiments. The results were compared with control cultures – cells not exposed to the tested agents, which were started and processed in parallel.

2.12.1. SRB Assay

Cell density was determined using the sulforhodamine B colorimetric assay, based on the measurement of the cellular protein content. The SRB assay is a rapid and sensitive colorimetric method for measuring the drug-induced growth-inhibiting activity in both monolayer and suspension cell cultures. This assay was developed for use in the disease-orientated large-scale anticancer drug discovery program of the National Cancer Institute (NCI) [142].

SRB is a bright pink aminoxanthene dye, comprising two sulfonic groups (Figure 2.8). Under mildly acidic conditions, it binds to the basic amino acid residues from proteins present in the cell membrane, to provide a sensitive index of cellular protein. Since the binding of SRB is stoichiometric, the amount of the dye extracted from the coloured cells is directly proportional to the cell mass (and thus equivalent to cell density) [143]. This is a simple, fast, and sensitive method, able to detect very small cell densities with good accuracy and without significant interference from environmental fluctuations. Moreover, this assay allows to test a large number of samples in a short time, using non-expensive reagents and equipment, thus being an economically viable large scale *in vitro* screening test [144].

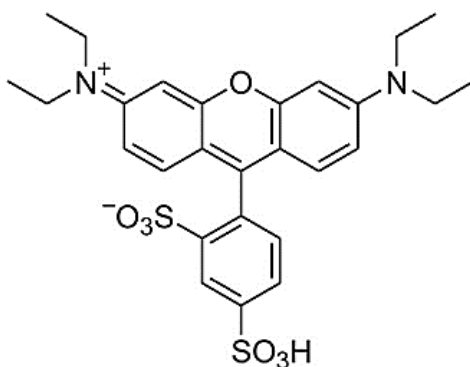


Figure 2.8. Chemical structure of Sulforhodamine B. (From [145]).

After cell culture establishment in the 24-well cell culture plates, the cells were treated with different concentrations of Mn(III)TPP-*p*-CF₃ (5 μM, 2.50 μM, 1.25 μM, 0.63 μM, 0.32 μM, and 0.16 μM) and γ-CD*Mn(III)TPP-*p*-CF₃ (500 μM, 250 μM, 125 μM, 62.50 μM, 31.25 μM, and 15.63 μM), to a final volume of 800 μL in each well and were then

monitored at defined timepoints (Figure 2.9). The cells in control wells were incubated with DMSO: 8 μL of DMSO (corresponding to 1% (v/v)) for Mn(III)TPP-*p*-CF₃ and 80 μL of DMSO:H₂O (10% (v/v) DMSO:H₂O) for γ-CD*Mn(III)TPP-*p*-CF₃, considering the total volume of each well (since a higher concentration leads to a cytotoxic effect of DMSO on the cells). The cell density was quantified at 24, 48 and 72 hours after the addition of the tested agents. Upon these incubation periods, the cells were washed with PBS 1x and ultrapure water and were incubated at 37°C for 2 h. Then, 1 mL of cold methanol 1% (v/v)/acetic acid solution was added, and the culture plates were stored at -20°C. Afterwards, the solution was discarded and 250 μL of 0.5% (w/v) SRB solution were added. After incubation at 37°C for 1 hour (wrapped in aluminium foil, since this solution is photosensitive), the excess of dye that was not bound to the cellular proteins was removed by washing with a 1% (v/v) acetic acid solution. The culture plates were left to dry overnight. Finally, 1 mL of Tris was added to obtain a more homogenous colour and allow an accurate absorbance reading. This was carried out in a Biotek Gen5™ scanning multiwell spectrophotometer, at 540 nm.

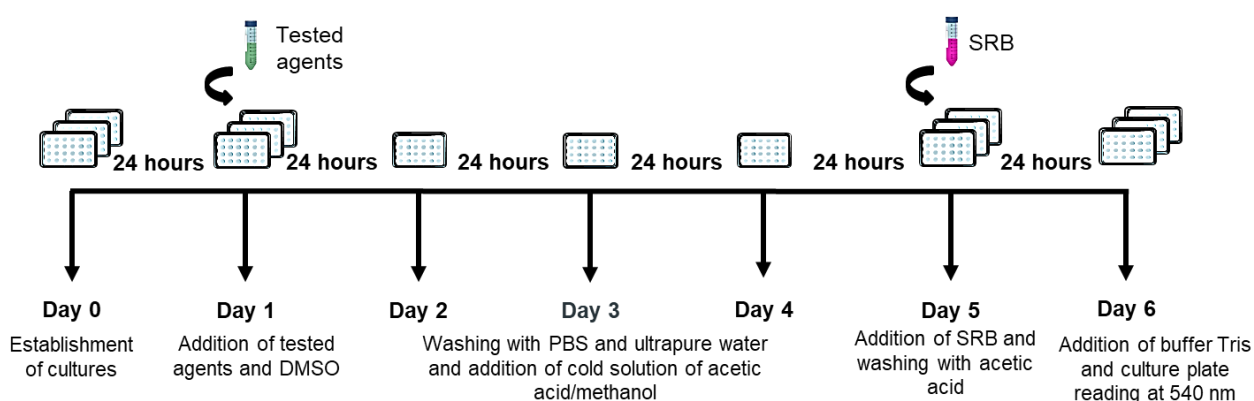


Figure 2.9. Protocol used for the analysis of cell protein content based on the SRB assay.

The values of cell proliferation were estimated by the percentage of SRB retention (cell density), according to equation 2.4:

$$\% \text{ cellular proliferation} = \frac{A_{\text{sample}} - A_{\text{control}_0}}{A_{\text{control}} - A_{\text{control}_0}} \times 100 \quad (2.4)$$

Where A_{sample} represents the absorbance of the solutions exposed to the tested agents, A_{control_0} is related to the absorbance of the control ($t = 0$ hours, which corresponds to cell density in the absence of any compounds) and A_{control} expresses the absorbance of the control wells at the different time points counted.

2.12.2. MTT Assay

The MTT colorimetric assay for spectrophotometric quantification of cell viability relies on the cleavage of the yellow MTT tetrazolium salt to yield purple formazan crystals (Figure 2.10), in metabolically active cells. The reduction of MTT to formazan is catalysed by mitochondrial succinate dehydrogenase (SDH), which involves the pyridine nucleotide cofactors NADH or NADPH. Since SDH is an important cellular enzymatic complex, that participates in both the tricarboxylic acid cycle and the electron transport chain, the MTT assay is dependent on mitochondrial respiration and is therefore directly related to cell viability [146,147].

The formazan crystals, which are insoluble in water, are solubilised in DMSO giving rise to a coloured solution (violet) that can be quantified by spectrophotometry, measuring the absorbance values at 570 nm. Following the Beer-Lambert law, it is possible to quantify the formazan formed upon addition of MTT to the cell suspension, since at this wavelength the unmetabolized MTT has no absorbance (it is colourless). This assay allows rapid and convenient handling of a large number of samples and ensures a high degree of accuracy [148].

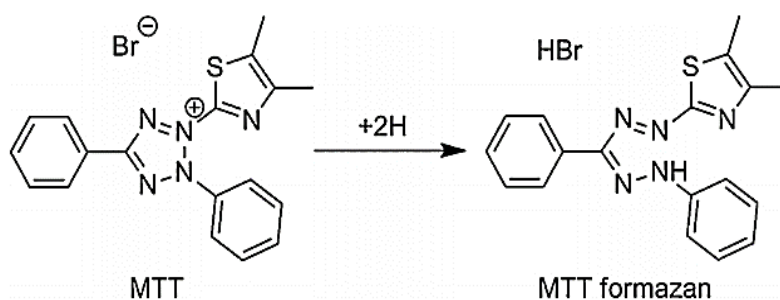


Figure 2.10. Reduction of MTT bromide to its formazan crystals by cellular reductases, in viable cells. (From [146]).

Analogously to the SRB method, after the establishment in the 24-well cell culture plates, the cells were treated with the same concentrations of Mn(III)TPP-*p*-CF₃ (5 μM , 2.50 μM , 1.25 μM , 0.63 μM , 0.31 μM , and 0.16 μM) and γ -CD*Mn(III)TPP-*p*-CF₃ (500 μM , 250 μM , 125 μM , 62.50 μM , 31.25 μM , and 15.63 μM) to a final volume of 1 mL in each well and were monitored at defined timepoints (Figure 2.11). The control wells were incubated with DMSO: 10 μL of DMSO (1% (*v/v*)) for Mn(III)TPP-*p*-CF₃; and 100 μL of DMSO:H₂O (10% (*v/v*) DMSO:H₂O) for γ -CD*Mn(III)TPP-*p*-CF₃, considering the total volume of each. The cell viability was measured at 24, 48 and 72 hours after the addition of the tested agents. Upon these incubation periods, the cells were washed with PBS 1x, treated with

250 µL of a 0.5 mg/mL MTT solution and incubated at 37°C for 2 h (wrapped in aluminium foil). After incubation, the solution was removed with care (not to destroy the formazan crystals) and 250 µL of DMSO were added to each well to completely dissolve the crystals, resulting in a homogenous violet solution. Finally, the samples were measured (in the culture plate) as to their absorbance at 570 nm, in a Biotek Gen5™ scanning multiwell spectrophotometer.

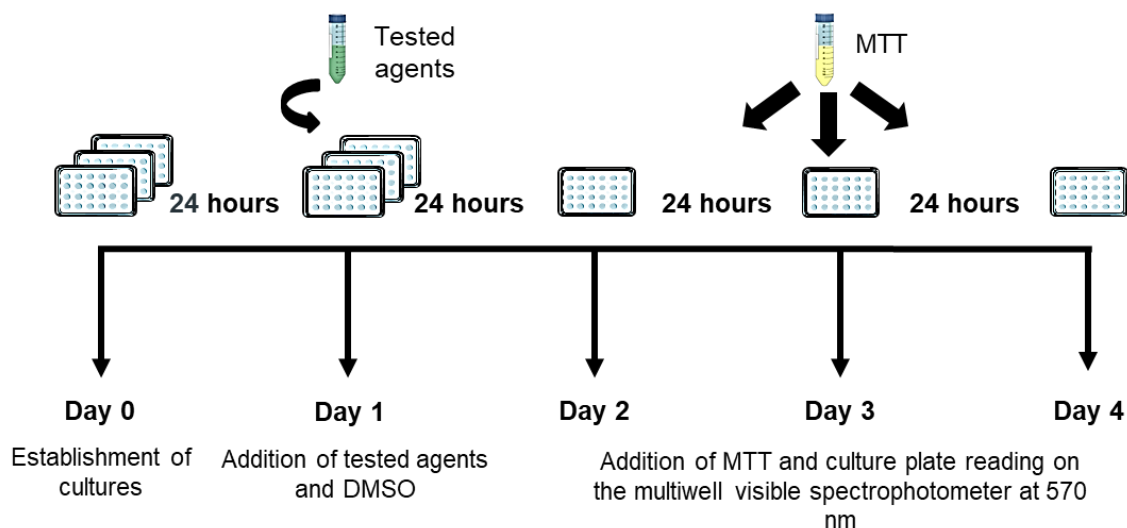


Figure 2.11. Protocol used for the analysis of cell viability based on the MTT metabolization.

The values of cell viability were determined according to equation 2.5:

$$\% \text{ cell viability} = \frac{A_{\text{sample}}}{A_{\text{control}} - A_{\text{blank}}} \times 100 \quad (2.5)$$

Where A_{sample} represents the absorbance of the solutions exposed to the tested agents, and A_{blank} and A_{control} are the absorbance of DMSO and corresponds to the absorbance of the control wells. The results were expressed as a percentage in relation to the control, which was considered 100%.

2.13. Data Processing and Analysis

The chemical structures and reactions were made using ChemDraw Ultra 12.0 Software for Windows (ChemDraw, PerkinElmer, France).

The UV-Vis spectra were plotted using Origin Software for Windows (OriginLab Corporation, Massachusetts, USA). All the data were collected using specific software coupled to the UV-Vis spectrophotometer. The molar absorption coefficients were obtained

using the linear fit and regression analysing tools. All the spectra were normalized to obtain a graphical representation for absorbance values not exceeding 1.

The NMR spectra were analysed using MestreNova Software (Mestrelab Research S. L., Santiago de Compostela, Spain). All the data were processed using phase line and baseline correction. The chemical shift and area values shown result from peak picking and their integration.

Cell proliferation data were obtained from experiments in which both controls and cell cultures were established and processed in parallel. The results were expressed as a percentage of the control and were an average of at least three independent experiments. The statistical analysis of these *in vitro* results was performed with the GraphPad Prism 8.0.2 software for Windows (GraphPad Software Inc, California, USA). The statistical relevance of differences between concentrations was examined using the one-way ANOVA method, which was followed by Tukey's multiple comparison test. The results were presented as mean \pm standard deviation (S.D.). Differences with $p^* < 0.05$; $p^{**} < 0.01$; $p^{***} < 0.001$; $p^\# < 0.0001$ were considered statistically significant.

Synthesis and Characterization of a Biocompatible Fluorinated Mn(III)-Porphyrin as a Redox Responsive ¹⁹F-NMR/T₁ Bimodal MRI Contrast Agent

Results and Discussion

Synthesis and Characterization of a Biocompatible Fluorinated Mn(III)-Porphyrin as a Redox Responsive ¹⁹F-NMR/T₁ Bimodal MRI Contrast Agent

3.1. Synthesis of the Mn(III)TPP-*p*-CF₃ Probe

As previously discussed in Chapter 1, the growing application of porphyrins in medicine plays a crucial role in its development, particularly in structural modulation and improvement of its synthesis methods. One of the most well-known methods for synthesizing meso-aryl porphyrins is the nitrobenzene method, which was used in the synthesis of the porphyrin described in this dissertation. Thus, the main goal of this work was the development not only of the free-base porphyrin but also its manganese-complexed form for potential application in ^{19}F MRI as a fluorinated contrast agent.

Firstly, TPP-*p*-CF₃ was synthesized through the nitrobenzene method by heating a mixture of glacial acetic acid and nitrobenzene at 120°C, for ten minutes. Then, 4-(trifluoromethyl)benzaldehyde and 1H-pyrrole were added dropwise (Figure 3.1). The reaction was left in a reflux system with stirring for two hours. After complete reaction, the mixture was cooled, and precipitation was done with methanol. In the end, the TPP-*p*-CF₃ was collected being the total yield of 10%.

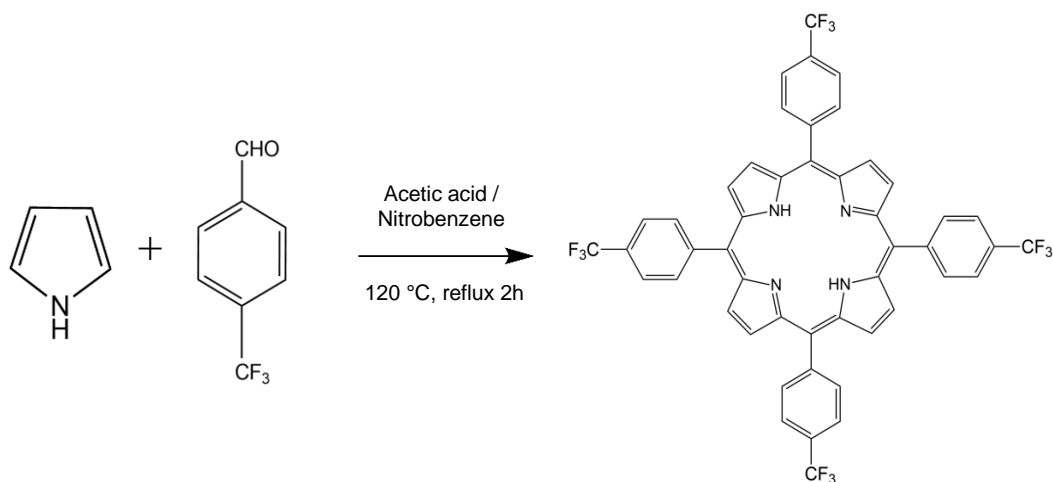


Figure 3.1. Synthesis of TPP-*p*-CF₃. Reagents and reaction conditions: Acetic acid/Nitrobenzene, 2 hours, 120°C.

The preparation of Mn(III)TPP-*p*-CF₃ proceeded by reacting the TPP-*p*-CF₃ porphyrin with excess manganese (II) acetate and sodium acetate. Acetic acid was used as a solvent and the temperature was kept constant at 80°C. The control of the reaction was done by UV-Vis spectroscopy. After purification, a yield of 85% was obtained. The strategy adopted for the synthesis of the Mn^{III} biocompatible probe is depicted in Figure 3.2.

Synthesis and Characterization of a Biocompatible Fluorinated Mn(III)-Porphyrin as a Redox Responsive ^{19}F -NMR/ T_1 Bimodal MRI Contrast Agent

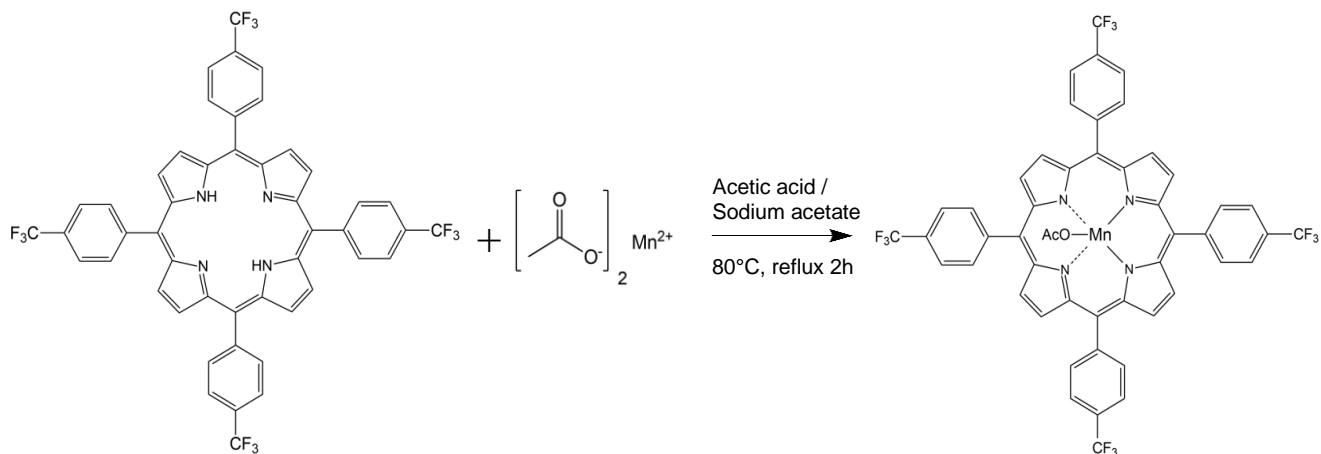


Figure 3.2. Synthesis of Mn(III)TPP-*p*-CF₃. Reagents and reaction conditions: Acetic acid/Sodium acetate, 2 hours, 80°C.

In order to characterize the complex, ^1H NMR spectroscopy was carried out in deuterated DMSO, before and after the complexation with manganese. Figure 3.3 represents the ^1H NMR spectrum of TPP-*p*-CF₃ and Figure 3.4 represents the ^1H NMR spectrum of Mn(III)TPP-*p*-CF₃.

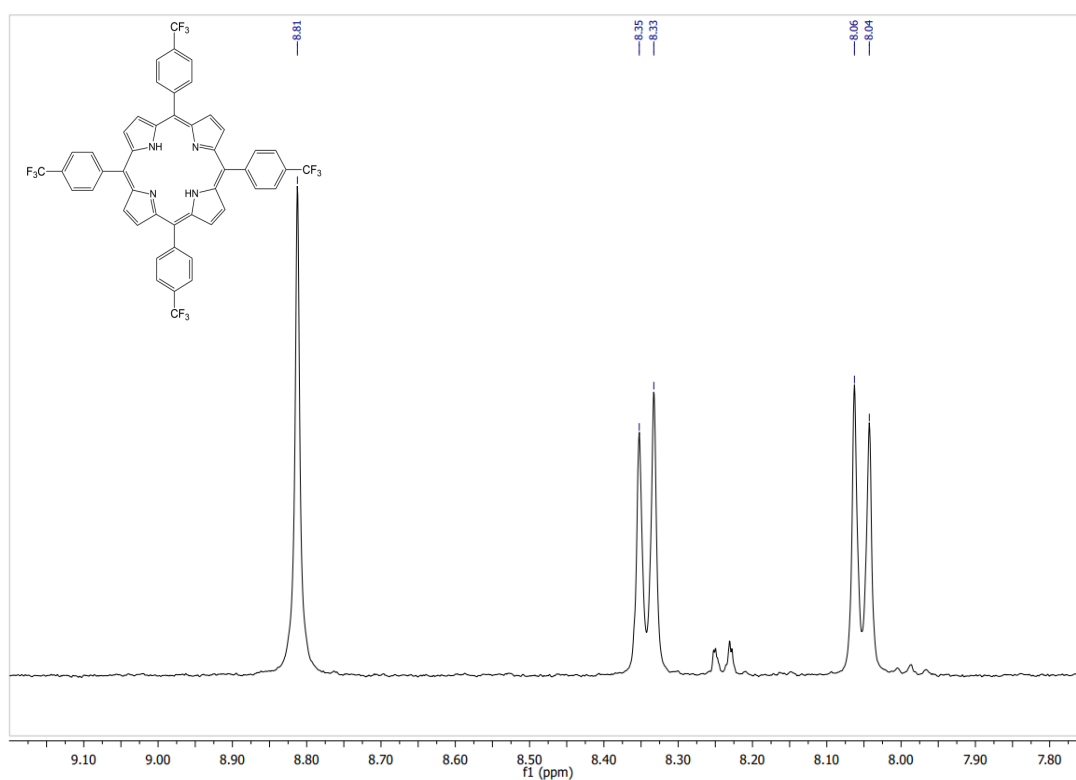


Figure 3.3. ^1H NMR spectrum of 0.6 mM TPP-*p*-CF₃ recorded in DMSO-*d*₆, at room temperature (25°C).

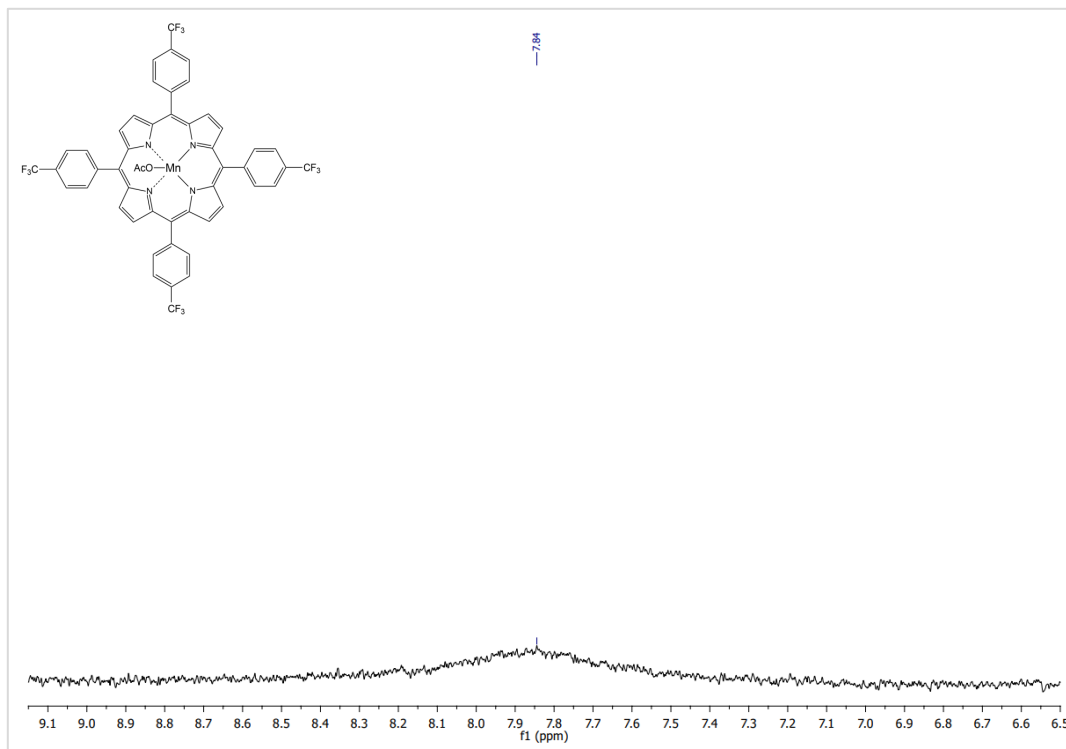


Figure 3.4. ^1H NMR spectrum of 0.6 mM Mn(III)TPP-*p*-CF₃ in DMSO-*d*₆, at room temperature (25°C).

Analysing the TPP-*p*-CF₃ spectrum, the presence of several protons with different chemical shifts can be noticed. A singlet at $\delta = 8.82$ ppm is observed, corresponding to the resonance of the β -pyrrolic protons, as these protons are very unprotected due to the strong ring current shifts caused by π electrons. The doublet at $\delta = 8.34$ ppm ($^3J_{\text{HH}} = 7.9$ Hz) corresponds to the ortho protons of the meso aryl group that are closer to the macrocycle. On the other hand, the doublet at $\delta = 8.05$ ppm ($^3J_{\text{HH}} = 8.0$ Hz) is assigned to the meta protons of the aryl group located near the CF₃ group. Comparing these results with the spectrum obtained after manganese complexation (Figure 3.4), the effect of the metal is notorious. The oxidation of Mn^{II} to Mn^{III} in Mn(III)TPP-*p*-CF₃ causes a strong broadening of the aryl proton signals indicated above, and it is only possible to observe a very wide peak centred at $\delta \cong 7.85$ ppm, shifted to higher frequencies relative to the diamagnetic positions. The β -pyrrolic protons, which would be expected around -22 ppm [63], are too broad to be observed. Therefore, Mn³⁺ causes, as expected, strong proton shifts and broadenings, but the signals are still observable [63].

Considering that the application of this complex is intended for ^{19}F MRI, its analysis by ^{19}F NMR is also fundamental. According to previous results [149], the ^{19}F NMR spectrum of TPP-*p*-CF₃ consists of a well-defined sharp peak ($\Delta\nu_{1/2} = 2.93$ Hz) singlet at $\delta = -62.07$

ppm, corresponding to the twelve equivalent fluorine atoms of the molecule, with the same chemical shift. The ^{19}F NMR spectrum of Mn(III)TPP-*p*-CF₃ is illustrated in Figure 3.5, which shows the presence of a sharp (linewidth $\Delta\nu_{1/2} = 44.87$ Hz) singlet of high intensity ($\delta = -61.12$ ppm), corresponding to the same twelve equivalent fluorine atoms in the four CF₃ groups. The paramagnetic Mn^{III} ion of Mn(III)TPP-*p*-CF₃ induced a very small positive paramagnetic shift (+0.95 ppm) on the CF₃ signal broadening ($\Delta\Delta\nu_{1/2} = 41.94$ Hz), thus confirming the potential use of this complex as a ^{19}F MRI contrast agent.

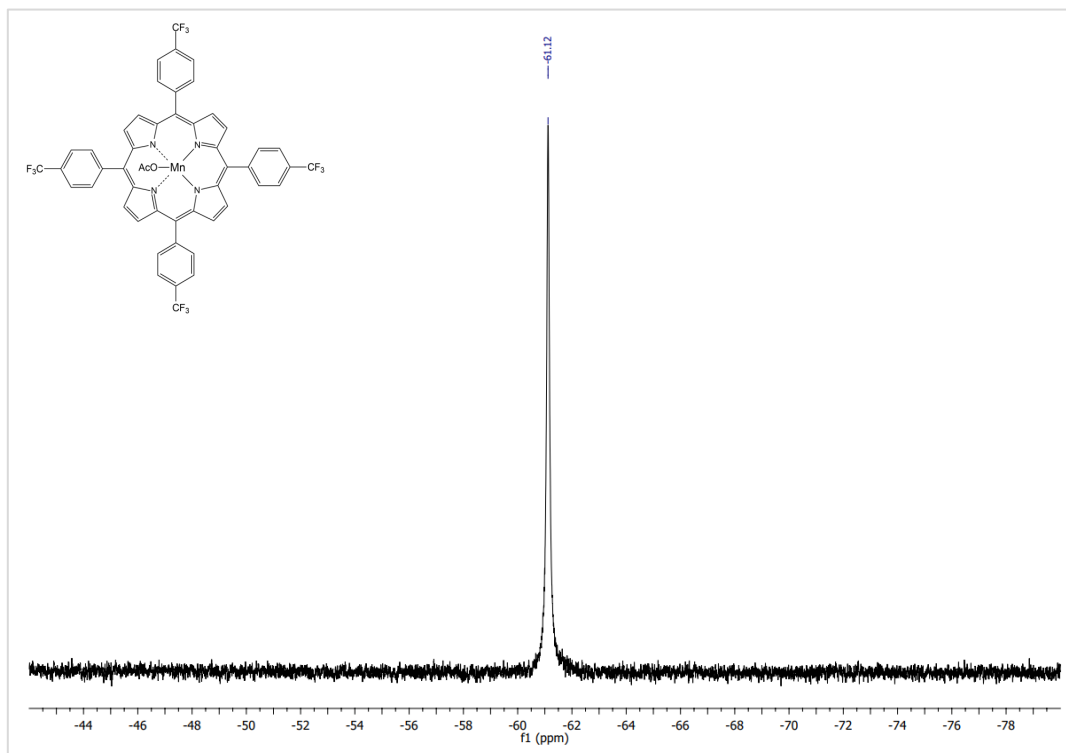


Figure 3.5. ^{19}F NMR spectrum of 0.6 mM Mn(III)TPP-*p*-CF₃. The spectrum was recorded in deuterated DMSO, at room temperature (25°C).

In fact, signal intensity is maximized if there is only one dominant ^{19}F resonance to observe. This suggests that the preferred ^{19}F labels are homotopic CF₃ groups, in a preferentially water-soluble complex where one major stereoisomer that is kinetically stable is present in solution [150,151]. This situation observed with Mn(III)TPP-*p*-CF₃, is, in contrast, with the multiple ^{19}F signals observed for the Mn(III) complex of tetra-phenyl porphyrin with the phenyl rings fluorinated at the ortho and meta positions, and with PEG₅₀₀ groups in the para positions, Mn(III)-TTFPP-(pPEG₅₀₀) porphyrin [63]. Its ^{19}F NMR spectrum consists of a broad resonance at -126.2 ppm ($\Delta\nu_{1/2} \cong 2260$ Hz), corresponding to the eight ortho ^{19}F nuclei and a set of five sharper ($\Delta\nu_{1/2} \cong 190$ Hz) signals from the meta ^{19}F nuclei (due to the five possible combinations of the chain lengths of the four polydisperse PEG chains with

several ethylene glycol moieties $n = 10-11$). Their ^{19}F paramagnetic shifts induced by Mn^{3+} relative to the free porphyrin are +10.7 ppm (ortho) and in the +7.3 to 0.7 ppm range (meta). The relative values of the paramagnetic ^{19}F shifts and broadenings observed for the ortho and meta nuclei in $\text{Mn(III)-TTFPP-(pPEG}_{500})$ are in qualitative agreement with the $1/r^3$ and $1/r^6$ (being r is the average Mn-F distance) dependence of the dipolar shift and relaxation effects expected for Mn^{III} [63].

3.2. Characterization of the Mn(III)TPP- $p\text{-CF}_3$ Probe

3.2.1. Determination of Molar Absorption Coefficients

To achieve a more detailed characterization of the synthesized manganese complex, several photophysical parameters were determined.

Porphyrins have a characteristic UV-Vis absorption spectrum because of their ability to absorb radiation in the UV-Vis region and due to the fact that they have a delocalised π electron system [152]. So, the UV-Vis absorption spectrum of a free-base porphyrin is characterized by the existence of an intense absorption band between 350 to 500 nm, called B band or Soret band, followed by four bands with lower intensity, known as Q bands, observed from 500 to 750 nm [153].

The metalloporphyrins have a metal atom complexed at the centre of the molecule, while free base porphyrins have two hydrogen atoms in the centre [154]. The insertion of a metal ion into the porphyrin cavity or the protonation of the nitrogen atoms may result in a change in the wavelength and intensity of the absorption spectrum (Figure 3.6). When the metal ion coordinates with the N atoms, the number of Q bands tends to decrease. Hence, metalloporphyrins exhibit one Soret band and either one or two Q bands [155].

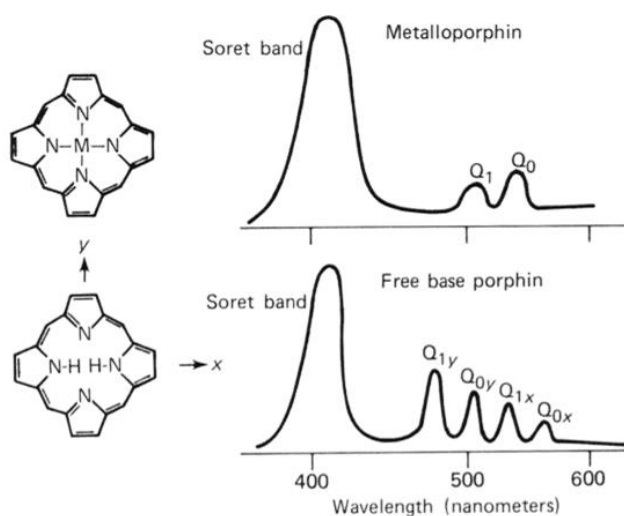


Figure 3.6. Optical absorption spectra of free-base porphyrin and metalloporphyrin in solution, at room temperature. In the metalloporphyrin, Q_0 is the result of a pure electronic transition (no

molecular vibrations) between the electronic ground state and the first electronic excited state; Q₁ is due to the same electronic transition but also molecular vibrations are involved. This band is called a vibronic band. The 0 and 1 of free-base porphyrin indicate a similar interpretation. The x and y refer to the orientation (polarization) of the electric vector of the absorbed light concerning the axes shown on the chemical structure diagram for free-base porphyrin. (From [156]).

The Beer-Lambert law connects the attenuation of light with the characteristics of the material through which light is travelling. Therefore, it can be defined as the logarithmic dependence between the intensity of incident light in a sample (*I*₀) and the intensity of light transmitted by it (*I*). Besides that, it relates the fraction of incident light absorbed at a particular wavelength (*λ*) with the molar absorption coefficient (*ε* in M⁻¹cm⁻¹), the sample concentration (*c* in M) and the optical path length (*l* in cm) [157]. Equation 3.1 represents the Beer-Lambert law and is provided below.

$$A(\lambda) = \log \frac{I_0}{I} = \varepsilon(\lambda)lc \leftrightarrow \varepsilon(\lambda) = \frac{A(\lambda)}{lc} \quad (3.1)$$

Based on this law and setting the optical path length to 1 cm, the molar absorption coefficients of Mn(III)TPP-*p*-CF₃ were established (Table 3.1). Several solutions were prepared with concentrations around 10⁻⁶ M, in THF. Then, a UV-Vis spectrum was collected for each solution and the maximum absorbance of each band was recorded. In the end, the adjustment of the results was carried out using a linear equation. The slope adjusting the linear regression to data corresponds to the molar absorption coefficient.

Table 3.1. Values of the molar absorption coefficients obtained for the different bands of Mn(III)TPP-*p*-CF₃.

Bands	Wavelength (nm)	Values of <i>ε</i> (M ⁻¹ cm ⁻¹)
Soret band	473	163 719.75
Q ₁ band	582	17 321.03
Q ₂ band	618	16 087.52

Figure 3.7 displays the graphical representation of absorbance as a function of concentration for the Soret band of Mn(III)TPP-*p*-CF₃.

The molar absorption coefficient obtained for the Soret band of the porphyrin was 163719.75 M⁻¹cm⁻¹. This result is consistent with the literature, as the molar absorption coefficient for the Soret band has been defined to be around 10⁵ M⁻¹cm⁻¹ [158]. Also, the R-squared, which measures the strength of the relationship between the linear regression model and the dependent variable, indicates that the adjustment model fits very well the

data ($R^2 = 0.99$). Therefore, it can be concluded that, in the concentration range used, there were no deviations from the Beer-Lambert law.

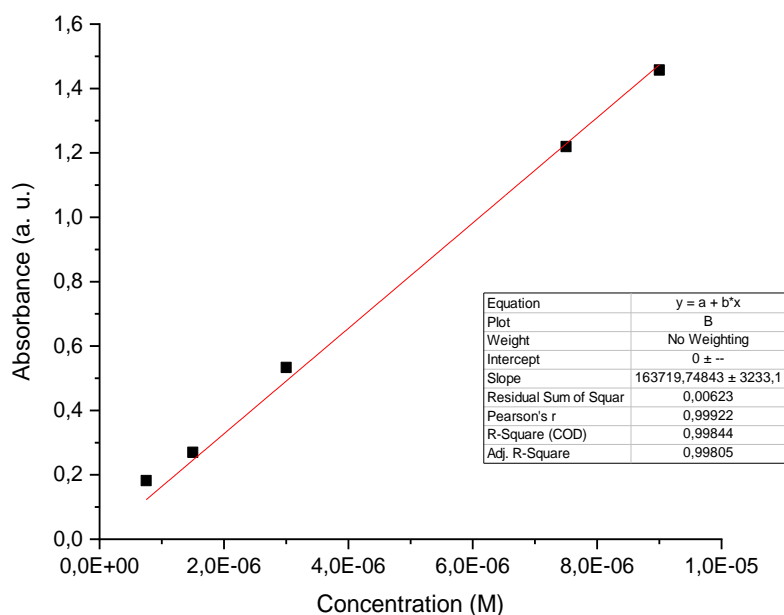


Figure 3.7. Linear fit of molar absorbance coefficient vs. concentration for the Soret band of Mn(III)TPP- p -CF $_3$, in THF.

The molar absorption coefficients for the Q bands were also established. The graphical representation of absorbance as a function of concentration for the Q bands Mn(III)TPP- p -CF $_3$ is expressed in Figure 3.8.

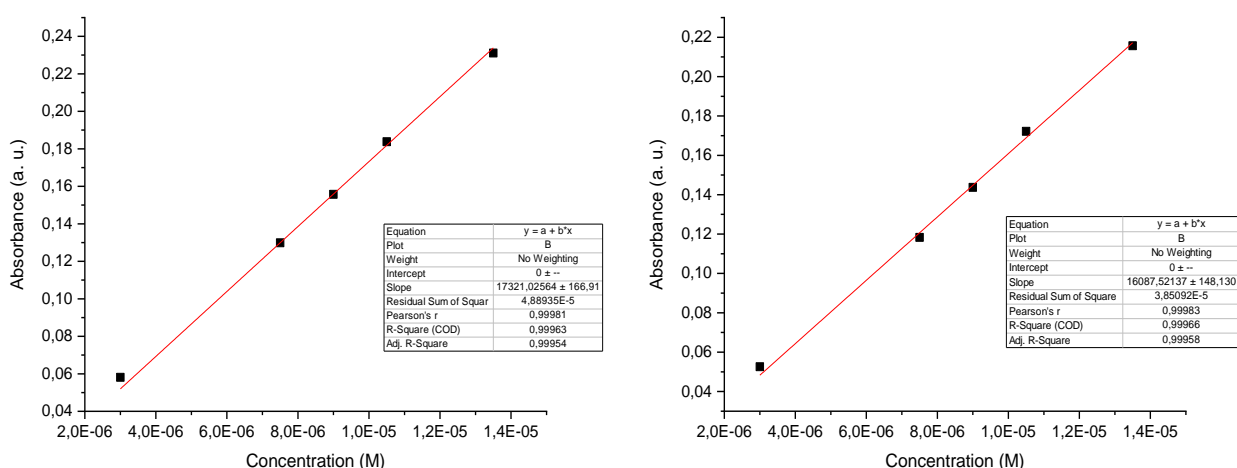


Figure 3.8. Linear regression model of molar absorbance coefficient for the Q bands of Mn(III)TPP- p -CF $_3$, in THF. The Q $_2$ band (with a wavelength of 618 nm) and the Q $_1$ band (with a wavelength of 582 nm on the right) are represented on the left, and on the right, respectively.

The molar absorption coefficient values acquired for the Q bands of the porphyrin were $16087.52 \text{ M}^{-1}\text{cm}^{-1}$ (Q $_2$: $\lambda = 618 \text{ nm}$) and $17321.03 \text{ M}^{-1}\text{cm}^{-1}$ (Q $_1$: $\lambda = 582 \text{ nm}$). These

results are in agreement with the literature, as the molar absorption coefficients for the Q band has been defined around $10^4 \text{ M}^{-1}\text{cm}^{-1}$ [158]. The values of R-squared obtained for the linear regression model fit properly the data ($R^2 = 0.99$). As a result, no deviations from the Beer-Lambert law were observed.

3.2.2. Reduction of Mn(III)TPP-*p*-CF₃

As the main goal of the Mn(III)TPP-*p*-CF₃ complex is to be applied as an MRI contrast agent and work as a “turn-off” redox probe, it must be reduced in the presence of intracellular reducing agents. In order to assess the possibility of reducing Mn^{III} to Mn^{II} in the porphyrin, two important biological reductants present in the organism were used - ascorbic acid and glutathione.

3.2.2.1. Study Performed with Ascorbic Acid

The reduction of the complex with ascorbic acid was followed by UV-Vis spectroscopy since it is a powerful antioxidant capable of reducing other molecules and it is present in the organism in a significant concentration. The experiment was carried out in two solvents: DMSO and THF. In both experiments, the Mn^{III} porphyrin solution was placed in the quartz cell and increasing amounts of the reductant were added. Tetrahydrofuran is a colourless cyclic ether commonly used as an organic solvent that can be miscible with water and have low viscosity [159]. It is considered an aprotic solvent able to dissolve a wide range of nonpolar and polar organic compounds, being very versatile [160]. Figure 3.9 shows the results of the experiment carried out using THF.

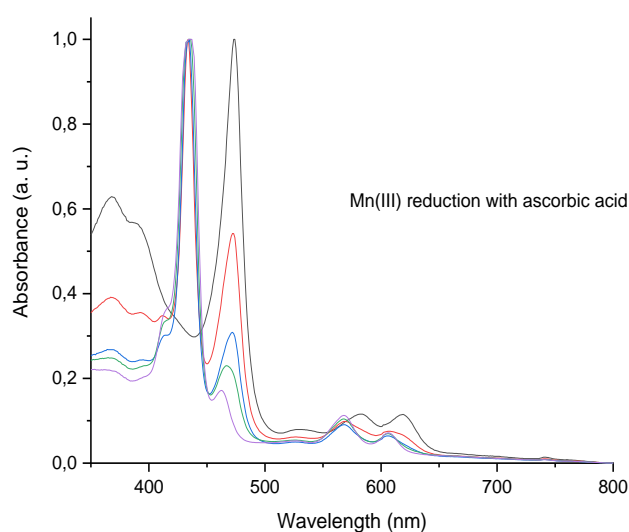


Figure 3.9. UV-Vis reduction titration of 0.0125 mM Mn(III)TPP-*p*-CF₃ with ascorbic acid, recorded in THF (25°C). Number of equivalents of ascorbic acid added: 0 (black line); 0.87 (red line); 2.18 (blue line); 3.93 (green line); 12.65 (purple line).

The addition of ascorbic acid in water to the solution changed the oxidation state of manganese in the porphyrin from Mn^{III} to Mn^{II} . This event can be verified through the analysis of the UV-Vis spectrum. The addition of 0.87 equivalents of the reductant induced a decrease in the absorption at 473 nm, which is the typical wavelength for the charge transfer Soret band (band V) of Mn^{III} porphyrins, with the concomitant appearance of a new band at 432 nm, the typical absorption wavelength of this band for Mn^{II} porphyrins. Through the addition of larger volumes of ascorbic acid, this effect becomes increasingly notable, not only in the Soret band but also in the Q bands of the Mn^{III} porphyrin. The increase of the % water in the THF solution with successive additions of the reductant solution did not affect the position of the Soret and Q bands. The total reduction of Mn^{III} to Mn^{II} was achieved after adding 12.65 equivalents of ascorbic acid. The need for a large excess of ascorbic acid to observe the reduction in the short time of acquiring the UV-Vis spectrum does not tell anything about the stoichiometry of the reaction, which can be obtained in a time-dependent study [63]. This result is in line with what would be expected, considering that ascorbic acid is a powerful reducing agent ($E^{\circ} = +0.184$ V at pH 7.4) [160], capable of reducing several metals. Also, it agrees with the study of the reduction of $\text{Mn}(\text{III})\text{-TTFPP}$ -(pPEG_{500}) with ascorbic acid in the literature, which was explained by the capacity of the ascorbate molecule to coordinate in the axial position of the $\text{Mn}(\text{III})$ to perform electron transfer to the metal centre in a thermodynamically and kinetically allowed reaction [63]

Conversely, oxidation of Mn^{II} to Mn^{III} in the $\text{Mn}(\text{III})\text{TPP-}p\text{-CF}_3$ porphyrin was evaluated by acquiring the UV-Vis spectrum of the $\text{Mn}(\text{III})\text{TPP-}p\text{-CF}_3$ in THF solution after 1 hour of exposure to air (Figure 3.10). The system displayed some reversibility within a short period of time.

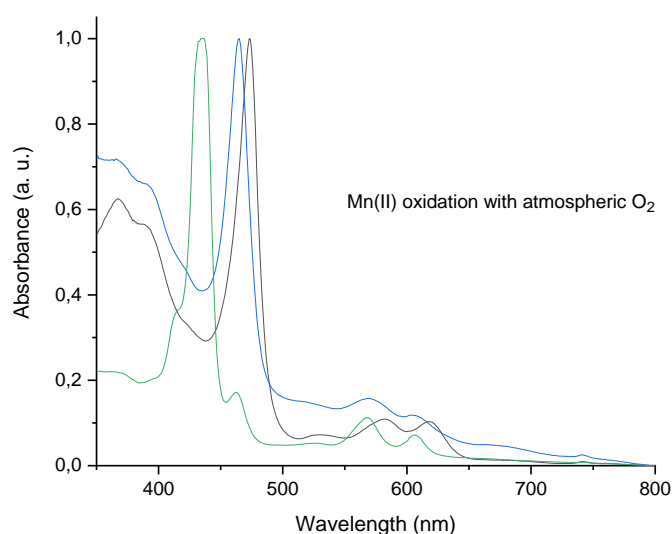


Figure 3.10. UV-Vis spectrum of the reoxidation of $\text{Mn}(\text{II})\text{TPP-}p\text{-CF}_3$ (green line) in THF, obtained upon air exposure after 1 hour. Complete conversion to Mn^{III} was attained (blue line). The initial $\text{Mn}(\text{III})\text{TPP-}p\text{-CF}_3$ spectrum is represented by the black line.

After 1 hour of air exposure, the effect of air oxygen as an oxidizing agent was perceived in the THF solution, containing Mn(II)TPP-*p*-CF₃. Oxygen is a strong oxidizing agent, able to react with multiple elements and compounds. According to the spectrum, the Soret band at 432 nm of the Mn^{II} porphyrin disappeared, and a new band at 465 nm appeared, which suggests the complete reoxidation of Mn^{II} to Mn^{III}, considering this a typical wavelength of the Soret band of Mn^{III} porphyrins. Even though the Soret band and the Q bands appeared slightly shifted from the initial Mn^{III} porphyrin wavelength, the oxidation state of the porphyrin increased, most probably to Mn^{III}. This should be later confirmed by cyclic voltammetry and NMR spectroscopy.

To complete the reduction study with ascorbic acid in THF, a time-dependent experiment was carried out. Therefore, 0.87 equivalents of ascorbic acid were added to the Mn^{III} solution, and successive spectra were acquired over a period of time, in order to verify whether a small amount of ascorbic acid produced the same reduction effect over a longer acquisition time (Figure 3.11).

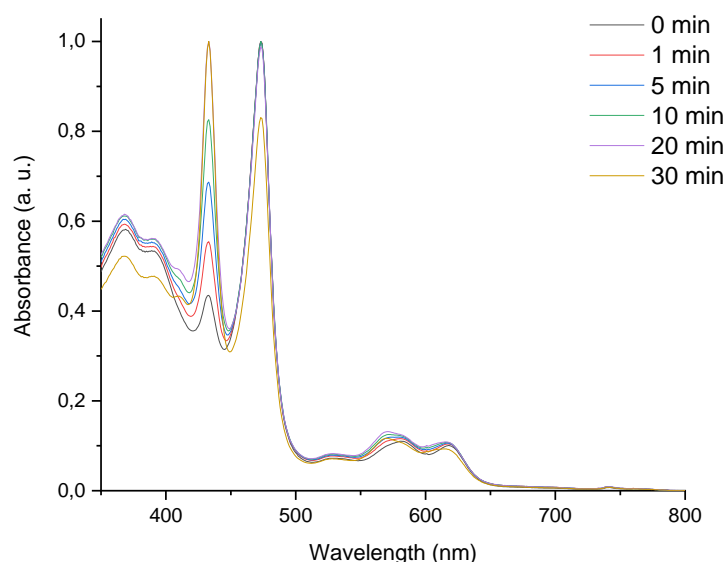


Figure 3.11. UV-Vis reduction spectra of 0.0125 mM Mn(III)TPP-*p*-CF₃ with 0.87 equivalents of ascorbic acid, recorded in THF (25°C). The spectra were acquired in different time points: 0 min (black line); 1 min (red line); 5 min (blue line); 10 min (green line); 20 (purple line); 30 min (orange line).

It can be seen that, by adding a smaller amount of ascorbic acid equivalents, the reduction to Mn^{II} also takes place over time. After 30 minutes, it is verified that the Mn^{II} band has a high intensity, which means that the manganese is gradually reduced over time. However, the Mn^{III} band only decreases slightly, indicating that a greater amount of the reducing agent is needed to achieve the complete reduction. In the future, the same experiment should be carried out by adding larger volumes of ascorbic acid.

The same experiment was repeated using DMSO, which is an important aprotic solvent capable of solubilizing a wide variety of poorly soluble polar and nonpolar molecules [161]. In this way, it is miscible with a broad range of organic solvents along with water [162]. This, coupled with its apparent low toxicity at concentrations below 10%, has led to its extensive use and widespread application [163]. DMSO is employed as a solvent for many drug types and is often used as the vehicle control-of-choice for both *in vitro* and *in vivo* studies [164]. Analogously, the reduction of Mn(III)TPP-*p*-CF₃ with aqueous ascorbic acid was monitored by UV-Vis spectroscopy, by placing the Mn(III)TPP-*p*-CF₃ solution in the cell and adding increasing amounts of the reductant, until total conversion of Mn^{III} to Mn^{II}. The reoxidation of Mn^{II} to Mn^{III} was evaluated by applying the same method as specified above (Figure 3.12).

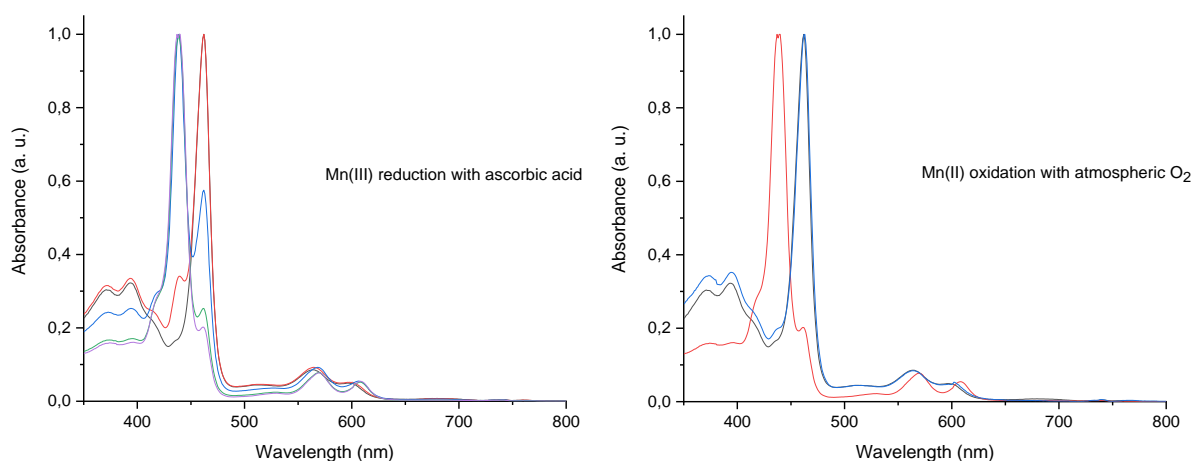


Figure 3.12. UV-Vis reduction titration of 0.0125 mM Mn(III)TPP-*p*-CF₃ with ascorbic acid, recorded in DMSO (25°C) (left), and reoxidation of Mn(II)TPP-*p*-CF₃ obtained upon air exposure after 1 hour (right). Left: number of equivalents of ascorbic acid added: 0 (black line); 2.50 (red line); 8.35 (blue line); 12.52 (green line); 16.70 (purple line). Right: initial Mn(III)TPP-*p*-CF₃ (black line); Mn(II)TPP-*p*-CF₃ (red line); complete reoxidation to Mn^{III} (blue line).

By adding aqueous ascorbic acid to the solution, the oxidation state of manganese changed from Mn^{III} to Mn^{II}. This event can be confirmed through the analysis of the spectrum. By adding 2.50 equivalents of the reductant there was not a significant effect on the oxidation number of the complex. Nevertheless, the addition of 8.35 equivalents of ascorbic acid induced a decrease in the absorption band at 462 nm (corresponding to the Mn^{III}-porphyrin), with the simultaneous appearance of a new band at 438 nm, related to the Mn^{II}-porphyrin. This effect has become more notable as larger volumes of ascorbic acid were added to the mixture. The total reduction of Mn^{III} to Mn^{II} was achieved after adding 16.70 equivalents of the reducing agent. It should be noted that a larger number of equivalents were needed to achieve the complete conversion to the Mn^{II}-porphyrin in

DMSO than in THF, during the same recording time, indicating that the redox reaction is slower in DMSO than in THF. THF has a much lower static dielectric constant ($\epsilon_s = 7.58$) than DMSO ($\epsilon_s = 46.7$). This observation is in agreement with Marcus theory of electron transfer [165]. Using DMSO as a solvent, the Soret band of the Mn^{III}-porphyrin appeared at a lower wavelength (462 nm) than in THF (473 nm). On the other hand, the Soret band of the Mn^{II}-porphyrin appeared at a higher wavelength (438 nm) than in THF (432 nm). Also, the system displayed some reversibility after 1 hour of air exposure, changing the Mn^{II} redox state to Mn^{III}.

This study was performed in two different organic solvents to evaluate if the results obtained agree, and to determine which solvent is most advantageous to be used in the probe characterization. It can be concluded that, Mn(III)TPP-*p*-CF₃ in the presence of ascorbic acid responds reversibly and relatively quickly to this reducing agent, changing the oxidation state of manganese from Mn^{III} to Mn^{II}, but also that Mn^{II} can be reoxidized upon air exposure within one hour. This result may indicate that the Mn(III)TPP-*p*-CF₃ complex can be used as a “turn-off” probe for MRI application.

3.2.2.2. Study Performed with Glutathione

Subsequently, the same experiment was carried out using glutathione as a reducing agent, considering the large reducing capacity of this ubiquitous endogenous antioxidant. The experiment was followed by UV-Vis spectroscopy and it was recorded in both solvents (DMSO and THF) by adding increasing amounts of the aqueous reductant (Figure 3.13).

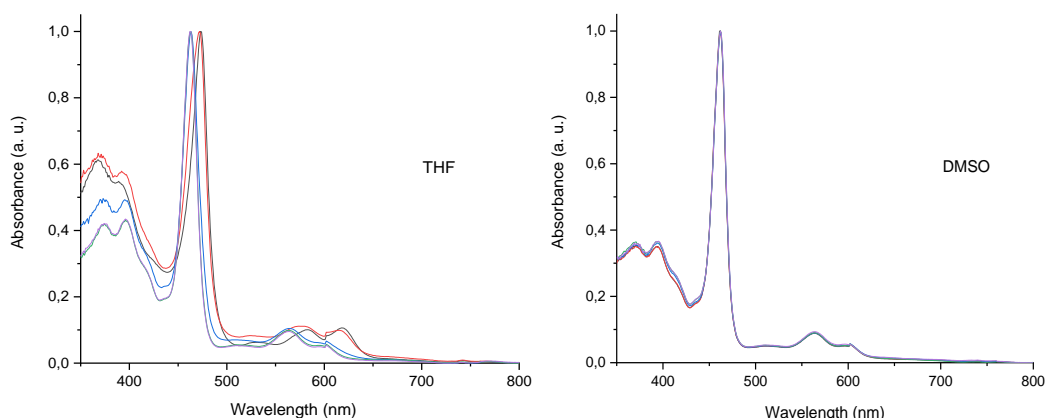


Figure 3.13. UV-Vis spectra of Mn(III)TPP-*p*-CF₃ solutions upon addition of glutathione, recorded in THF (left) and DMSO (right) (25°C). The number of equivalents of glutathione added: 0 (black line); 2.50 (red line); 8.35 (blue line); 12.52 (green line); 16.70 (purple line).

It can be noticed that the oxidation state of manganese did not change from Mn^{III} upon the addition of aqueous glutathione to the Mn(III)TPP-*p*-CF₃ solution, in both solvents.

Even after adding a large excess of the reductant, the Soret band did not appear at the expected values (432 nm in THF, 438 nm in DMSO), characteristic of the Mn^{II} -porphyrin. However, there was a slight change in the wavelength of the Soret band (from 473 nm to 462 nm) and the Q bands (in the THF solution), as the water content increased, which was not seen in DMSO.

Since no effect was observed in the presence of glutathione, even in a large excess of this important biological reductant, it can be concluded that glutathione is not capable of reducing this probe. This fact is thermodynamically unexpected considering that the redox potential ($E^{0'} = -240$ mV) of the GSH/GSSG couple is most probably negative enough to reduce Mn^{III} to Mn^{II} in this porphyrin. Although its redox potential has not yet been determined (should be done by CV in future studies), the conclusion above is supported by the value of $E^{0'}_{\text{Mn}^{\text{III}}/\text{Mn}^{\text{II}}} = +0.193$ mV, obtained for the similar $\text{Mn}(\text{III})\text{-TTFPP-(pPEG)}_{500}$ porphyrin [63]. This can be attributed to the binding of the terminal carboxylate groups of glutathione to the paramagnetic metal ion in the axial position of Mn^{III} , which kinetically prevents the reduction [63]

3.2.3. ^1H and ^{19}F Study

The reduction of $\text{Mn}(\text{III})\text{TPP-}p\text{-CF}_3$ by aqueous ascorbic acid was studied by ^1H NMR. Figure 3.14 shows that the proton signal at 7.85 ppm, corresponding to the aryl groups of the Mn^{III} -porphyrin, disappears in the presence of ascorbate, due to the extreme broadening effect of Mn^{II} in the reduced Mn^{II} -porphyrin. However, the quantitation of the oxidized porphyrin in solution was not possible, as a result of the broadness of the peak at 7.85 ppm.

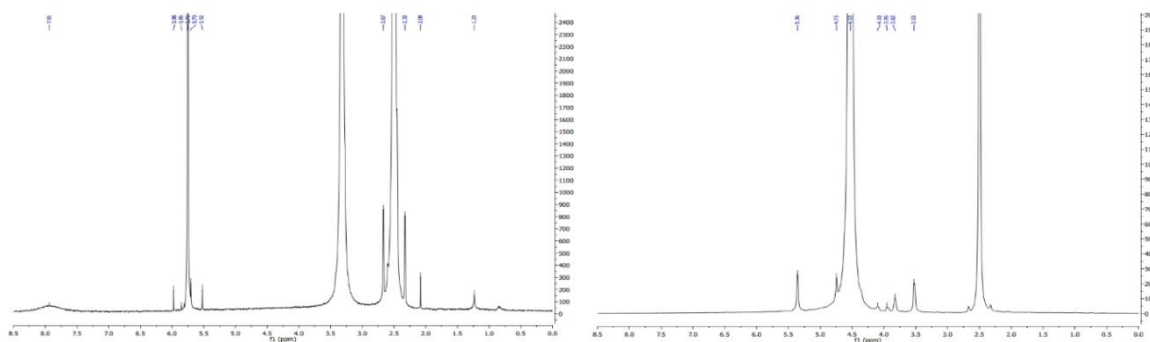


Figure 3.14. ^1H NMR spectra of 0.6 mM $\text{Mn}(\text{III})\text{TPP-}p\text{-CF}_3$ before (left) and after (right) addition 16.70 equivalents of aqueous ascorbic acid, recorded in deuterated DMSO (25°C). (Number of scans = 143; acquisition time = 0.82 s).

An important aspect of ^{19}F NMR studies is the broader chemical shift range compared with ^1H NMR spectroscopy. This aspect has promoted the development of ^{19}F

magnetic resonance to follow changes in the composition of fluorinated compounds, for example in metabolic studies *in vivo* of a fluorinated drug [166]. Moreover, it has encouraged the creation of fluorinated probes, in which the observed chemical shifts report on their local environment [167]. Some examples of such “responsive probes” are the ones in which the chemical shifts report an irreversible transformation of the fluorinated probe (for instance, by bond cleavage catalysed by an endogenous enzyme) and the ones involving a reversible process, induced by modulation of the local chemical environment (measuring changes in temperature, pH value, metal ion concentration, O_2 , or specific gene reporters) [26]. A change in the conformation of the complex can also be coupled to other local parameters, e.g., redox potential and dielectric constant.

The reduction of Mn(III)TPP-*p*-CF₃ was also followed by ^{19}F NMR spectroscopy by adding increasing amounts of ascorbic acid, as displayed in Figure 3.15.

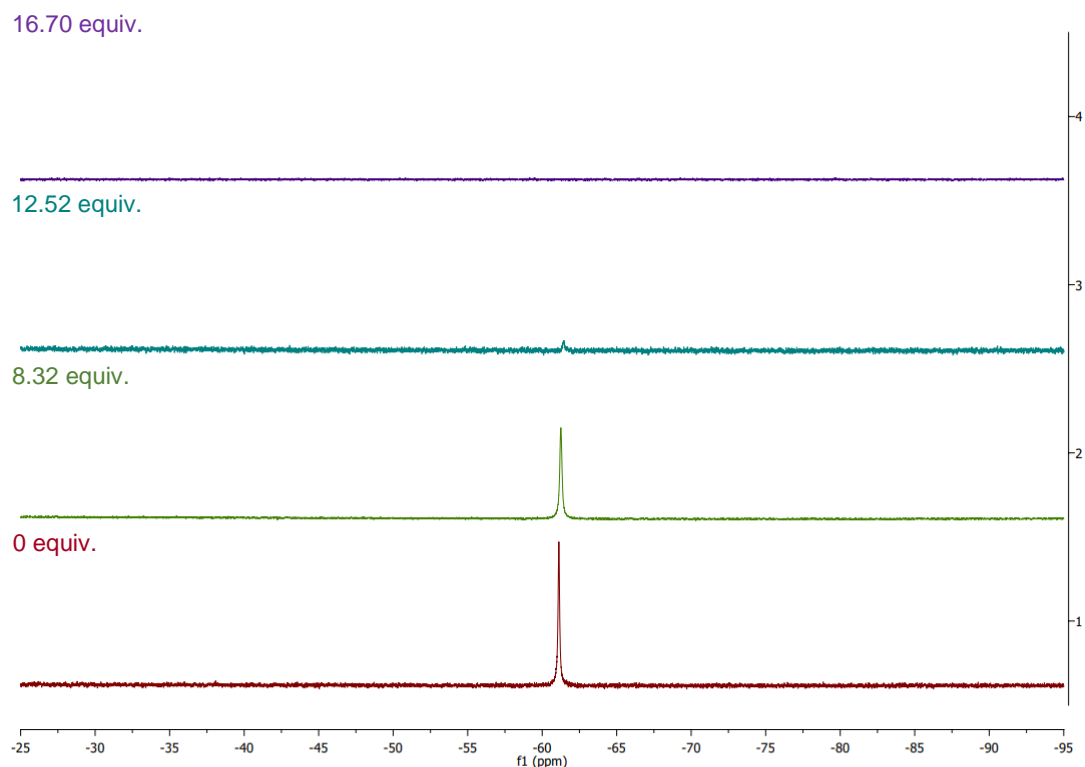


Figure 3.15. ^{19}F NMR spectral titration of 0.6 mM Mn(III)TPP-*p*-CF₃ with ascorbic acid, recorded in deuterated DMSO (25°C). Number of equivalents of ascorbic acid added: 0 (red line); 8.32 (green line); 12.52 (blue line); 16.70 (purple line). (Number of scans = 123; acquisition time = 0.5 s).

Analysing Figure 3.15, it can be noticed that the ^{19}F NMR spectrum of the Mn^{III}-porphyrin before the addition of ascorbic acid shows a high-intensity well-defined ^{19}F NMR signal, as discussed above. As an increasing number of ascorbic acid equivalents are added to the Mn^{III} complex, a continuous decrease of the signal is observed, until its

disappearance, after the addition of more than 16 equivalents, during the time after the addition and recording of the spectra. This is justified by the reduction of Mn^{III} to Mn^{II} in the porphyrin, induced by ascorbic acid. The broadening of the ^{19}F signal in the Mn^{III} porphyrin, which is far away from the metal, is very small, as the ion causes a slow relaxation rate in ^{19}F , making it possible to be detected. However, as Mn^{II} causes a much larger T_1/T_2 relaxation than Mn^{III} , it broadens the ^{19}F NMR signal of the Mn^{II} -porphyrin beyond detection, as the linewidth of the signal is inversely proportional to the observed T_2 value. As a result, the reduced Mn^{II} -porphyrin becomes undetectable in ^{19}F NMR and MRI, therefore it has the potential to be used as a “turn-off” redox responsive contrast agent for ^{19}F MRI, facilitating the identification of regions or tissues with a strong reducing character, such as in the case of tumours.

3.2.4. Reduction kinetics of Mn(III)TPP-*p*-CF₃

The reduction kinetics of Mn(III)TPP-*p*-CF₃ in DMSO-d₆ upon addition of 2.5 equivalents of an aqueous solution of ascorbic acid in D₂O was followed by ^{19}F NMR, in a time-dependent variation, undertaken pseudo-first-order conditions. The conversion of Mn^{III} to Mn^{II} was monitored by the decrease of the signal intensity of the fluorine singlet in ^{19}F NMR. The reduction of the complex in the presence of excess ascorbic acid was monitored over time, at intervals of 1 minute, particularly between 3 and 40 minutes after the addition of the reducing agent (Figure 3.16).

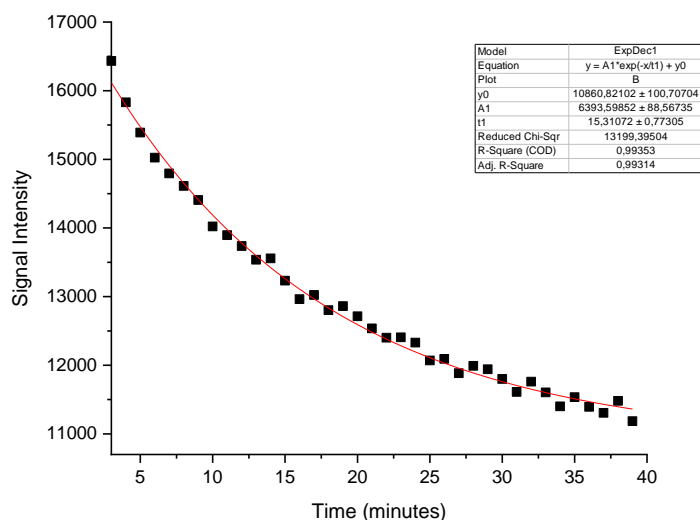


Figure 3.16. Reduction kinetics of 0.6 mM Mn(III)TPP-*p*-CF₃ in DMSO-d₆ upon addition of 2.5 equivalents of ascorbic acid in D₂O (25°C).

Figure 3.16 shows the observed time-dependent decrease of the signal intensity of Mn(III)TPP-*p*-CF₃ in the presence of excess ascorbic acid, which results in equation 3.2:

$$y = y_0 + A_1 e^{-t/t_1} \quad (3.2)$$

where $y = I(t)$, $y_0 = I_\infty$ and $A_1 = (I_0 - I_\infty)$ represent the ¹⁹F NMR signal intensity (arbitrary units) observed at times t , ∞ , 0 and at the 0 to ∞ decay, and $t_1 = 1/k_{app}$, where k_{app} is the observed pseudo-first-order rate constant. A non-linear least-squares fit of the data provided the values shown in Figure 3.16, giving a value of $t_1 = 15.31 \pm 0.77$ min ($R^2 = 0.993$), corresponding to $k_{app} = 1.09 \times 10^{-3} \text{ s}^{-1}$. As $k_{app} = k_2 [AA]_0$ ($[AA]_0 = 1.5 \text{ mM}$), the calculated second order kinetic constant is $k_2 = 0,727 \text{ mM}^{-1} \text{ s}^{-1}$.

The same experiment was also performed with the addition of 0.87 and 8.32 equivalents of ascorbic acid. The reduction kinetics with 0.87 equivalents was quite slow, with no significant decrease in the intensity of the fluorine signal. Likewise, the addition of 8.32 equivalents did not provide conclusive information about the reduction kinetics of Mn(III)TPP-*p*-CF₃ with ascorbic acid.

3.2.5. ¹⁹F NMR Relaxometry

As previously discussed, this study focuses on the development of a potential redox responsive contrast agent for application in ¹⁹F MRI. The fluorine nucleus is an attractive probe for chemical and biological magnetic resonance studies, considering the fact that in the human body its concentration is lower than 10⁻⁶ M, and therefore, the image signal detected results only from the contrast agent. However, ¹⁹F has a slow longitudinal relaxation rate ($R_1 = 1/T_1$ between 0.5 and 1 s⁻¹), which entails a large acquisition time [168]. The literature reports several studies of fluorine-based complexes containing paramagnetic centres (such as a d- or f- block metal ion or complex) capable of interacting with the fluorine nucleus or perfluorinated groups, as a strategy to overcome this problem. Thus, ¹⁹F T₁ will be reduced from values of the order of 1 s to about 10 ms, enabling a faster data acquisition *per* unit of time. It is important to emphasize that the concomitant decrease in T₂ acquisition time should not impair detection sensitivity too much [150,169,170].

The ¹⁹F T₁ and T₂ relaxation times of TPP-*p*-CF₃ and Mn(III)TPP-*p*-CF₃ in DMSO-d₆ (25°C) were measured and are presented in Table 3.2.

Table 3.2. Values of ¹⁹F T₁ and T₂ relaxation times (ms), and respective R₁ and R₂ relaxation rates (s⁻¹), for TPP-*p*-CF₃ and Mn(III)TPP-*p*-CF₃ solutions (0.6 mM), in DMSO-d₆ (25°C).

Compound	T ₁ (ms)	R ₁ (s ⁻¹)	T ₂ (ms)	R ₂ (s ⁻¹)
TPP- <i>p</i> -CF ₃	916	1.09	6.52	153.37
Mn(III)TPP- <i>p</i> -CF ₃	14	71.43	3	333.33

Experimentally, the values obtained for T₁ and T₂ relaxation times of TPP-*p*-CF₃ were 916 ms and 6.52 ms, respectively. The very short T₂ value is due to the contribution of the spin-rotation mechanism to ¹⁹F relaxation, which results from the coupling of the ¹⁹F nuclear magnetic moment (μ_{19F}) with the rotational magnetic moment, resulting from the coherent rotational motion of the electronic density of the F atom during the rotation of the molecule (μ_{Jr}). This creates a local magnetic moment at the ¹⁹F nucleus which fluctuates with molecular collisions and causes nuclear relaxation. This relaxation mechanism is dominant for ¹⁹F nuclei in diamagnetic molecules [23]. On the other hand, for the Mn^{III} complex, the value of T₁ was 14 ms and that of T₂ was 3 ms due to the paramagnetic dipolar relaxation induced by the Mn^{III} centre at the nucleus. Indeed, it can be confirmed that the presence of Mn^{III} decreases both relaxation times, as expected. The largest decrease is observed in the T₁ relaxation time, which goes from 916 ms to 14 ms. However, the largest paramagnetic contribution to the relaxation rates of ¹⁹F ($R_{iM} = R_{ip} - R_{id}$, $i = 1, 2$, where R_{ip} and R_{id} are the observed rates for the paramagnetic complex and diamagnetic ligand) is for R₂, as expected ($R_{2M} = 179.96 \text{ s}^{-1}$, vs $R_{1M} = 70.34 \text{ s}^{-1}$). This substantial effect on the R₁ relaxation rate without an excessive effect on R₂ (not too much signal broadening) proves the potential of the Mn(III)TPP-*p*-CF₃ complex as a contrast agent for ¹⁹F MRI, allowing the acquisition of sufficient signal intensity in a reasonable time period. The disappearance of the ¹⁹F signal of the reduced form Mn(II)TPP-*p*-CF₃ shows that it can be used as a “turn-off” redox responsive ¹⁹F MRI contrast agent.

In addition, the distance (r_{Mn-F}) between the paramagnetic metal centre and the ¹⁹F nuclei in the fluorinated probe must be considered, as the values of R_{1M} and R_{2M} are proportional to $(1/r_{Mn-F})^6$ [169,170]. For instance, if there is an intermolecular interaction between them, then the encounter probability is reduced, and the relaxation enhancement effect will be limited. Furthermore, a more functional approach is to make the interaction intramolecular by positioning the ¹⁹F nucleus at a fixed distance from the paramagnetic ion, preferably in the range 4.5 and 7.5 Å [169]. If the distance is too close, the effect will be severe, and if it is too distant, the longitudinal relaxation time rate increases just a little and the sensitivity gain is much shortened [170]. This effect was confirmed in some previous studies carried out by the group of Catálise e Química Fina, of the University of Coimbra.

3.3. Inclusion of Mn(III)TPP-*p*-CF₃ into γ -cyclodextrin

3.3.1. Inclusion Study

Considering the fact that the Mn(III)TPP-*p*-CF₃ complex is non-water-soluble, a strategy to overcome this obstacle was established. In order to increase its solubility in water, an experiment based on the inclusion of the complex into two cyclodextrins (methyl- β -CD and γ -CD) was performed, since one of the goals of this study includes its application *in vitro*. It is important to highlight that the chosen cyclodextrins were those that display a greater enhancement regarding the hydrosolubility of molecules/drugs, according to the literature.

For that purpose, multiple solutions containing the Mn^{III} complex and one of the two tested cyclodextrins (methyl- β -CD and γ -CD) were prepared with concentrations around 10^{-4} M. Then, a UV-Vis spectrum of each solution was collected to estimate the behaviour of both compounds in solution (Figure 3.17).

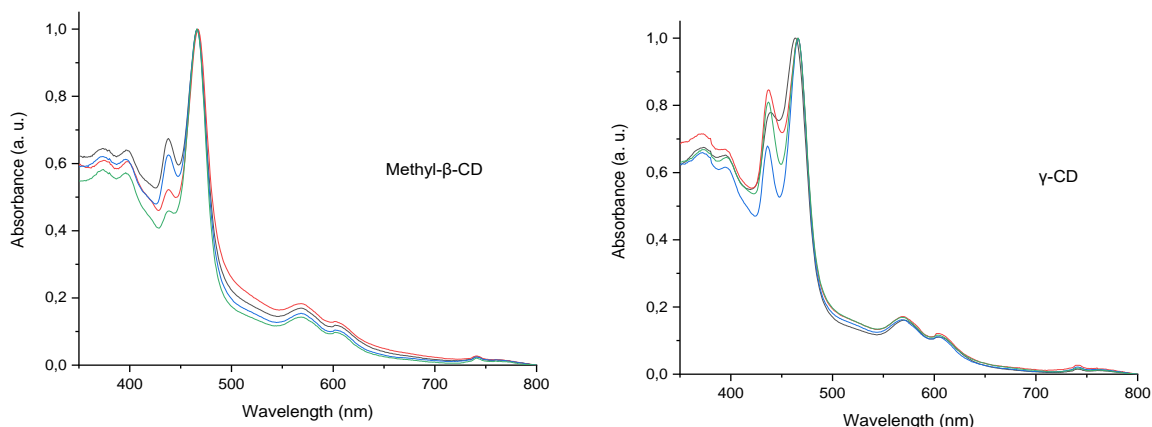


Figure 3.17. UV-Vis spectra obtained for the solutions containing 0.0052 mM Mn(III)TPP-*p*-CF₃ and CDs (methyl- β -CD, on the left, and γ -CD, on the right). Concentrations of cyclodextrin in the prepared solutions: 0.1 mM (black line); 0.2 mM (red line); 0.4 mM (blue line); 0.5 mM (green line).

The addition of aqueous cyclodextrin solution to the complex causes a slight change in the UV-Vis spectra, compared with that of Mn(III)TPP-*p*-CF₃ in THF (Figure 3.9), which suggests the existence of some sort of interaction between the two compounds (using both cyclodextrins). Analysing the obtained spectra, it is possible to identify the same bands of Mn(III)TPP-*p*-CF₃ - the two Q bands and the Soret band, of high intensity. However, in both cases, the addition of cyclodextrin to the solution also stabilizes the Mn^{II} oxidation state, with the concomitant appearance of the Mn(II)TPP-*p*-CF₃ Soret band (432 nm). The intensity of this band was highly influenced by the time of exposure to the atmospheric air,

obtaining a higher or lesser intensity depending on this factor, suggesting that the product of its interaction may not be kinetically stable [171]. Moreover, to carry out this study, different concentrations of both cyclodextrins were tested, since the γ -CD*Mn(III)TPP-*p*-CF₃ stoichiometry was unknown.

For the remaining studies, γ -CD was chosen as it has the largest cavity and ideally would be more suitable with the aim of the work (inclusion of the meso aryl groups of the porphyrin).

3.3.2. Reduction of γ -CD*Mn(III)TPP-*p*-CF₃

It was also essential to verify whether the γ -CD*Mn(III)TPP-*p*-CF₃ complex was reduced in the presence of ascorbic acid, similar to what happened with Mn(III)TPP-*p*-CF₃, take into account the fact that the complex still must work as a “turn-off” probe for application in ¹⁹F MRI. Therefore, the reduction of several solutions containing the Mn(III)TPP-*p*-CF₃ complex and different concentrations of γ -CD (the same as used above) with ascorbic acid was followed by UV-Vis spectroscopy. The multiple solutions were prepared as described in section 2.7.1., and increasing amounts of the reductant were added, as demonstrated in Figure 3.18.

Through the spectral analysis of the different solutions, it can be noticed that the addition of ascorbic acid induced the reduction of Mn^{III} to Mn^{II} oxidation state, as desired. A small number of equivalents of ascorbic acid (7.57 equivalents) was enough to achieve almost the complete reduction of the complex, for the solutions with the lower concentrations of γ -CD (0.1 and 0.2 mM). However, for the 0.4 mM and 0.5 mM of γ -CD solutions, a large number of equivalents (23.49 equivalents) were needed to produce the same effect. Therefore, the presence of γ -CD hinders the reduction of Mn^{III} to Mn^{II} in the porphyrin by ascorbic acid. This could be explained by the steric hindrance of the binding of ascorbate to the axial position of Mn^{III} in the porphyrin, which is needed for the electron transfer process leading to reduction of Mn^{III} [63], by the γ -CD, when forming inclusion complexes with the meso aryl groups of the porphyrin, probably with 1:1 and 1:2 porphyrin/ γ -CD stoichiometries. More importantly, it should be noted that for none of the solutions a complete reduction of the metal was achieved, always being present the coexistence of both oxidation states of the metal in solution – Mn^{III} and Mn^{II}. This probably results from a balance of the reductive effects of ascorbate and γ -CD, and the oxidative effect of air oxygen complemented by the reduction hindering effect of γ -CD.

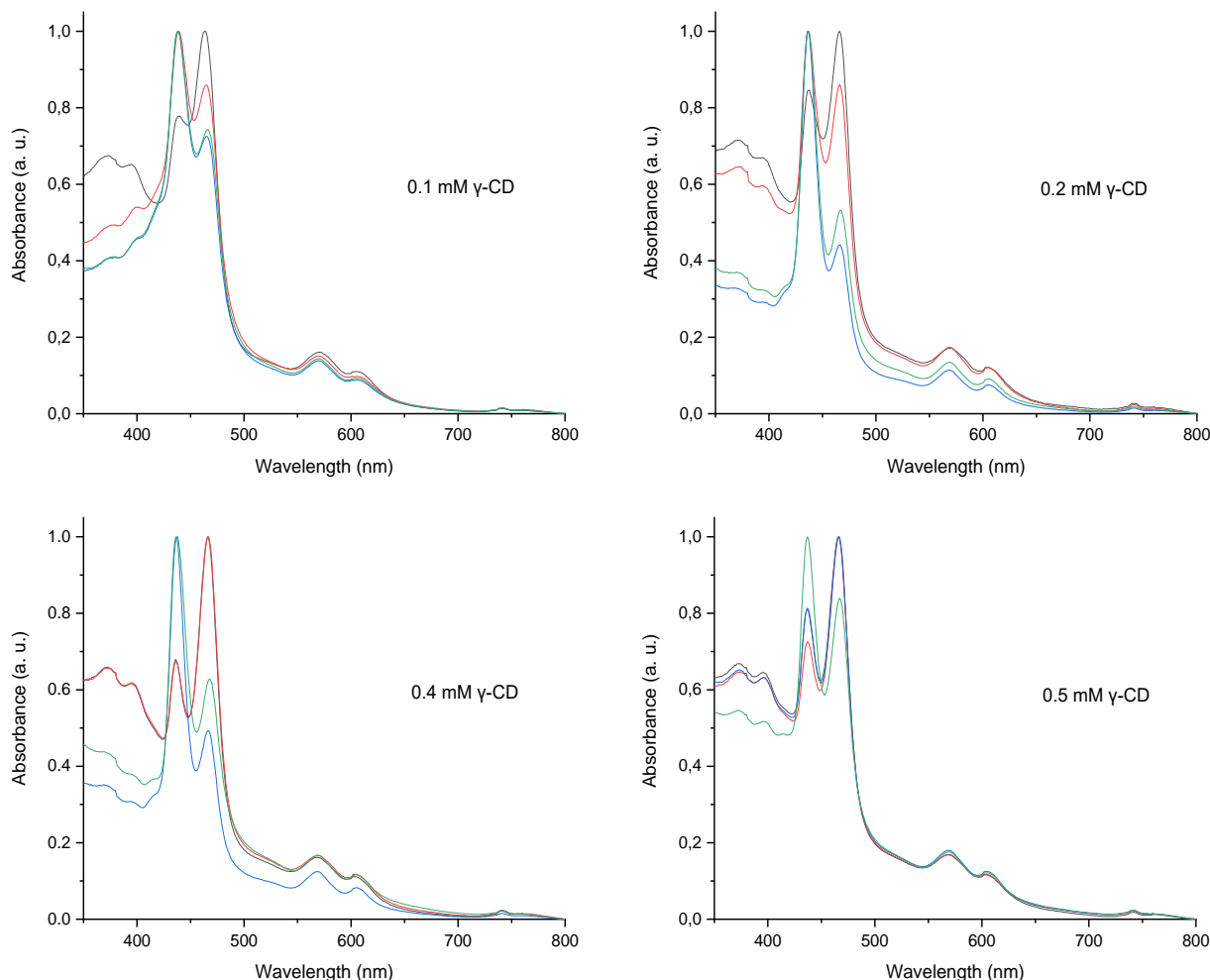


Figure 3.18. UV-Vis reduction titration spectra of the solutions containing 0.0052 mM Mn(III)TPP-*p*-CF₃ and different concentrations of γ -CD. Number of equivalents of ascorbic acid added: 0 (black line); 2.35 (red line); 7.57 (green line); 23.49 (blue line).

3.3.3. ^1H and ^{19}F NMR Study

NMR is one of the techniques that can best support evidence for the inclusion of a guest molecule into a hydrophobic cyclodextrin cavity in solution. The inclusion of Mn(III)TPP-*p*-CF₃ into γ -CD can, in principle, be proven by the change in the proton chemical shifts of the guest Mn(III)TPP-*p*-CF₃, which were too broad to be used, and those of the host γ -CD protons in the supramolecular complex, in comparison with the chemical shifts of the same protons in the free components. Also, ^{19}F NMR can provide relevant information about the interaction of these molecules. The titration of Mn(III)TPP-*p*-CF₃ into

γ -CD was followed by both ^1H and ^{19}F NMR spectroscopy, as shown in Figures 3.19 and Figure 3.20, respectively.

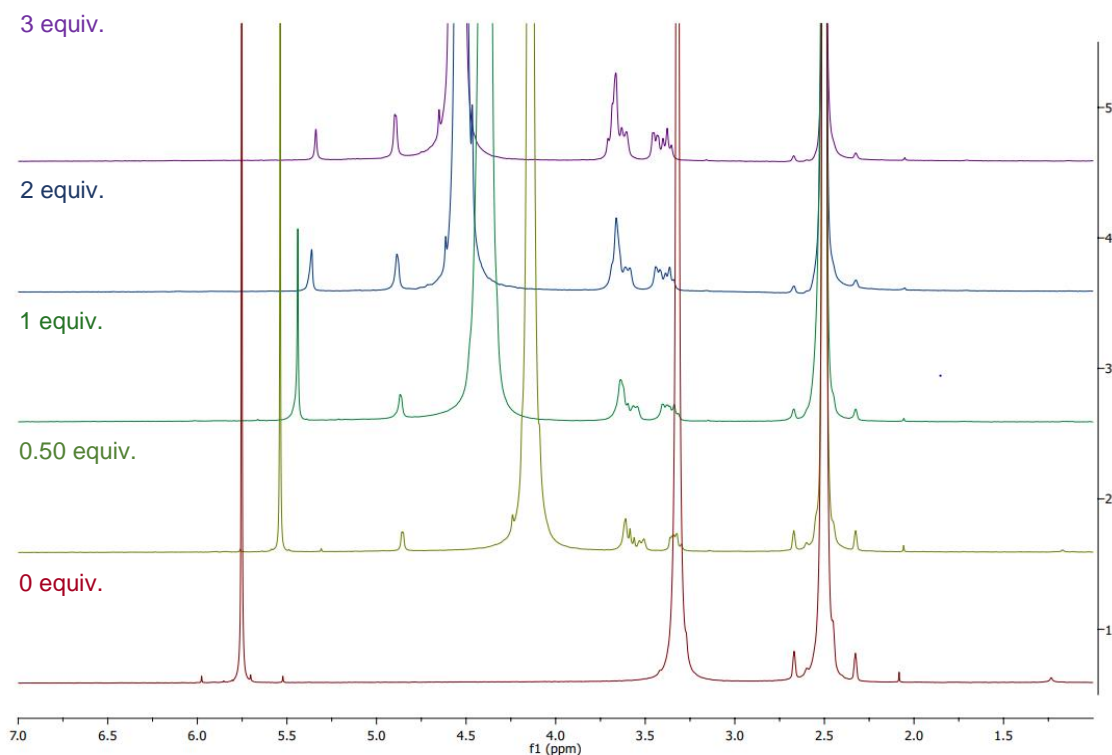


Figure 3.19. ^1H NMR spectra titration of 0.5 mM Mn(III)TPP-*p*-CF₃ in DMSO-*d*₆ (25°C) upon addition of aqueous γ -CD. Number of equivalents of γ -CD added: 0 (red line); 0.50 (light green line); 1 (dark green line); 2 (blue line); 3 (purple line). (Number of scans = 143; acquisition time = 0.82 s).

The ^1H NMR spectrum of Mn(III)TPP-*p*-CF₃ in DMSO-*d*₆ shows the residual non-deuterated DMSO CH₃ signal at 2.50 ppm (used as internal shift reference), the residual HDO water at 3.30 ppm and a signal at 5.75 ppm from an impurity. The broad resonance from the Mn^{III}-porphyrin aryl groups at 7.85 ppm is outside the plotted shift range (Figure 3.4). Upon the addition of increasing amounts of a D₂O solution of γ -CD, the HDO signal increased its intensity due to the presence of more water in the D₂O/DMSO-*d*₆ mixture, and shifted from 3.30 ppm to 4.50 ppm, due to hydrogen bonding of HDO with the DMSO oxygens. More importantly, the γ -CD proton signals, increase their intensity proportionally to the concentration of added γ -CD, becoming broader due to the proximity of the Mn^{III} paramagnetic centre, and shift H₁ to lower frequencies and the others to higher frequencies. The complexation-induced chemical shifts of the protons in the internal cavity of γ -CD resulting from their interaction with the meso aryl groups of Mn(III)TPP-*p*-CF₃, which are oriented towards the γ -CD cavity, confirming the formation of supramolecular complexes between Mn(III)TPP-*p*-CF₃ and γ -CD. These shifts could result from ring current effects and/or paramagnetic dipolar effects of Mn^{III}. The fact that the spectra obtained

correspond to the fast exchange regime indicates that the interaction between all the perfluorinated groups of the porphyrin and the internal cavity of the cyclodextrin is weak. The Mn(III)TPP-*p*-CF₃ signal at 7.85 ppm disappeared upon the addition of 3 equivalents of γ -CD, confirming its reduction to Mn(II)TPP-*p*-CF₃.

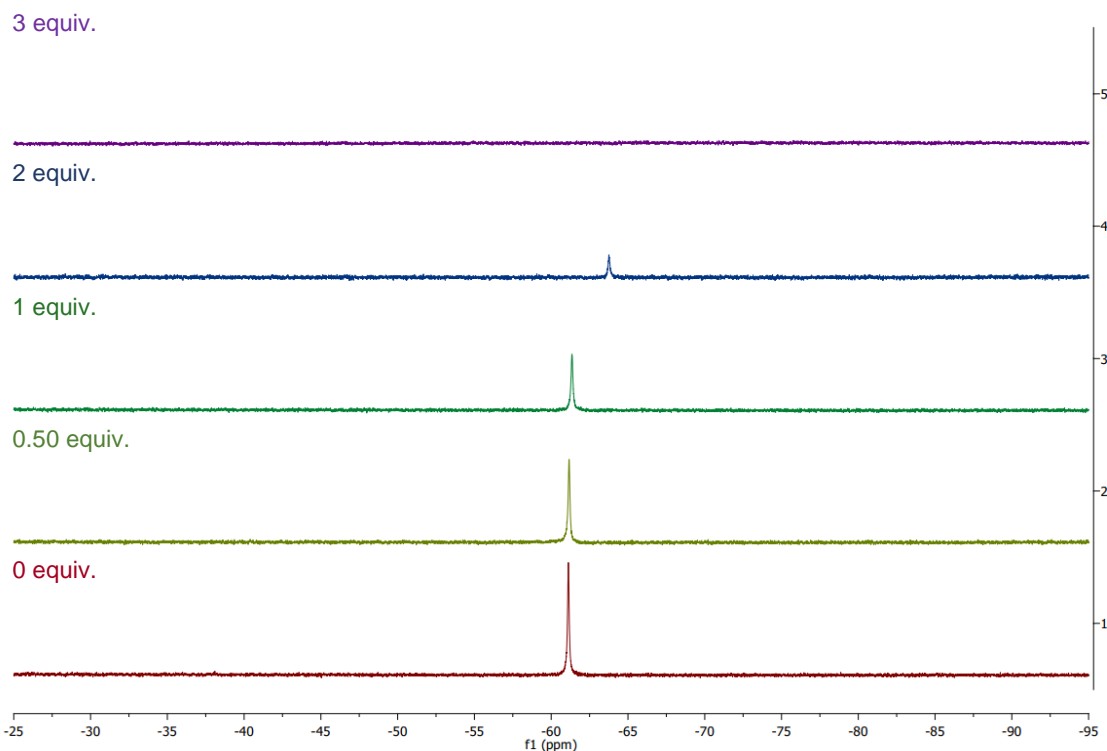


Figure 3.20. ^{19}F NMR spectra titration of γ -CD with 0.5 mM Mn(III)TPP-*p*-CF₃, recorded in DMSO-*d*₆ (25°C). Number of equivalents of γ -CD added: 0 (red line); 0.50 (light green line); 1 (dark green line); 2 (blue line); 3 (purple line). (Number of scans = 128; acquisition time = 0.5 s).

The ^{19}F NMR spectra resulting from the titration of Mn(III)TPP-*p*-CF₃ with γ -CD (Figure 3.20) shows that the ^{19}F NMR signal of the CF₃ groups in the Mn^{III}-porphyrin gradually decreases its intensity in the presence of γ -CD, up to the addition of 3 equivalents of γ -CD, which makes the signal not detected. This fact confirms that the addition of γ -CD reduces Mn^{III} to its 2+ oxidation state, even without the addition of any reducing agent (as verified through the UV-Vis study), since Mn(II)TPP-*p*-CF₃ is not detected by ^{19}F NMR. As Mn(III) has a relatively small paramagnetic relaxation effect, the ^{19}F signal of the Mn^{III}-porphyrin can be detected, whereas Mn(II) strongly broadens the ^{19}F signal, causing the reduced probe signal to disappear. However, in the range of γ -CD added concentrations below 3 equivalents, the chemical shift of the ^{19}F signal gradually became more negative, indicating an interaction between the Mn^{III}-porphyrin and γ -CD, which could result from the

paramagnetic dipolar shift induced by Mn^{III} and/or by shifts induced by the inclusion of the meso $p\text{-CF}_3$ substituted phenyl groups of the porphyrin in the cavity of the cyclodextrin.

In order to further establish the stoichiometry between $\text{Mn(III)TPP-}p\text{-CF}_3$ and $\gamma\text{-CD}$, an absorbance titration study and the Job's method were conducted.

3.3.4. Stoichiometric Determination

With a view to establishing the stoichiometry of the supramolecular complex between the Mn^{III} -porphyrin and the γ -cyclodextrin, titration studies were carried out by UV-Vis absorption spectroscopy, including a titration where $\text{Mn(III)TPP-}p\text{-CF}_3$ was kept constant and several molar fractions of $\gamma\text{-CD}$ were added, as well as Job's method. However, these studies did not provide consistent results: firstly, the Soret band of $\text{Mn(III)TPP-}p\text{-CF}_3$ is very little influenced by the interaction with the CDs, and secondly, the presence of $\gamma\text{-CD}$ reduces the $\text{Mn(III)TPP-}p\text{-CF}_3$ in a time-dependent manner, which strongly reduces the intensity of the Soret band.

As an illustration of the results obtained, Figure 3.21 shows a titration involving multiple solutions, where the number of moles of $\text{Mn(III)TPP-}p\text{-CF}_3$ was kept constant and increasing molar fractions of $\gamma\text{-CD}$ were added. The final volume of all the solutions was kept constant. The wavelength in which the absorbance values were maximum (465 nm - corresponding to the Soret band) was fixed, and the absorbance values were collected. Thus, it was possible to plot a graph of absorbance vs molar fractions of $\gamma\text{-CD}$ used.

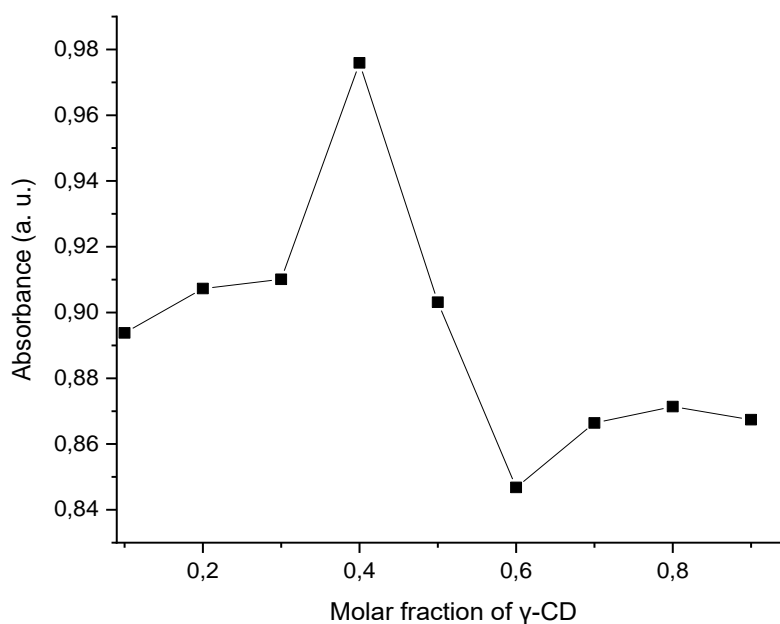


Figure 3.21. Plot of absorbance (at 465 nm) of 0.052 mM $\text{Mn(III)TPP-}p\text{-CF}_3$ (in THF) vs. molar fractions of $\gamma\text{-CD}$ used to prepare the solutions.

This plot shows very little and erratic changes in absorbance in relation to the molar fractions of γ -CD used. For higher molar fractions, the band intensity decreases as a result of the reduction of the porphyrin. The same happens in the data obtained from Job's method. The use of ^{19}F NMR based titrations is also not useful because the ^{19}F signals disappear with reduction induced by the presence of γ -CD. Therefore, the present studies cannot be used to support an expected 2:1 stoichiometry (γ -CD:Mn(III)TPP-*p*-CF₃), based on what is described in the literature for similar systems [137].

3.4. *In Vitro* Antitumour Assays

A successful probe discovery program encompasses a range of processes based on strong target definition and validation, using a diverse set of biochemical and cell-based assays with functional relevance to the biological system under study. Therefore, the main goal in probe development is to identify a stable compound with sub- μM activity and reasonable selectivity. The compounds identified from probe discovery can also be used as starting scaffolds for lead optimization approaches [172].

In the present study, the effect of several concentrations of both Mn(III)TPP-*p*-CF₃ and γ -CD*Mn(III)TPP-*p*-CF₃ on a human cell culture was evaluated by two different *in vitro* techniques: the MTT and SRB assays. The SRB assay is widely used to conduct screening assays to investigate antiproliferative capacity in cell-based (*in vitro*) studies. The amount of bound dye can be used to quantify cell mass (cell density), which is then extrapolated to measure cell proliferation (section 2.12.1). The MTT method is a reliable method for estimating the metabolic activity of living cells (section 2.12.2). Under optimized conditions, the absorbance of the cellular suspension after reaction with MTT is directly proportional to the number of viable cells. The results thus obtained are presented in Figure 3.22.

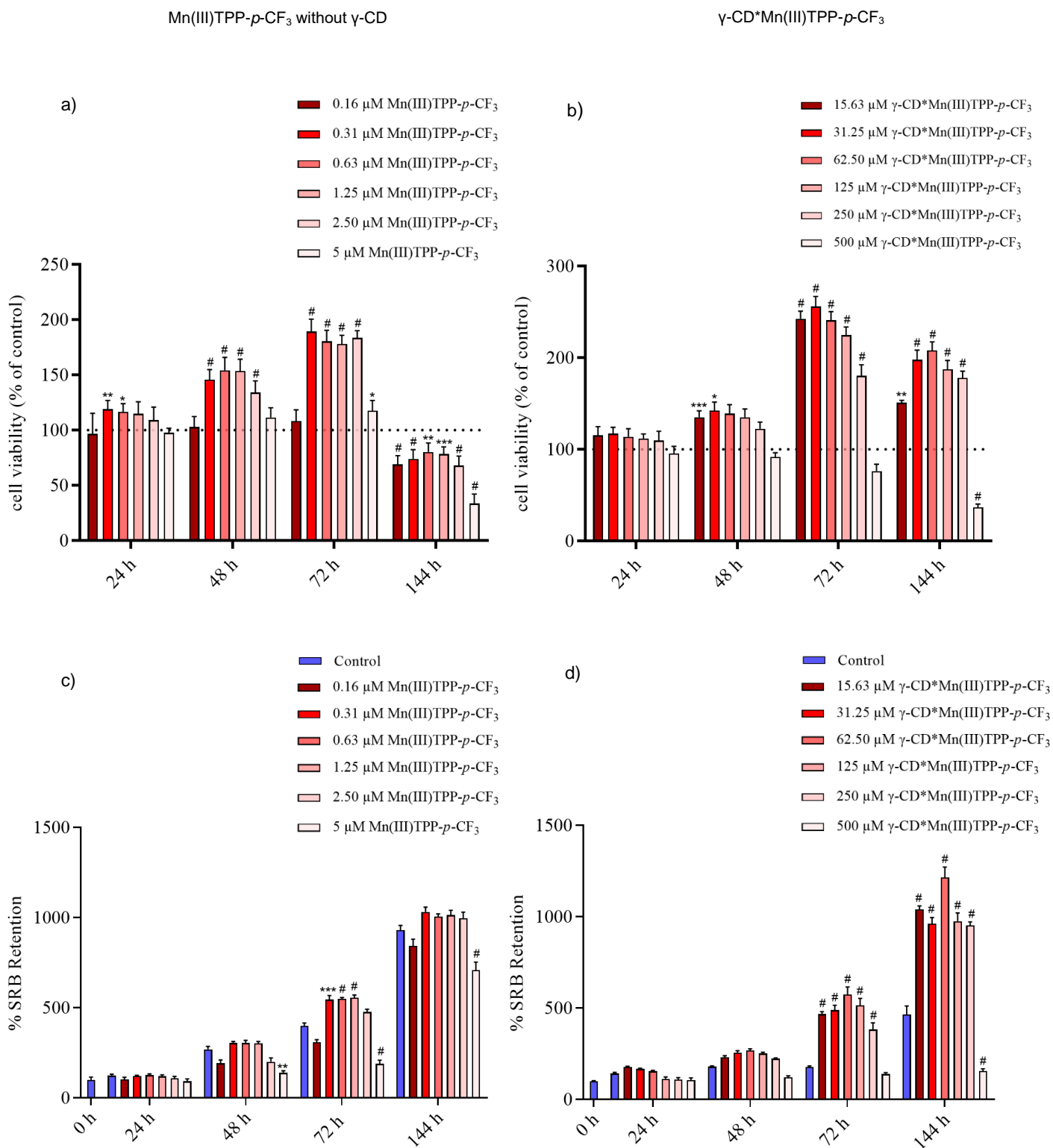


Figure 3.22. Effect of Mn(III)TPP-*p*-CF₃ and γ -CD*Mn(III)TPP-*p*-CF₃ on Caco-2 cells, assessed by the MTT (a) and b)) and SRB (c) and d)) colorimetric tests. After 72 hours of the addition of the tested agents, the medium was discarded and new culture medium was added. Control corresponds to 144 hours. Results are represented as mean \pm SD of three independent experiments ($n = 3$), performed in triplicate for each experimental condition. The MTT data were expressed in % of each control at the different time points. The SRB data were expressed in % of C₀, according to equation 2.4. Data were analysed with the software GraphPad Prism 8.0.2, using the one-way ANOVA

method followed by the Tukey's multiple comparison test: p* < 0.05; p** < 0.01; p*** < 0.001; p# < 0.0001 were considered statistically significant. If p > 0.05 no statistically significant differences were considered.

These results suggest that for the highest and lowest concentrations of the tested agents, free and CD-included – 0.16 and 5 μM, and 15.63 μM and 500 μM, respectively – no significant effect on cell viability was detected. These results evidence that these particular concentrations are either too low or too high to allow reliable quantification of the effect of these compounds *in vitro*. Therefore, it can be assumed that the use of these complexes as probes in this type of cancer cells is limited by a concentration threshold, *i.e.*, they have an ideal range of concentrations.

In general, for the Mn(III)TPP-*p*-CF₃ complex it can be observed that cellular viability tends to increase with longer incubation times (up to 72 hours). The same result was confirmed by the SRB assay. Based on these data, it may be concluded that there is an overall concentration-dependent increasing cell density and viability with incubation time, clearly revealing that Mn(III)TPP-*p*-CF₃ does not show either a cytotoxic or an anti-proliferative activity on this type of cells. Indeed, only the highest probe concentration (5 μM) was found to induce a slight growth-inhibitory effect.

Regarding the γ-CD*Mn(III)TPP-*p*-CF₃ inclusion complex, cellular proliferation and viability tend to increase with exposure time, particularly between 48 h and 72 h, and for the intermediate concentrations currently applied. It is important to highlight that these concentrations are 100x higher than those used for Mn(III)TPP-*p*-CF₃ (since CD-inclusion increases the probe hydrophilicity allowing much larger dosages to be administered).

Concerning the reversibility study for the isolated probe, cell proliferation was found to increase continuously over time, even after removal of the probe from the culture medium (and further incubation for 72 h), although there was a very significant decrease in cellular viability for the highest concentrations. The reversibility study for the CD-included probe showed that both cell proliferation and cell viability continued to increase over time, even in the absence of any probe in the cellular medium.

These results evidence that the Mn(III)TPP-*p*-CF₃ complex affects the metabolism of the living cells, contrary to its CD-included analogue. Thus, it may be assumed that this effect may be caused by the CF₃ groups, which are included in the cyclodextrin cavity in γ-CD*Mn(III)TPP-*p*-CF₃ and therefore hindered from exerting their effect. According to previous studies by García-LLinás *et al.*, the CF₃ group can participate in noncovalent interactions acting as a Lewis acid and disrupting the normal function of a NADP⁺-dependent isocitrate dehydrogenase (IDH), which is responsible for converting isocitrate to

α -ketoglutarate. It should also be emphasized that IDH mutations are usually found in multiple hematologic and solid tumours, inducing premalignant disorders [173].

According to these *in vitro* data, the CD-included γ -CD*Mn(III)TPP-*p*-CF₃ complex showed a smaller anticancer effect as compared with the free probe Mn(III)TPP-*p*-CF₃, even when the former was applied in much larger (x100) concentrations. These results render the Mn(III)TPP-*p*-CF₃ and γ -CD*Mn(III)TPP-*p*-CF₃ compounds feasible for application as contrast agents since their main goal is to signal cellular redox imbalance, present in neoplasms, without affecting cell growth and viability.

Synthesis and Characterization of a Biocompatible Fluorinated Mn(III)-Porphyrin as a Redox Responsive ^{19}F -NMR/ T_1 Bimodal MRI Contrast Agent

Conclusion and Future Perspectives

Synthesis and Characterization of a Biocompatible Fluorinated Mn(III)-Porphyrin as a Redox Responsive ^{19}F -NMR/ T_1 Bimodal MRI Contrast Agent

MRI-based cell imaging is a versatile technique because it can exploit several different types of contrast [24]. For *in vivo* MRI applications, three key factors should be considered: the sensitivity of detection, the toxicity/tolerance as well as the biodistribution profile of the probe, and the feasibility of developing responsive probes for chemical shift imaging. In the case of sensitivity, probe design and detection systems should be improved over the next decade. Over the field range of 1.5 to 7 T, paramagnetic-based ^{19}F probes display sensitivity gains of between 15 to 20 times those of diamagnetic analogues [170]. The clearance of these probes occurs reasonably quickly *in vivo*, through renal or biliary pathways determined by the charge and hydrophobicity of the complex.

In this dissertation, a new fluorinated porphyrin derivative was successfully synthesized and characterized. It was found to stabilize both Mn^{III} and Mn^{II} in the complexes, in a biologically significant range of redox potentials. In solution, the manganese cation undergoes reversible reduction/oxidation reactions, fostered by the natural reducing and oxidative agents ascorbic and oxygen, respectively. The reoxidation by air exposure is quite slow but it is fully achieved within a couple of hours. Nevertheless, the complex is not reduced by glutathione, one of the main redox buffers of the intracellular space. In human plasma, the glutathione reach levels of approximately 7 μM , while ascorbic acid has a concentration of around 20-40 μM . Thus, the role of ascorbic acid should not be disregarded either in maintaining the extracellular redox state. By way of example, in circulating immune cells, the ascorbic acid concentration reaches millimolar concentrations and controls the redox state, allowing its quantification in those cells [63]. The Mn^{III} reduction by ascorbic acid is complete within some minutes, whereas reoxidation by oxygen is slow but will be determined by the varying tissue oxygenation levels. As a consequence, the MRI signal variation of $\text{Mn}^{\text{II}}/\text{Mn}^{\text{III}}$ is expected to be relatively sensitive to the oxygenation state of tissues, particularly under hypoxic conditions.

Moreover, the ^{19}F NMR resonances of Mn^{III} are relatively well-defined, which may give rise to further possibilities to exploit such complexes as paramagnetic ^{19}F NMR probes [150]. Also, it was possible to demonstrate that the complexation with manganese decreased both T_1 and T_2 relaxivity times, making its application as ^{19}F MRI contrast agents not only possible but advantageous. The non-water solubility of $\text{Mn}(\text{III})\text{TPP-}p\text{-CF}_3$ was overcome with its inclusion with $\gamma\text{-CD}$, even though it was unfeasible to determine the stoichiometry between the two compounds experimentally. Also, the inclusion with CD causes the reduction of Mn^{III} to Mn^{II} , which compromises its application as a redox probe and made the characterization of $\gamma\text{-CD}^*\text{Mn}(\text{III})\text{TPP-}p\text{-CF}_3$ erratic. The cytotoxicity evaluation on the Caco-2 cell line confirmed *in vitro* non-toxicity of both tested agents in the used μM concentrations, being the $\gamma\text{-CD}^*\text{Mn}(\text{III})\text{TPP-}p\text{-CF}_3$ complex less cytotoxic than

Mn(III)TPP-*p*-CF₃. It is important to point out that the concentrations used for these studies should be bigger, considering that the typical range used for MRI probes is mM.

In general, the development of MRI imaging probes to monitor redox environments *in vivo* deals with several limitations. Some Mn^{III/II} chelates have been reported to have suitable *in vitro* properties as redox-active MRI contrast agents, however, their kinetic stability might be inadequate [174]. Hence, Mn-porphyrin redox responsive complexes can be advantageous. The present Mn^{III}/Mn^{II} porphyrin complex satisfies many criteria required for a redox imaging probe: water solubility (through its inclusion with CD), biocompatibility, non-toxicity, kinetic stability in both metal oxidation states and decreasing of T_1 relaxivity time.

For future studies, it is paramount to perform a stability study of the probe-CD inclusion complex and characterization of the redox behaviour of the Mn(III)TPP-*p*-CF₃ probe in the absence and presence of γ -CD using cyclic voltammetry to determine their mid-point redox potentials. The interaction of Mn(III)TPP-*p*-CF₃ with human serum albumin (HSA) in water could also be studied in order to solubilise it and improve its water relaxivity properties. In addition, it would be interesting to synthesize other porphyrin derivatives with a similar distance from the paramagnetic atom to the CF₃ moieties and comprising additional groups favouring its hydrosolubility. In the cases where the water solubility of the probe increases so much that their water studies become possible without jeopardizing their redox stability, a full water proton relaxometric study of its Mn^{III}/Mn^{II} redox states would be warranted. On the other hand, it would be interesting to continue the *in vitro* studies including other types of human cancer cells, in order to achieve a better understanding of the selectivity and mechanisms of action of both the free and CD-included complexes as contrast agents, considering some variations (decrease) that were presently detected in cell proliferation (particularly at 48 h and 72 h of incubation). It would also be important to assess other concentrations of both tested agents, as well as different incubation times, thus increasing the exposure period of the cells to the compounds under investigation. Furthermore, other biological tests should be carried out to ascertain the effect of prolonged exposure (*e.g.*, 144 h), allowing to compare these results with those obtained in the currently reported reversibility studies.

Additionally, the application of different techniques apart from NMR should be considered, for a complete characterization of the new agent γ -CD*Mn(III)TPP-*p*-CF₃ which would greatly assist interpretation of the *in vitro* data. DSC (Differential Scanning Calorimetry) and TGA (Thermal Gravimetric Analysis), in particular, would allow confirming the inclusion of the meso aryl groups of Mn(III)TPP-*p*-CF₃ into the γ -CD cavity. Inclusion

complexes in different cyclodextrins (e.g., β -CD) could also be tested, aiming at a better fit between probe dimensions and CD internal cavity.

Synthesis and Characterization of a Biocompatible Fluorinated Mn(III)-Porphyrin as a Redox Responsive ^{19}F -NMR/ T_1 Bimodal MRI Contrast Agent

References

Synthesis and Characterization of a Biocompatible Fluorinated Mn(III)-Porphyrin as a Redox Responsive ^{19}F -NMR/ T_1 Bimodal MRI Contrast Agent

1. Phelps, M.E. PET: The Merging of Biology and Imaging into Molecular Imaging. *Journal of Nuclear Medicine* **2000**, *41*, 661–681.
2. Cassidy, P.J.; Radda, G.K. Molecular Imaging Perspectives. *Journal of the Royal Society Interface* **2005**, *2*, 133–144, doi:10.1098/rsif.2005.0040.
3. Cherry, S.R. Multimodality in Vivo Imaging Systems: Twice the Power or Double the Trouble? *Annual Review of Biomedical Engineering* **2006**, *8*, 35–62, doi:10.1146/annurev.bioeng.8.061505.095728.
4. Qin, C.; Zhu, S.; Tian, J. New Optical Molecular Imaging Systems. *Current Pharmaceutical Biotechnology* **2010**, *11*, 620–627, doi:10.2174/138920110792246519.
5. Wu, M.; Shu, J. Multimodal Molecular Imaging: Current Status and Future Directions. *Contrast Media and Molecular Imaging* **2018**, *2018*, doi:10.1155/2018/1382183.
6. Xing, Y.; Zhao, J.; Conti, P.S.; Chen, K. Radiolabeled Nanoparticles for Multimodality Tumor Imaging. *Theranostics* **2014**, *4*, 290–306, doi:10.7150/thno.7341.
7. Wang, Y.; Chen, J.; Yang, B.; Qiao, H.; Gao, L.; Su, T.; Ma, S.; Zhang, X.; Li, X.; Liu, G.; et al. In Vivo MR and Fluorescence Dual-Modality Imaging of Atherosclerosis Characteristics in Mice Using Profilin-1 Targeted Magnetic Nanoparticles. *Theranostics* **2016**, *6*, 272–286, doi:10.7150/thno.13350.
8. O'Halloran, R.; Kopell, B.H.; Sprooten, E.; Goodman, W.K.; Frangou, S. Multimodal Neuroimaging-Informed Clinical Applications in Neuropsychiatric Disorders. *Frontiers in Psychiatry* **2016**, *7*, 1–14, doi:10.3389/fpsy.2016.00063.
9. Teipel, S.; Drzezga, A.; Grothe, M.J.; Barthel, H.; Chételat, G.; Schuff, N.; Skudlarski, P.; Cavado, E.; Frisoni, G.B.; Hoffmann, W.; et al. Multimodal Imaging in Alzheimer's Disease: Validity and Usefulness for Early Detection. *The Lancet Neurology* **2015**, *14*, 1037–1053, doi:10.1016/S1474-4422(15)00093-9.
10. Thorsen, F.; Fite, B.; Mahakian, L.M.; Seo, J.W.; Qin, S.; Harrison, V.; Johnson, S.; Ingham, E.; Caskey, C.; Sundstrøm, T.; et al. Multimodal Imaging Enables Early Detection and Characterization of Changes in Tumor Permeability of Brain Metastases. *Journal of Controlled Release* **2013**, *172*, 812–822, doi:10.1016/j.jconrel.2013.10.019.
11. F. Bloch, W. W. Hansen, and M.P. Nuclear Induction. *Phys. Rev.* **1946**, *738*, 1939.
12. Purcell, E.M.; Torrey, H.C.; Pound, R. v. Resonance Absorption by Nuclear Magnetic Moments in a Solid. *Physical Review* **1946**, *69*, 37–38, doi:10.1103/PhysRev.69.37.
13. W. G. Proctor; F. C. Yu The Dependence of a Nuclear Magnetic Resonance Frequency Upon Chemical Compound. *Physics Rev.* **1950**, *77*, 717.
14. Dickinson, W.C. Dependence of the F19 Nuclear Resonance Position on Chemical Compound. *Physics Rev.* **1950**, *77*, 736–737.
15. Damadian, R. Tumor Detection by Nuclear Magnetic Resonance. *Science* **1971**, *171*, 1151–1153.
16. Lauterbur, P.C. Image Formation by Induced Local Interactions: Examples Employing Nuclear Magnetic Resonance. *Nature* **1973**, *242*, 190–191.

17. Lauterbur, P.C. Magnetic Resonance Zeugmatography. *Pure Appl. Chem.* **1974**, *40*, 149–157.
18. Lauterbur, P.C., M.D.M., and R.A.M. Augmentation of Tissue Water Proton Spin-Lattice Relaxation Rates by in Vivo Addition of Paramagnetic Ions. *Electrons to Tissues* **1978**, *1*, 752–759, doi:10.1016/B978-0-12-225401-7.50093-X.
19. Hounsfield, G.N. Computerized Transverse Axial Scanning (Tomography): Part I. Description of System. *British Journal of Radiology* **1973**, 1016–1022.
20. Bottomley, P. A., Hart, H. R., Edelstein, W. A., Schenck, J. F., Smith, L. S., Leue, W. M., Mueller, O.M., and Redington, R.W. NMR Imaging/Spectroscopy System to Study Both Anatomy and Metabolism. *Lancet* **1983**, *322*, 273–274.
21. Hawkes, R.; Holland, G.; Moore, W.S.; Worthington, B. Nuclear Magnetic Resonance (NMR) Tomography of the Brain: A Preliminary Clinical Assessment with Demonstration of Pathology. *Journal of Computer Assisted Tomography* 1980, *4*, 577–586.
22. Smith, F.W.; Hutchison, J.M.S.; Mallard, J.R.; Johnson, G.; Redpath, T.W.; Selbie, R.D.; Reid, A.; Smith, C.C. Oesophageal Carcinoma Demonstrated by Whole-Body Nuclear Magnetic Resonance Imaging. *British Medical Journal (Clinical research ed.)* **1981**, *282*, 510–512, doi:10.1136/bmj.282.6263.510.
23. Victor M. S. G.; Carlos F. G. C. G. *Ressonância Magnética Nuclear: Fundamentos, Metodos e Aplicações*; Fundação Calouste GulbenKian, Ed.; Lisboa, 2002;
24. Srivastava, A.K.; Kadayakkara, D.K.; Bar-shir, A.; Gilad, A.A.; McMahan, M.T.; Bulte, J.W.M. Advances in Using MRI Probes and Sensors for in Vivo Cell Tracking as Applied to Regenerative Medicine. **2015**, 323–336, doi:10.1242/dmm.018499.
25. Grover, V.P.B.; Tognarelli, J.M.; Crossey, M.M.E.; Cox, I.J.; Taylor-Robinson, S.D.; McPhail, M.J.W. Magnetic Resonance Imaging: Principles and Techniques: Lessons for Clinicians. *Journal of Clinical and Experimental Hepatology* **2015**, *5*, 246–255, doi:10.1016/j.jceh.2015.08.001.
26. Mark A. B.; Richard C. S. *MRI: Basic Principles and Applications*; 3rd ed.; 2005;
27. Yousaf, T.; Dervenoulas, G.; Politis, M. *Advances in MRI Methodology*; 1st ed.; Elsevier Inc., 2018; Vol. 141; ISBN 9780128154182.
28. Srinivas, M.; Boehm-Sturm, P.; Figdor, C.G.; de Vries, I.J.; Hoehn, M. Labeling Cells for in Vivo Tracking Using ¹⁹F MRI. *Biomaterials* **2012**, *33*, 8830–8840, doi:10.1016/j.biomaterials.2012.08.048.
29. Ahrens, E.T.; Zhong, J.H. In Vivo MRI Cell Tracking Using Perfluorocarbon Probes and Fluorine-19 Detection. *NMR in Biomedicine* **2013**, *26*.
30. Peterson, K.L.; Srivastava, K.; Pierre, V.C. Fluorinated Paramagnetic Complexes: Sensitive and Responsive Probes for Magnetic Resonance Spectroscopy and Imaging. *Frontiers in chemistry* **2018**, *6*, 160, doi:10.3389/fchem.2018.00160.
31. Ocali, O.; Atalar, E. Ultimate Intrinsic Signal-to-Noise Ratio in MRI. *Magnetic Resonance in Medicine* **1998**, *39*, 462–473, doi:https://doi.org/10.1002/mrm.1910390317.

32. Polzehl, J.; Tabelow, K. Low SNR in Diffusion MRI Models. *Journal of the American Statistical Association* **2016**, *111*, 1480–1490, doi:10.1080/01621459.2016.1222284.
33. Staal, X.; Koshkina, O.; Srinivas, M. *In Vivo 19-Fluorine Magnetic Resonance Imaging*; Elsevier Inc., 2018; ISBN 9780128127339.
34. Lee, H.K.; Nalcioglu, O.; Buxton, R.B. Correction for Chemical-Shift Artifacts in ¹⁹F Imaging of PFOB: Simultaneous Multislice Imaging. *Magnetic Resonance in Medicine* **1991**, *21*, 21–29, doi:https://doi.org/10.1002/mrm.1910210105.
35. Tweedle, M.F. The Chemistry of Contrast Agents in Medical Magnetic Resonance Imaging. *Journal of the American Chemical Society* **2002**, *124*, 884–885, doi:10.1021/ja0152963.
36. Wahsner, J.; Gale, E.M.; Rodríguez-Rodríguez, A.; Caravan, P. Chemistry of MRI Contrast Agents: Current Challenges and New Frontiers. *Chemical Reviews* **2019**, *119*, 957–1057, doi:10.1021/acs.chemrev.8b00363.
37. Boros, E.; Gale, E.M.; Caravan, P. MR Imaging Probes: Design and Applications. *Dalton Transactions* **2015**, *44*, 4804–4818, doi:10.1039/c4dt02958e.
38. Mewis, R.E.; Archibald, S.J. Biomedical Applications of Macrocyclic Ligand Complexes. *Coordination Chemistry Reviews* **2010**, *254*, 1686–1712, doi:10.1016/j.ccr.2010.02.025.
39. Lancelot, E. Revisiting the Pharmacokinetic Profiles of Gadolinium-Based Contrast Agents. *Investigative Radiology* **2016**, *51*, 691–700, doi:10.1097/RLI.0000000000000280.
40. Peters, J.A.; Djanashvili, K.; Geraldes, C.F.G.C. Imaging with Lanthanides. In *Comprehensive Supramolecular Chemistry II*; J.L. Atwood, Ed.; 2017; Vol. 8, pp. 261–293.
41. Woods, M.; Woessner, D.E.; Sherry, A.D. Paramagnetic Lanthanide Complexes as PARACEST Agents for Medical Imaging. *Chemical Society Reviews* **2006**, *35*, 500–511, doi:10.1039/B509907M.
42. Ratnakar, S.J.; Chirayil, S.; Funk, A.M.; Zhang, S.; Queiró, J.F.; Geraldes, C.F.G.C.; Kovacs, Z.; Sherry, A.D. *A Novel Frequency-Selective PH-Responsive PARACEST Agent*, *Angewandte Chemie Int. Ed.*, 2020;
43. Chen, J.; Lanza, G.M.; Wickline, S.A. Quantitative Magnetic Resonance Fluorine Imaging: Today and Tomorrow. *Wiley interdisciplinary reviews. Nanomedicine and nanobiotechnology* **2010**, *2*, 431–440, doi:10.1002/wnan.87.
44. Silvio A.; Peter C. Biodistribution of Gadolinium-Based Contrast Agents, Including Gadolinium Deposition. *J Magn Reson Imaging* **2009**, *30*, doi:10.1002/jmri.21969.
45. Kueny-Stotz, M.; Garofalo, A.; Felder-Flesch, D. Manganese-Enhanced MRI Contrast Agents: From Small Chelates to Nanosized Hybrids. *European Journal of Inorganic Chemistry* **2012**, 1987–2005, doi:10.1002/ejic.201101163.
46. Dipanjan P.; Anne H. S.; Samuel A. W.; Gregory M. L. Manganese-Based MRI Contrast Agents: Past, Present and Future. *Tetrahedron* **2011**, *67*, 8431–8444, doi:10.1016/j.tet.2011.07.076.

47. Van Breemen, R.B.; Li, Y. Caco-2 Cell Permeability Assays to Measure Drug Absorption. *Expert Opinion on Drug Metabolism and Toxicology* **2005**, *1*, 175–185, doi:10.1517/17425255.1.2.175.
48. Takaoka, Y.; Sakamoto, T.; Tsukiji, S.; Narazaki, M.; Matsuda, T.; Tochio, H.; Shirakawa, M.; Hamachi, I. Self-Assembling Nanoprobes That Display off/on ¹⁹F Nuclear Magnetic Resonance Signals for Protein Detection and Imaging. *Nature Chemistry* **2009**, *1*, 557–561, doi:10.1038/nchem.365.
49. Díaz-López, R.; Tsapis, N.; Fattal, E. Liquid Perfluorocarbons as Contrast Agents for Ultrasonography and ¹⁹F-MRI. *Pharmaceutical Research* **2009**, *27*, 1, doi:10.1007/s11095-009-0001-5.
50. Dong, X.; Chen, H.; Qin, J.; Wei, C.; Liang, J.; Liu, T.; Kong, D.; Lv, F. Thermosensitive Porphyrin-Incorporated Hydrogel with Four-Arm PEG-PCL Copolymer (II): Doxorubicin Loaded Hydrogel as a Dual Fluorescent Drug Delivery System for Simultaneous Imaging Tracking in Vivo. *Drug Delivery* **2017**, *24*, 641–650, doi:10.1080/10717544.2017.1289570.
51. Muhammad I.; Muhammad R.; Ahmad Kaleem Q.; Muhammad Azhar K.; Muhammad T. Emerging Applications of Porphyrins and Metalloporphyrins in Biomedicine and Diagnostic Magnetic Resonance Imaging. *Biosensors (Basel)* **2018**, *19*.
52. Calvete, M.J.F.; Pinto, S.M.A.; Pereira, M.M.; Geraldes, C.F.G.C. Metal Coordinated Pyrrole-Based Macrocycles as Contrast Agents for Magnetic Resonance Imaging Technologies: Synthesis and Applications. *Coordination Chemistry Reviews* **2017**, *333*, 82–107, doi:10.1016/j.ccr.2016.11.011.
53. Song, R.; Robert, A.; Bernadou, J.; Meunier, B. Sulfonated and Acetamidofunctionalized Tetraarylporphyrins as Biomimetic Oxidation Catalysts under Aqueous Conditions. *Inorganica Chimica Acta* **1998**, *272*, 228–234, doi:10.1016/s0020-1693(97)05944-6.
54. Ni, D.; Bu, W.; Ehlerding, E.B.; Cai, W.; Shi, J. Engineering of Inorganic Nanoparticles as Magnetic Resonance Imaging Contrast Agents. *Chemical Society Reviews* **2017**, *46*, 7438–7468, doi:10.1039/c7cs00316a.
55. Lauffer, R.B. Paramagnetic Metal Complexes as Water Proton Relaxation Agents for NMR Imaging: Theory and Design. *Chemical Reviews* **1987**, *87*, 901–927, doi:10.1021/cr00081a003.
56. P. Caravan; J. J. Ellison; T. J. McMurry; R. B. Lauffer Gadolinium(III) Chelates as MRI Contrast Agents: Structure, Dynamics, and Applications. *Chem Rev* **1999**, *99*, 2293–2352, doi:10.1021/cr980440x.
57. Tei, L.; Gugliotta, G.; Fekete, M.; Kálmán, F.K.; Botta, M. Mn(II) Complexes of Novel Hexadentate AAZTA-like Chelators: A Solution Thermodynamics and Relaxometric Study. *Dalton Transactions* **2011**, *40*, 2025–2032, doi:10.1039/c0dt01114b.
58. Lee, T.; Zhang, X. an; Dhar, S.; Faas, H.; Lippard, S.J.; Jasanoff, A. In Vivo Imaging with a Cell-Permeable Porphyrin-Based MRI Contrast Agent. *Chemistry and Biology* **2010**, *17*, 665–673, doi:10.1016/j.chembiol.2010.05.009.

59. Mauri, M.; Collico, V.; Morelli, L.; Das, P.; García, I.; Penaranda Avila, J.; Bellini, M.; Rotem, R.; Truffi, M.; Corsi, F.; et al. MnO Nanoparticles Embedded in Functional Polymers as T₁ Contrast Agents for Magnetic Resonance Imaging. *ACS Applied Nano Materials* **2020**, *3*, 3787–3797, doi:10.1021/acsnm.0c00474.
60. Gilad, A.A.; Walczak, P.; McMahon, M.T.; Na, H. bin; Lee, J.H.; An, K.; Hyeon, T.; van Zijl, P.C.M.; Bulte, J.W.M. MR Tracking of Transplanted Cells with “Positive Contrast” Using Manganese Oxide Nanoparticles. *Magnetic resonance in medicine* **2008**, *60*, 1–7, doi:10.1002/mrm.21622.
61. Cheng, W.; Haedicke, I.E.; Nofiele, J.; Martinez, F.; Beera, K.; Scholl, T.J.; Cheng, H.-L.M.; Zhang, X. Complementary Strategies for Developing Gd-Free High-Field T₁ MRI Contrast Agents Based on MnIII Porphyrins. *Journal of Medicinal Chemistry* **2014**, *57*, 516–520, doi:10.1021/jm401124b.
62. Sara Pinto; Vanessa Tomé; Mário J.F. Calvete; M. Margarida C.A. Castro; Éva Tóth; Carlos F.G.C. Geraldes Metal-Based Redox-Responsive MRI Contrast Agents. *Coord. Chem. Rev* **2019**, *390*, 1–31, doi:10.1016/j.ccr.2019.03.014.
63. Pinto, S.M.A.; Calvete, M.J.F.; Ghica, M.E.; Soler, S.; Gallardo, I.; Pallier, A.; Laranjo, M.B.; Cardoso, A.M.S.; Castro, M.M.C.A.; Brett, C.M.A.; et al. A Biocompatible Redox MRI Probe Based on a Mn(II)/Mn(III) Porphyrin. *Dalton Transactions* **2019**, *48*, 3249–3262, doi:10.1039/C8DT04775H.
64. Geraldes, C.F.G.C.; Castro, M.M.C.A.; Peters, J.A. Mn(III) Porphyrins as Potential MRI Contrast Agents for Diagnosis and MRI-Guided Therapy. *Coordination Chemistry Reviews* **2021**, *445*, 214069, doi:https://doi.org/10.1016/j.ccr.2021.214069.
65. Aime, S.; Botta, M.; Gianolio, E.; Terreno, E. A p(O₂)-Responsive MRI Contrast Agent Based on the Redox Switch of Manganese(II / III) – Porphyrin Complexes. *Angewandte Chemie International Edition* **2000**, *39*, 747–750, doi:https://doi.org/10.1002/(SICI)1521-3773(20000218)39:4<747::AID-ANIE747>3.0.CO;2-2.
66. Zhang, Z.; He, R.; Yan, K.; Guo, Q. ni; Lu, Y. guo; Wang, X. xia; Lei, H.; Li, Z. ying Synthesis and in Vitro and in Vivo Evaluation of Manganese(III) Porphyrin-Dextran as a Novel MRI Contrast Agent. *Bioorganic and Medicinal Chemistry Letters* **2009**, *19*, 6675–6678, doi:10.1016/j.bmcl.2009.10.003.
67. Callewaert, M.; Roullin, V.G.; Cadiou, C.; Millart, E.; Van Gulik, L.; Andry, M.C.; Portefaix, C.; Hoeffel, C.; Laurent, S.; Elst, L. Vander; et al. Tuning the Composition of Biocompatible Gd Nanohydrogels to Achieve Hypersensitive Dual T₁/T₂ MRI Contrast Agents. *Journal of Materials Chemistry B* **2014**, *2*, 6397–6405, doi:10.1039/c4tb00783b.
68. Tu, C.; Osborne, E.A.; Louie, A.Y. Activatable T₁ and T₂ Magnetic Resonance Imaging Contrast Agents. *Annals of Biomedical Engineering* **2011**, *39*, 1335–1348, doi:10.1007/s10439-011-0270-0.

69. Bryson, J.M.; Reineke, J.W.; Reineke, T.M. Macromolecular Imaging Agents Containing Lanthanides: Can Conceptual Promise Lead to Clinical Potential? *Macromolecules* **2012**, *45*, 8939–8952, doi:10.1021/ma301568u.
70. Sarsour, E.H.; Kumar, M.G.; Chaudhuri, L.; Kalen, A.L.; Goswami, P.C. Redox Control of the Cell Cycle in Health and Disease. *Antioxidants & Redox Signaling* **2009**, *11*, 2985–3011, doi:10.1089/ars.2009.2513.
71. Wilson, W.R.; Hay, M.P. Targeting Hypoxia in Cancer Therapy. *Nature Reviews Cancer* **2011**, *11*, 393–410, doi:10.1038/nrc3064.
72. Chen, H.; Tang, X.; Gong, X.; Chen, D.; Li, A.; Sun, C.; Lin, H.; Gao, J. Reversible Redox-Responsive ¹H/¹⁹F MRI Molecular Probes. *Chemical Communications* **2020**, *56*, 4106–4109, doi:10.1039/D0CC00778A.
73. Forman, H.J.; Zhang, H.; Rinna, A. Glutathione: Overview of Its Protective Roles, Measurement, and Biosynthesis. *Molecular Aspects of Medicine* **2009**, *30*, 1–12, doi:10.1016/j.mam.2008.08.006.
74. Bjørklund, G.; Tinkov, A.A.; Hosnedlová, B.; Kizek, R.; Ajsuvakova, O.P.; Chirumbolo, S.; Skalnaya, M.G.; Peana, M.; Dadar, M.; El-Ansary, A.; et al. The Role of Glutathione Redox Imbalance in Autism Spectrum Disorder: A Review. *Free Radical Biology and Medicine* **2020**, *160*, 149–162, doi:10.1016/j.freeradbiomed.2020.07.017.
75. Morris, G.; Anderson, G.; Dean, O.; Berk, M.; Galecki, P.; Martin-Subero, M.; Maes, M. The Glutathione System: A New Drug Target in Neuroimmune Disorders. *Molecular Neurobiology* **2014**, *50*, 1059–1084, doi:10.1007/s12035-014-8705-x.
76. Lushchak, V.I. Glutathione Homeostasis and Functions: Potential Targets for Medical Interventions. *Journal of Amino Acids* **2012**, *2012*, 1–26, doi:10.1155/2012/736837.
77. Han, D.; Hanawa, N.; Saberi, B.; Kaplowitz, N. Mechanisms of Liver Injury. III. Role of Glutathione Redox Status in Liver Injury. *American Journal of Physiology - Gastrointestinal and Liver Physiology* **2006**, *291*, doi:10.1152/ajpgi.00001.2006.
78. Hwang, C.; Sinskey, A.J.; Lodish, H.F. Oxidized Redox State of Glutathione in the Endoplasmic Reticulum. *Science* **1992**, *257*, 1496–1502, doi:10.1126/science.1523409.
79. Marí, M.; Colell, A.; Morales, A.; von Montfort, C.; Garcia-Ruiz, C.; Fernández-Checa, J.C. Redox Control of Liver Function in Health and Disease. *Antioxidants and Redox Signaling* **2010**, *12*, 1295–1331, doi:10.1089/ars.2009.2634.
80. Jones, D.P. Redox Potential of GSH/GSSG Couple: Assay and Biological Significance. *Methods in Enzymology* **2002**, *348*, 93–112, doi:10.1016/S0076-6879(02)48630-2.
81. Ludolph, A.C. *Vitamins and Nutrition*; 1991; Vol. 4; ISBN 9780123838643.
82. Drouin, G.; Godin, J.-R.; Page, B. The Genetics of Vitamin C Loss in Vertebrates. *Current Genomics* **2011**, *12*, 371–378, doi:10.2174/138920211796429736.
83. Henry, B.Y. Oxidation of Ascorbic Acid in Tea. *Nature* **1943**, *151*, 112.

84. Xie, D.; King, T.L.; Banerjee, A.; Kohli, V.; Que, E.L. Exploiting Copper Redox for ¹⁹F Magnetic Resonance-Based Detection of Cellular Hypoxia. *Journal of the American Chemical Society* **2016**, *138*, 2937–2940, doi:10.1021/jacs.5b13215.
85. Li, S.; Purdy, W.C. Cyclodextrins and Their Applications in Analytical Chemistry. *Chemical Reviews* **1992**, *92*, 1457–1470, doi:10.1021/cr00014a009.
86. Zhang, J.; Ma, P.X. Cyclodextrin-Based Supramolecular Systems for Drug Delivery: Recent Progress and Future Perspective. *Advanced Drug Delivery Reviews* **2013**, *65*, 1215–1233, doi:10.1016/j.addr.2013.05.001.
87. Irie, T.; Uekama, K. Pharmaceutical Applications of Cyclodextrins. III. Toxicological Issues and Safety Evaluation. *Journal of Pharmaceutical Sciences* **1997**, *86*, 147–162, doi:10.1021/js960213f.
88. Brewster, M.E.; Loftsson, T. Cyclodextrins as Pharmaceutical Solubilizers. *Advanced Drug Delivery Reviews* **2007**, *59*, 645–666, doi:10.1016/j.addr.2007.05.012.
89. Guo Xiliang; Shuang Shaomin; Dong Chuan; Feng Feng; M.S. Wong Comparative Study on the Inclusion Behavior between Meso-Tetrakis(4-N-Ethylpyridinium)Porphyrin and β -Cyclodextrin Derivatives. *Spectrochimica Acta Part A* **2005**, *61*, 413–418.
90. Hamai, S.; Ohshida, T. Inclusion Complexes of Cyclodextrins with Tetrakis(4-Carboxyphenyl) Porphyrin and Tetrakis(4-Sulfonatophenyl)Porphyrin in Aqueous Solutions. *Journal of Inclusion Phenomena* **2004**, *50*, 209–217, doi:10.1007/s10847-004-9650-5.
91. Hostetler, J.S.; Hanson, L.H.; Stevens, D.A. Effect of Cyclodextrin on the Pharmacology of Antifungal Oral Azoles. *Antimicrobial Agents and Chemotherapy* **1992**, *36*, 477–480, doi:10.1128/AAC.36.2.477.
92. Müller, B.W.; Albers, E. Effect of Hydrotropic Substances on the Complexation of Sparingly Soluble Drugs with Cyclodextrin Derivatives and the Influence of Cyclodextrin Complexation on the Pharmacokinetics of the Drugs. *Journal of Pharmaceutical Sciences* **1991**, *80*, 599–604, doi:10.1002/jps.2600800620.
93. Li, X.X.; Wang, J.W.; Guo, Y.J.; Kong, L.H.; Pan, J.H. Study on Inclusion Complexes of Meso-Tetrakis(2-Thienyl) Porphyrin and Cu-Meso-Tetrakis(2-Thienyl)Porphyrin with Cyclodextrins by Spectroscopy Method. *Journal of Inclusion Phenomena and Macrocyclic Chemistry* **2007**, *58*, 307–315, doi:10.1007/s10847-006-9158-2.
94. Kong, L.H.; Guo, Y.J.; Li, X.X.; Pan, J.H. Study on the Supramolecular Systems of 5-(2-Hydroxy Phenyl)-10,15,20-Tris (4-Methoxy Phenyl) Porphyrin with Cyclodextrins. *Spectrochimica Acta - Part A: Molecular and Biomolecular Spectroscopy* **2007**, *66*, 594–598, doi:10.1016/j.saa.2006.04.001.
95. Wang, K.-R.; Guo, D.-S.; Jiang, B.-P.; Liu, Y. Excitonic Coupling Interactions in the Self-Assembly of Perylene-Bridged Bis(β -Cyclodextrin)s and Porphyrin. *Chemical Communications* **2012**, *48*, 3644–3646, doi:10.1039/C2CC17786B.
96. Kano, K.; Kitagishi, H.; Sone, Y.; Nakazawa, N.; Kodera, M. Redox Behavior of a Manganese Porphyrin Complexed with Per-O-Methylated β -Cyclodextrin in Aqueous Solution. *European*

- Journal of Inorganic Chemistry* **2006**, 2006, 4043–4053, doi:<https://doi.org/10.1002/ejic.200600336>.
97. Koji Kano; Hiroaki Kitagishi; Masahito Kodera; Shun Hirota Dioxxygen Binding to a Simple Myoglobin Model in Aqueous Solution. *Angewandte Chemie* **2005**, 117, 439–442.
98. Sun, M.; Zhang, H.-Y.; Liu, B.-W.; Liu, Y. Construction of a Supramolecular Polymer by Bridged Bis(Permethy-β-Cyclodextrin)s with Porphyrins and Its Highly Efficient Magnetic Resonance Imaging. *Macromolecules* **2013**, 46, 4268–4275, doi:10.1021/ma400806s.
99. Whitebread, S.; Hamon, J.; Bojanic, D.; Urban, L. Keynote Review: In Vitro Safety Pharmacology Profiling: An Essential Tool for Successful Drug Development. *Drug Discovery Today* **2005**, 10, 1421–1433, doi:10.1016/S1359-6446(05)03632-9.
100. Tung, C.H. Fluorescent Peptide Probes for in Vivo Diagnostic Imaging. *Biopolymers - Peptide Science Section* **2004**, 76, 391–403, doi:10.1002/bip.20139.
101. Helander, H.F.; Fändriks, L. Surface Area of the Digestive Tract-Revisited. *Scandinavian Journal of Gastroenterology* **2014**, 49, 681–689, doi:10.3109/00365521.2014.898326.
102. Kong, S.; Zhang, Y.H.; Zhang, W. Regulation of Intestinal Epithelial Cells Properties and Functions by Amino Acids. *BioMed Research International* **2018**, 2018, doi:10.1155/2018/2819154.
103. Okumura, R.; Takeda, K. Roles of Intestinal Epithelial Cells in the Maintenance of Gut Homeostasis. *Experimental and Molecular Medicine* **2017**, 49, e338-8, doi:10.1038/emm.2017.20.
104. Miron, N.; Cristea, V. Enterocytes: Active Cells in Tolerance to Food and Microbial Antigens in the Gut. *Clinical and Experimental Immunology* **2012**, 167, 405–412, doi:10.1111/j.1365-2249.2011.04523.x.
105. Hochman, J.H.; Fix, J.A.; LeCluyse, E.L. In Vitro and in Vivo Analysis of the Mechanism of Absorption Enhancement by Palmitoylcarnitine. *Journal of Pharmacology and Experimental Therapeutics* **1994**, 269, 813–822.
106. Artursson, P.; Magnusson, C. Epithelial Transport of Drugs in Cell Culture. II: Effect of Extracellular Calcium Concentration on the Paracellular Transport of Drugs of Different Lipophilicities across Monolayers of Intestinal Epithelial (Caco-2) Cells. *Journal of Pharmaceutical Sciences* **1990**, 79, 595–600, doi:10.1002/jps.2600790710.
107. Verhoeckx, K.; Cotter, P.; López-Expósito, I.; Kleiveland, C.; Lea, T.; Mackie, A.; Requena, T.; Swiatecka, D.; Wichers, H. *The Impact of Food Bioactives on Health: In Vitro and Ex Vivo Models*; 2015; ISBN 9783319161044.
108. Sun, H.; Chow, E.C.Y.; Liu, S.; Du, Y.; Pang, K.S. The Caco-2 Cell Monolayer: Usefulness and Limitations. *Expert Opinion on Drug Metabolism and Toxicology* **2008**, 4, 395–411, doi:10.1517/17425255.4.4.395.
109. Bergström, C.A.S. In Silico Predictions of Drug Solubility and Permeability: Two Rate-Limiting Barriers to Oral Drug Absorption. *Basic and Clinical Pharmacology and Toxicology* **2005**, 96, 156–161, doi:10.1111/j.1742-7843.2005.pto960303.x.

110. O'Callaghan, Y.; O'Brien, N. Bioaccessibility, Cellular Uptake and Transepithelial Transport of α -Tocopherol and Retinol from a Range of Supplemented Foodstuffs Assessed Using the Caco-2 Cell Model. *International Journal of Food Science and Technology* **2010**, *45*, 1436–1442, doi:10.1111/j.1365-2621.2010.02285.x.
111. Artursson, P.; Palm, K.; Luthman, K. Caco-2 Monolayers in Experimental and Theoretical Predictions of Drug Transport. *Advanced Drug Delivery Reviews* **2012**, *64*, 280–289, doi:10.1016/j.addr.2012.09.005.
112. Fogh, J.; Fogh, J.M.; Orfeo, T. One Hundred and Twenty Seven Cultured Human Tumor Cell Lines Producing Tumors in Nude Mice. *Journal of the National Cancer Institute* **1977**, *59*, 221–226, doi:10.1093/jnci/59.1.221.
113. Fogh, J.; Wright, W.C.; Loveless, J.D. Absence of HeLa Cell Contamination in 169 Cell Lines Derived from Human Tumors. *Journal of the National Cancer Institute* **1977**, *58*, 209–214, doi:10.1093/jnci/58.2.209.
114. Keller, H. Key Characteristics. *Tempo* **1956**, *2*, 5–16, doi:10.1017/s0040298200052827.
115. American Type Culture Collection Caco-2 [Caco2] Available online: <https://www.atcc.org/products/htb-37> (accessed on 5 June 2021).
116. Vachon, P.H.; Beaulieu, J.F. Transient Mosaic Patterns of Morphological and Functional Differentiation in the Caco-2 Cell Line. *Gastroenterology* **1992**, *103*, 414–423, doi:10.1016/0016-5085(92)90829-N.
117. Engle, M.J.; Goetz, G.S.; Alpers, D.H. Caco-2 Cells Express a Combination of Colonocyte and Enterocyte Phenotypes. *Journal of Cellular Physiology* **1998**, *174*, 362–369, doi:10.1002/(SICI)1097-4652(199803)174:3<362::AID-JCP10>3.0.CO;2-B.
118. Chantret, I.; Rodolosse, A.; Barbat, A.; Dussaulx, E.; Brot-Laroche, E.; Zweibaum, A.; Rousset, M. Differential Expression of Sucrase-Isomaltase in Clones Isolated from Early and Late Passages of the Cell Line Caco-2: Evidence for Glucose-Dependent Negative Regulation. *Journal of Cell Science* **1994**, *107*, 213–225, doi:10.1242/jcs.107.1.213.
119. Mahraoui, L.; Rodolosse, A.; Barbat, A.; Dussaulx, E.; Zweibaum, A.; Rousset, M.; Brot-Laroche, E. Presence and Differential Expression of SGLT1, GLUT1, GLUT2, GLUT3 and GLUT5 Hexose-Transporter MRNAs in Caco-2 Cell Clones in Relation to Cell Growth and Glucose Consumption. *Biochemical Journal* **1994**, *298*, 629–633, doi:10.1042/bj2980629.
120. Sharp, P. Methods and Options for Estimating Iron and Zinc Bioavailability Using Caco-2 Cell Models: Benefits and Limitations. *International Journal for Vitamin and Nutrition Research* **2005**, *75*, 413–421, doi:10.1024/0300-9831.75.6.413.
121. Yamashita, S.; Konishi, K.; Yamazaki, Y.; Taki, Y.; Sakane, T.; Sezaki, H.; Furuyama, Y. New and Better Protocols for a Short-Term Caco-2 Cell Culture System. *Journal of Pharmaceutical Sciences* **2002**, *91*, 669–679, doi:10.1002/jps.10050.
122. Artursson, P.; Karlsson, J. Correlation between Oral Drug Absorption in Humans and Apparent Drug Permeability Coefficients in Human Intestinal Epithelial (Caco-2) Cells.

- Biochemical and Biophysical Research Communications* **1991**, *175*, 880–885, doi:10.1016/0006-291X(91)91647-U.
123. Bourguine, J.; Billaut-Laden, I.; Happillon, M.; Lo-Guidice, J.M.; Maunoury, V.; Imbenotte, M.; Broly, F. Gene Expression Profiling of Systems Involved in the Metabolism and the Disposition of Xenobiotics: Comparison between Human Intestinal Biopsy Samples and Colon Cell Lines. *Drug Metabolism and Disposition* **2012**, *40*, 694–705, doi:10.1124/dmd.111.042465.
124. Lei, J.; Zhang, M. qiu; Huang, C. yu; Bai, L.; He, Z. hu Effects of Ascorbic Acid and Citric Acid on Iron Bioavailability in an in Vitro Digestion/ Caco-2 Cell Culture Model. *Nan fang yi ke da xue xue bao = Journal of Southern Medical University* **2008**, *28*, 1743–1747.
125. Shimizu, M. Interaction between Food Substances and the Intestinal Epithelium. *Bioscience, Biotechnology and Biochemistry* **2010**, *74*, 232–241, doi:10.1271/bbb.90730.
126. Knipp, G.T.; Ho, N.F.H.; Barsuhn, C.L.; Borchardt, R.T. Paracellular Diffusion in Caco-2 Cell Monolayers: Effect of Perturbation on the Transport of Hydrophilic Compounds That Vary in Charge and Size. *Journal of Pharmaceutical Sciences* **1997**, *86*, 1105–1110, doi:10.1021/js9700309.
127. Albert S. Tang, Prashant J. Chikhale, P.K.S. and R.T.B. Utilization of a Human Intestinal Epithelial Cell Culture System (Caco-2) for Evaluating Cytoprotective Agents 1993.
128. Burton, P.S.; Conradi, R.A.; Ho, N.F.H.; Hilgers, A.R.; Borchardt, R.T. How Structural Features Influence the Biomembrane Permeability of Peptides. *Journal of Pharmaceutical Sciences* **1996**, *85*, 1336–1340, doi:10.1021/js960067d.
129. Wachter, V.J.; Salphati, L.; Benet, L.Z. Active Secretion and Enterocytic Drug Metabolism Barriers to Drug Absorption PII of Original Article: S0169-409X(96)003304. The Article Was Originally Published in *Advanced Drug Delivery Reviews* 20 (1996) 99–112.1. *Advanced Drug Delivery Reviews* **2001**, *46*, 89–102, doi:10.1016/s0169-409x(00)00126-5.
130. Yamashita, S., Tanaka, Y., Endoh, Y., Taki, Y., Sakane, T., Nadai, T., & Sezaki, H. 1997_Analysis of Drug Permeation across Caco-2 Monolayer.Pdf. *Pharmaceutical Research* 1997, *14*, 486–491.
131. Spiess, H.W. 50th Anniversary Perspective: The Importance of NMR Spectroscopy to Macromolecular Science. *Macromolecules* **2017**, *50*, 1761–1777, doi:10.1021/acs.macromol.6b02736.
132. Wang, X.P.; Pan, J.H.; Li, W.H.; Zhang, Y. Study on the Supramolecular System of TAPP with Cyclodextrins by Polarography. *Talanta* **2001**, *54*, 805–810, doi:10.1016/S0039-9140(00)00661-5.
133. Vosburgh, W.C.; Cooper, G.R. Complex Ions. I. The Identification of Complex Ions in Solution by Spectrophotometric Measurements. *Journal of the American Chemical Society* **1941**, *63*, 437–442, doi:10.1021/ja01847a025.
134. Facchiano, A.; Ragone, R. Modification of Job's Method for Determining the Stoichiometry of Protein – Protein Complexes. **2003**, *313*, 170–172.

135. Ingham, K.C. On the Application of Job's Method of Continuous Variation to the Stoichiometry of Protein-Ligand Complexes. *Analytical Biochemistry* **1975**, *68*, 660–663, doi:[https://doi.org/10.1016/0003-2697\(75\)90666-1](https://doi.org/10.1016/0003-2697(75)90666-1).
136. Huang, C.Y. Determination of Binding Stoichiometry by the Continuous Variation Method: The Job Plot. *Methods in Enzymology* **1982**, *87*, 509–525, doi:10.1016/S0076-6879(82)87029-8.
137. Renny, J.S.; Tomasevich, L.L.; Tallmadge, E.H.; Collum, D.B. Method of Continuous Variations: Applications of Job Plots to the Study of Molecular Associations in Organometallic Chemistry. *Angewandte Chemie - International Edition* **2013**, *52*, 11998–12013, doi:10.1002/anie.201304157.
138. ATCC Thawing, Propagating, and Cryopreserving Protocol (Caco-2). *Physical Sciences-Oncology Center Network Bioresource Core Facility* **2012**, *37*, 3–4.
139. Louis, K.S.; Siegel, A.C. Cell Viability Analysis Using Trypan Blue: Manual and Automated Methods. *740*, 7–12, doi:10.1007/978-1-61779-108-6.
140. Strober, W. Trypan Blue Exclusion Test of Cell Viability. *Current protocols in immunology / edited by John E. Coligan ... [et al.]* **2001**, Appendix 3, 2–3, doi:10.1002/0471142735.ima03bs21.
141. Natoli, M.; Leoni, B.D.; D'Agnano, I.; Zucco, F.; Felsani, A. Good Caco-2 Cell Culture Practices. *Toxicology in Vitro* **2012**, *26*, 1243–1246, doi:10.1016/j.tiv.2012.03.009.
142. Skehan, P.; Storeng, R.; Scudiero, D.; Monks, A.; McMahon, J.; Vistica, D.; Warren, J.T.; Bokesch, H.; Kenney, S.; Boyd, M.R. New Colorimetric Cytotoxicity Assay for Anticancer-Drug Screening. *Journal of the National Cancer Institute* **1990**, *82*, 1107–1112, doi:10.1093/jnci/82.13.1107.
143. Vichai, V.; Kirtikara, K. Sulforhodamine B Colorimetric Assay for Cytotoxicity Screening. *Nature Protocols* **2006**, *1*, 1112–1116, doi:10.1038/nprot.2006.179.
144. Orellana, E.; Kasinski, A. Sulforhodamine B (SRB) Assay in Cell Culture to Investigate Cell Proliferation. *Bio-Protocol* **2016**, *6*, doi:10.21769/bioprotoc.1984.
145. Yan, D.; Lu, J.; Wei, M.; Evans, D.G.; Duan, X. Sulforhodamine B Intercalated Layered Double Hydroxide Thin Film with Polarized Photoluminescence. **2009**, 1381–1388.
146. Grela, E.; Kozłowska, J.; Grabowiecka, A. Current Methodology of MTT Assay in Bacteria – A Review. *Acta Histochemica* **2018**, *120*, 303–311, doi:10.1016/j.acthis.2018.03.007.
147. Hamid, R.; Rotshteyn, Y.; Rabadi, L.; Parikh, R.; Bullock, P. Comparison of Alamar Blue and MTT Assays for High Through-Put Screening. *Toxicology in Vitro* **2004**, *18*, 703–710, doi:10.1016/j.tiv.2004.03.012.
148. Plumb, J.A. Cell Sensitivity Assays: Clonogenic Assay. *Methods in molecular medicine* **2004**, *88*, 159–164, doi:10.1385/1-59259-687-8:17.
149. Gomes, D. Síntese de Ligandos Nitrogenados e Complexos Metálicos Com Potencialidade Para Imagiologia Médica. Dissertation submitted to the Department of Chemistry of the University of Coimbra, **2019**.

150. Chalmers, K.H.; De Luca, E.; Hogg, N.H.M.; Kenwright, A.M.; Kuprov, I.; Parker, D.; Botta, M.; Ian Wilson, J.; Blamire, A.M. Design Principles and Theory of Paramagnetic Fluorine-Labelled Lanthanide Complexes as Probes For¹⁹F Magnetic Resonance: A Proof-of-Concept Study. *Chemistry - A European Journal* **2010**, *16*, 134–148, doi:10.1002/chem.200902300.
151. Chalmers, K.H.; Botta, M.; Parker, D. Strategies to Enhance Signal Intensity with Paramagnetic Fluorine-Labelled Lanthanide Complexes as Probes for ¹⁹F Magnetic Resonance. *Dalton Transactions* **2011**, *40*, 904–913, doi:10.1039/c0dt01232g.
152. Zheng, W.; Shan, N.; Yu, L.; Wang, X. UV-Visible, Fluorescence and EPR Properties of Porphyrins and Metalloporphyrins. *Dyes and Pigments* **2008**, *77*, 153–157, doi:10.1016/j.dyepig.2007.04.007.
153. Imran, M.; Ramzan, M.; Qureshi, A.K.; Azhar Khan, M.; Tariq, M. Emerging Applications of Porphyrins and Metalloporphyrins in Biomedicine and Diagnostic Magnetic Resonance Imaging. *Biosensors* **2018**, *8*, 1–17, doi:10.3390/bios8040095.
154. Huang, X.; Nakanishi, K.; Berova, N. Porphyrins and Metalloporphyrins: Versatile Circular Dichroic Reporter Groups for Structural Studies. *Chirality* **2000**, *12*, 237–255, doi:10.1002/(SICI)1520-636X(2000)12:4<237::AID-CHIR10>3.0.CO;2-6.
155. Lan, M.; Zhao, H.; Yuan, H.; Jiang, C.; Zuo, S.; Jiang, Y. Absorption and EPR Spectra of Some Porphyrins and Metalloporphyrins. *Dyes and Pigments* **2007**, *74*, 357–362, doi:10.1016/j.dyepig.2006.02.018.
156. Kim, B.F.; Bohandy, J. Spectroscopy of Porphyrins. *Johns Hopkins APL Technical Digest (Applied Physics Laboratory)* **1981**, *2*, 153–163.
157. Kocsis, L.; Herman, P.; Eke, A. The Modified Beer-Lambert Law Revisited. *Physics in Medicine and Biology* **2006**, *51*, doi:10.1088/0031-9155/51/5/N02.
158. Valicsek, Z.; Horváth, O. Application of the Electronic Spectra of Porphyrins for Analytical Purposes: The Effects of Metal Ions and Structural Distortions. *Microchemical Journal* **2013**, *107*, 47–62, doi:10.1016/j.microc.2012.07.002.
159. Wu, Y.; Zhang, X.; Zhang, Z.; Wang, X.; Geng, Z.; Jin, C.; Liu, H.; Yao, M. Effects of Diesel-Ethanol-THF Blend Fuel on the Performance and Exhaust Emissions on a Heavy-Duty Diesel Engine. *Fuel* **2020**, *271*, 117633, doi:10.1016/j.fuel.2020.117633.
160. Fowles, J.; Boatman, R.; Bootman, J.; Lewis, C.; Morgott, D.; Rushton, E.; van Rooij, J.; Banton, M. A Review of the Toxicological and Environmental Hazards and Risks of Tetrahydrofuran. *Critical Reviews in Toxicology* **2013**, *43*, 811–828, doi:10.3109/10408444.2013.836155.
161. Lee, H.; Park, J.B. Evaluation of the Effects of Dimethylsulphoxide on Morphology, Cellular Viability, mRNA, and Protein Expression of Stem Cells Culture in Growth Media. *Biomedical Reports* **2017**, *7*, 291–296, doi:10.3892/br.2017.961.

162. Santos, N.C.; Figueira-Coelho, J.; Martins-Silva, J.; Saldanha, C. Multidisciplinary Utilization of Dimethyl Sulfoxide: Pharmacological, Cellular, and Molecular Aspects. *Biochemical Pharmacology* **2003**, *65*, 1035–1041, doi:10.1016/S0006-2952(03)00002-9.
163. Galvao, J.; Davis, B.; Tilley, M.; Normando, E.; Duchon, M.R.; Cordeiro, M.F. Unexpected Low-Dose Toxicity of the Universal Solvent DMSO. *FASEB Journal* **2014**, *28*, 1317–1330, doi:10.1096/fj.13-235440.
164. Modesitt, S.C.; Parsons, S.J. In Vitro and in Vivo Histone Deacetylase Inhibitor Therapy with Vorinostat and Paclitaxel in Ovarian Cancer Models: Does Timing Matter? *Gynecologic Oncology* **2010**, *119*, 351–357, doi:10.1016/j.ygyno.2010.06.030.
165. Marcus, R.A. On the Theory of Oxidation-Reduction Reactions Involving Electron Transfer. I. *The Journal of Chemical Physics* **1956**, *24*, 966–978, doi:10.1063/1.1742723.
166. Hull, W.E.; Port, R.E.; Herrmann, R.; Britsch, B.; Kunz, W. Metabolites of 5-Fluorouracil in Plasma and Urine, as Monitored by ¹⁹F Nuclear Magnetic Resonance Spectroscopy, for Patients Receiving Chemotherapy with or without Methotrexate Pretreatment. *Cancer Research* **1988**, *48*, 1680–1688.
167. Yu, J.; Kodibagkar, V.; Cui, W.; Mason, R. ¹⁹F: A Versatile Reporter for Non-Invasive Physiology and Pharmacology Using Magnetic Resonance. *Current Medicinal Chemistry* **2005**, *12*, 819–848, doi:10.2174/0929867053507342.
168. Tirotta, I.; Dichiarante, V.; Pigliacelli, C.; Cavallo, G.; Terraneo, G.; Bombelli, F.B.; Metrangolo, P.; Resnati, G. ¹⁹F Magnetic Resonance Imaging (MRI): From Design of Materials to Clinical Applications. *Chemical Reviews* **2015**, *115*, 1106–1129, doi:10.1021/cr500286d.
169. Senanayake, P.K.; Kenwright, A.M.; Parker, D.; van der Hoorn, S.K. Responsive Fluorinated Lanthanide Probes for ¹⁹F Magnetic Resonance Spectroscopy. *Chemical Communications* **2007**, 2923–2925, doi:10.1039/b705844f.
170. Harvey, P.; Kuprov, I.; Parker, D. Lanthanide Complexes as Paramagnetic Probes for ¹⁹F Magnetic Resonance. *European Journal of Inorganic Chemistry* **2012**, 2015–2022, doi:10.1002/ejic.201100894.
171. Dai, W.; Lv, Y.; Wang, L.; Shang, S.; Chen, B.; Li, G.; Gao, S. Highly Efficient Oxidation of Alcohols Catalyzed by a Porphyrin-Inspired Manganese Complex. *Chemical Communications* **2015**, *51*, 11268–11271, doi:10.1039/C5CC03657G.
172. Roy, A. Early Probe and Drug Discovery in Academia: A Minireview. *High-Throughput* **2018**, *7*, 1–14, doi:10.3390/ht7010004.
173. García-Llinás, X.; Bauzá, A.; Seth, S.K.; Frontera, A. Importance of R-CF₃...O Tetrel Bonding Interactions in Biological Systems. *Journal of Physical Chemistry A* **2017**, *121*, 5371–5376, doi:10.1021/acs.jpca.7b06052.
174. Gale, E.M.; Jones, C.M.; Ramsay, I.; Farrar, C.T.; Caravan, P.; Gale, E.M.; Jones, C.M.; Ramsay, I.; Farrar, C.T.; Caravan, P. A Janus Chelator Enables Biochemically Responsive MRI Contrast With Exceptional Dynamic Range A Janus Chelator Enables Biochemically

Synthesis and Characterization of a Biocompatible Fluorinated Mn(III)-Porphyrin as a Redox Responsive ¹⁹F-NMR/T₁ Bimodal MRI Contrast Agent

Responsive MRI Contrast with Exceptional Dynamic Range. **2016**,
doi:10.1021/jacs.6b10898.